

PROCESSING AND PROPERTIES OF $\text{Mo}_2\text{Fe}(\text{Ni})\text{B}_2\text{-Fe}(\text{Ni})$ CERMETS

*A Thesis Submitted
In Partial Fulfilment of the Requirements
for the Degree of*

DOCTOR OF PHILOSOPHY

By
PRADIP KUMAR BAGDI

To the
MATERIALS SCIENCE PROGRAMME
INDIAN INSTITUTE OF TECHNOLOGY, KANPUR

DECEMBER, 1995



CERTIFICATE

This is to certify that the thesis entitled "PROCESSING AND PROPERTIES OF $\text{Mo}_2\text{Fe}(\text{Ni})\text{B}_2$ - $\text{Fe}(\text{Ni})$ CERMETS" submitted by Pradip Kumar Bagdi (Roll No. 8811263) has been carried out under my supervision and has not been submitted elsewhere for a degree.

G. S. Upadhyaya
11 Dec. 1995

Dr. G. S. Upadhyaya
Professor
Department of Materials and
Metallurgical Engineering
Indian Institute of Technology
Kanpur - 208016

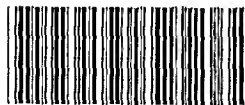
27 JUN 1996

CENTRAL LIBRARY

111 CAMPUS

121713
Doc. No. A.

MSP-1995-D-BAG-PRO



A121713

ACKNOWLEDGEMENTS

The author is deeply indebted to his thesis supervisor Prof. G. S. Upadhyaya for his invaluable guidance and constant inspiration at every stage throughout the present research.

Also the author expresses his special thanks to M/s S. C. Soni, K. P. Mukherjee, B. K. Jain, B. Sharma, Uma Sankar, U. S. Lal and P. K. Paul for their cooperation during the course of this work.

The friendship with the colleagues Drs. S. K. Bhaumick, H. N. Azari, P. K. Kar, N. Kapuri and Mr. D. Banerjee is greatly appreciated.

M/s V. P. Gupta, B. K. Jain and Yash Pal should be acknowledged for their excellent tracing work and typing respectively.

Finally the author expresses his deep sense of gratitude to his parents, brothers and sisters for their immense patience, moral support, courage and inspiration during this research programme.

PRADIP KUMAR BAGDI

PUBLICATIONS

Based on the present thesis the following papers have been accepted for publication:

1. Sintering of Binder modified $\text{Mo}_2\text{Fe}(\text{Ni})\text{B}_2$ -Fe(Ni) Cermets, in 'Sintering 95', Ed. R. G. Cornwall, R. M. German, G. L. Messing, Marcel Dekker Inc., New York, 1996 (in Press).
2. Sintering of Mo_2FeB_2 - αFe Cermets by elemental and MoB routes (communicated).

CONTENTS

Page No .

List of Tables	
List of Figures	
Synopsis	i
CHAPTER I LITERATURE REVIEW	1
1.1 INTRODUCTION	1
1.2 Mo-Fe-B BASED CERMETS	2
1.2.1 Phase Equilibria and Crystal Structures	2
1.2.2 Powder Metallurgy (P/M) Processing and Microstructural Aspects	3
1.2.3 Physical and Mechanical Properties	6
1.2.3.1 Sintered Density and Porosity	6
1.2.3.2 Hardness	8
1.2.3.3 Tensile Strength and Ductility	10
1.2.3.4 Transverse Rupture Strength (TRS)	11
1.3 Mo-Fe-Ni-B BASED CERMETS	13
1.3.1 Phase Equilibria and Crystal Structures	13
1.3.2 Powder Metallurgy (P/M) Processing and Microstructural Aspects	14
1.3.3 Physical and Mechanical Properties	14
1.3.3.1 Sintered Density	15
1.3.3.2 Hardness	15
1.3.3.3 Transverse Rupture Strength (TRS)	15
1.4 Mo-Ni-B BASED CERMETS	16
1.4.1 Phase Equilibria and Crystal Structures	16
1.4.2 Powder Metallurgy (P/M) Processing and Microstructural Aspects	17
1.4.3 Mechanical Properties	18
1.4.3.1 Hardness	18
1.4.3.2 Transverse Rupture Strength (TRS)	18
1.5 WEAR BEHAVIOUR OF BORIDE BASED CERMETS	19
1.6 CORROSION BEHAVIOUR OF BORIDE BASED HARD ALLOYS	20
1.6.1 Corrosion Weight Loss Studies	20
1.6.2 High Temperature Oxidation Studies	23
1.6.3 Potentiodynamic Studies	23
1.7 SCOPE OF THE PRESENT INVESTIGATION	24

CHAPTER II EXPERIMENTAL PROCEDURE	26
2.1 RAW MATERIALS	26
2.1.1 Carbonyl Iron Powder	26
2.1.2 Boron Powder	26
2.1.3 Molybdenum Powder	26
2.1.4 Nickel Powder	26
2.1.5 Molybdenum Boride (MoB) Powder	27
2.1.6 Paraffin Wax Powder	27
2.2 POWDER CHARACTERIZATION	28
2.2.1 Particle Shape	28
2.2.2 Particle Size	28
2.2.3 Apparent Density (ρ_{ap})	29
2.3 POWDER METALLURGY (P/M) PROCESSING	29
2.3.1 Powder Premix Preparation	31
2.3.2 Room Temperature Compaction	31
2.3.3 Vacuum Dewaxing and Sintering	31
2.4 DENSIFICATION BEHAVIOUR	32
2.4.1 % Volume shrinkage (% ΔV)	32
2.4.2 Sintered Density (ρ_s)	33
2.4.3 % Total Sintered Porosity (% ϵ_{TS})	33
2.4.4 Densification Parameter (ΔD)	33
2.5 MECHANICAL PROPERTIES	33
2.5.1 Vickers Hardness (HV)	33
2.5.2 Transverse Rupture Strength (TRS)	34
2.5.3 Indentation Fracture Toughness (Kc)	34
2.6 MICROSTRUCTURAL STUDIES	35
2.6.1 Optical Metallography	35
2.6.2 Scanning Electron Metallography	36
2.6.3 Boride Grain Mean Linear Intercept (\bar{I}_α) and Binder Mean Free Path (\bar{I}_β)	36
2.6.4 Boride Phase Contiguity	36
2.7 X-RAY DIFFRACTION ANALYSIS	37
2.8 SATURATION MAGNETIC FLUX DENSITY	38
2.9 THERMAL SHOCK RESISTANCE	38
2.10 CORROSION WEIGHT LOSS STUDY	39

CHAPTER III	EXPERIMENTAL RESULTS	40
PART I :	SINTERING OF $\text{Mo}_2\text{FeB}_2\text{-}\alpha\text{Fe}$ CERMETS THROUGH ELEMENTAL AND MoB ROUTES	40
3.1	CHARACTERIZATION OF MILLED POWDERS	40
3.2	DENSIFICATION BEHAVIOUR	41
3.2.1	% Volume Shrinkage	41
3.2.2	Sintered Density	42
3.2.3	% Total Sintered Porosity	43
3.2.4	Densification Parameter	43
3.3	MECHANICAL PROPERTIES	44
3.3.1	Vickers Hardness	44
3.3.2	Transverse Rupture Strength (TRS)	45
3.3.3	Indentation Fracture Toughness (Kc)	45
3.4	OPTICAL MICROSTRUCTURES AND SEM FRACTOGRAPHY	45
3.5	X-RAY DIFFRACTION ANALYSIS	47
3.6	SATURATION MAGNETIC FLUX DENSITY	48
3.7	THERMAL SHOCK RESISTANCE	48
3.8	CORROSION WEIGHT LOSS STUDY	48
PART II :	SINTERING OF $\text{Mo}_2\text{Fe}(\text{Ni})\text{B}_2$ - $\text{Fe}(\text{Ni})$ CERMETS THROUGH THE MoB ROUTE	49
3.9	CHARACTERIZATION OF MILLED POWDERS	49
3.10	DENSIFICATION BEHAVIOUR	49
3.10.1	% Volume Shrinkage	50
3.10.2	Sintered Density	50
3.10.3	% Total Sintered Porosity (% ϵ_{TS})	51
3.10.4	Densification Parameter	52
3.11	MECHANICAL PROPERTIES	52
3.11.1	Vickers Hardness	53
3.11.2	Transverse Rupture Strength (TRS)	53
3.11.3	Indentation Fracture Toughness (Kc)	54
3.12	OPTICAL MICROSTRUCTURE AND SEM FRACTOGRAPHY	54
3.13	QUANTITATIVE METALLOGRAPHY	56
3.13.1	Boride Grain Mean Linear Intercept (\bar{I}_α)	56
3.13.2	Binder Mean Free Path (\bar{I}_β)	57
3.13.3	Boride Phase Contiguity	57
3.14	X-RAY DIFFRACTION ANALYSIS	57
3.15	SATURATION MAGNETIC FLUX DENSITY	59

3.16 THERMAL SHOCK RESISTANCE	59
3.17 CORROSION WEIGHT LOSS STUDY	60
CHAPTER IV DISCUSSION	62
PART I : $\text{Mo}_2\text{FeB}_2\text{-}\alpha\text{Fe}$ CERMETS THROUGH THE ELEMENTAL AND MoB ROUTES	62
4.1 EFFECT OF BALL MILLING ON AVERAGE PARTICLE SIZE	62
4.2 DENSIFICATION BEHAVIOUR	62
4.3 MECHANICAL PROPERTIES	65
4.3.1 Vickers Hardness	65
4.3.2 Transverse Rupture Strength (TRS)	66
4.3.3 Indentation Fracture Toughness (Kc)	66
4.4 SATURATION MAGNETIC FLUX DENSITY	67
4.5 CORROSION WEIGHT LOSS STUDY	67
PART II : $\text{Mo}_2\text{Fe}(\text{Ni})\text{B}_2\text{-Fe}(\text{Ni})$ CERMETS THROUGH THE MoB ROUTE	68
4.6 EFFECT OF BALL MILLING ON AVERAGE PARTICLE SIZE	68
4.7 DENSIFICATION BEHAVIOUR AND MICROSTRUCTURES	69
4.8 MECHANICAL PROPERTIES	72
4.8.1 Vickers Hardness	72
4.8.2 Transverse Rupture Strength (TRS) and Indentation Fracture Toughness (Kc)	72
4.9 SATURATION MAGNETIC FLUX DENSITY	74
4.10 THERMAL SHOCK RESISTANCE	74
4.11 CORROSION WEIGHT LOSS STUDY	75
4.12 ELECTRONIC APPROACH TO BORIDE BASED CERMETS	76
CHAPTER V CONCLUSIONS	79
REFERENCES	83
APPENDIX	88

LIST OF TABLES

Page No .

1.1	Crystallographic details, theoretical densities of various metallic - intermetallic binders and superhard boride phases in the ternary Mo-Fe-B alloy system.	3
1.2	Crystallographic details, theoretical densities of various metallic - intermetallic binders and superhard boride phases in the ternary Mo-Ni-B alloy system.	18
2.1	Compositions of the various constituents in mass% used for the P/M processing of Mo_2FeB_2 - αFe cermets through the elemental route.	30
2.2	Compositions of the various constituents in mass% used for the P/M processing of $\text{Mo}_2\text{Fe}(\text{Ni})\text{B}_2$ - $\text{Fe}(\text{Ni})$ cermets through the MoB route.	30
3.1	Average particle size of as received powders.	42
3.2	Average particle size of ball milled powders corresponding to different Mo_2FeB_2 - αFe cermets prepared through elemental and MoB routes.	42
3.3	Thermal shock resistance (ΔT) variation of Mo_2FeB_2 - αFe cermets prepared through the MoB route.	48
3.4	Average particle size of the various powder premixes used for the P/M processing of $\text{Mo}_2\text{Fe}(\text{Ni})\text{B}_2$ - $\text{Fe}(\text{Ni})$ cermets through the MoB route.	49
3.5	Thermal shock resistance (ΔT) variation of $\text{Mo}_2\text{Fe}(\text{Ni})\text{B}_2$ - $\text{Fe}(\text{Ni})$ cermets prepared through the MoB route.	60

LIST OF FIGURES

	After Page No.
Fig. 1.1 Isothermal Mo-Fe-B ternary equilibrium phase diagram at 1000°C.	2
Fig. 1.2 Isothermal Mo-Fe-B ternary equilibrium phase diagram at 1050°C.	2
Fig. 1.3 Isothermal Mo-Ni-B ternary equilibrium phase diagram at 800°C.	16
Fig. 1.4 Isothermal Mo-Ni-B ternary equilibrium phase diagram at 1000°/1200°C.	16
Fig. 2.1 Schematic flow diagram of P/M processing of $\text{Mo}_2\text{Fe}(\text{Ni})\text{B}_2$ -Fe(Ni) cermets.	29
Fig. 2.2 Schematic diagram of the vacuum sintering furnace including the electrical circuit diagram.	32
Fig. 2.3 Schematic diagram of the thermal shock measuring furnace including oil bath and electrical circuit diagram.	39
Fig. 3.1 Particle size distribution of as received powders.	40
Fig. 3.2 Particle size distribution of Mo-B-Fe elemental powder premixes.	40
Fig. 3.3 Particle size distribution of MoB-Fe powder premixes.	40
Fig. 3.4 Secondary electron images of various powders: (a) Carbonyl Fe (b) B (c) Mo (d) MoB (e) Carbonyl Ni	40
Fig. 3.5 % Volume shrinkage variation of Mo_2FeB_2 - αFe cermets prepared through elemental and MoB routes and sintered at different temperatures.	41

Fig. 3.6	Sintered density variation of Mo_2FeB_2 - αFe cermet prepared through elemental and MoB routes and sintered at different temperatures.	42
Fig. 3.7	% Total sintered porosity variation of Mo_2FeB_2 - αFe cermet prepared through elemental and MoB routes and sintered at different temperatures.	43
Fig. 3.8	Densification parameter variation of Mo_2FeB_2 - αFe cermet prepared through elemental and MoB routes and sintered at different temperatures.	43
Fig. 3.9	Vickers hardness variation of Mo_2FeB_2 - αFe cermet prepared through elemental and MoB routes and sintered at different temperatures.	44
Fig. 3.10	Transverse rupture strength variation of Mo_2FeB_2 - αFe cermet prepared through elemental and MoB routes and sintered at different temperatures.	45
Fig. 3.11	Indentation fracture toughness variation of Mo_2FeB_2 - αFe cermet prepared through MoB route and sintered at 1350°C .	45
Fig. 3.12	Optical microstructures of Mo_2FeB_2 - αFe and its based cermet prepared through elemental and MoB routes (sintering temperature 1350°C)	
	(a) Mo_2FeB_2 (Elemental route)	
	(b) Mo_2FeB_2 (MoB route)	
	(c) Mo_2FeB_2 -12.43 vol.% αFe (Elemental route)	
	(d) Mo_2FeB_2 -12.43 vol.% αFe (MoB route)	
	(e) Mo_2FeB_2 -25.62 vol.% αFe (Elemental route)	
	(f) Mo_2FeB_2 -25.62 vol.% αFe (MoB route)	45

Fig. 3.13 SEM Fractographs of Mo_2FeB_2 and its based cermets sintered at 1350°C :	
(a) Mo_2FeB_2 (Elemental route)	
(b) Mo_2FeB_2 (MoB route)	
(c) Mo_2FeB_2 -12.43 vol.% αFe (Elemental route)	
(d) Mo_2FeB_2 -12.43 vol.% αFe (MoB route)	
(e) Mo_2FeB_2 - 25.62 vol.% αFe (Elemental route)	
(f) Mo_2FeB_2 - 25.62 vol.% αFe (MoB route)	46
Fig. 3.14 Lattice parameter variation of hard and binder phases in sintered Mo_2FeB_2 - αFe cermets prepared through elemental and MoB routes at different temperatures.	47
Fig. 3.15 Saturation magnetic flux density variation of Mo_2FeB_2 - αFe cermets prepared through elemental and MoB routes and sintered at 1350°C .	48
Fig. 3.16 Corrosion rate of Mo_2FeB_2 - αFe cermets in 10 wt.% HCl and 10 wt.% HF solutions for 10 hours respectively.	48
Fig. 3.17 Particle size distribution of MoB-Fe-Ni powder premixes.	49
Fig. 3.18 Particle size distribution of MoB-Ni powder premixes.	49
Fig. 3.19 % Volume shrinkage variation of $\text{Mo}_2\text{Fe}(\text{Ni})\text{B}_2$ -Fe(Ni) cermets prepared through the MoB route and sintered at 1350°C .	50
Fig. 3.20 Sintered density variation of $\text{Mo}_2\text{Fe}(\text{Ni})\text{B}_2$ -Fe(Ni) cermets prepared through the MoB route and sintered at 1350°C .	50
Fig. 3.21 % Total sintered porosity variation of $\text{Mo}_2\text{Fe}(\text{Ni})\text{B}_2$ - Fe(Ni) cermets prepared through the MoB route and sintered at 1350°C .	51
Fig. 3.22 Densification parameter variation of $\text{Mo}_2\text{Fe}(\text{Ni})\text{B}_2$ - Fe(Ni) cermets prepared through the MoB route and sintered at 1350°C .	52

- Fig. 3.23 Vickers hardness variation of $\text{Mo}_2\text{Fe}(\text{Ni})\text{B}_2$ -
Fe(Ni) cermet prepared through the MoB route
and sintered at 1350°C . 53
- Fig. 3.24 Transverse rupture strength variation of
 $\text{Mo}_2\text{Fe}(\text{Ni})\text{B}_2$ - Fe(Ni) cermet prepared through
the MoB route and sintered at 1350°C . 53
- Fig. 3.25 Indentation fracture toughness variation of
 $\text{Mo}_2\text{Fe}(\text{Ni})\text{B}_2$ - Fe(Ni) cermet prepared through
the MoB route and sintered at 1350°C . 54
- Fig. 3.26 Optical microstructures of $\text{Mo}_2(\text{Fe}_{0.5}\text{Ni}_{0.5})\text{B}_2$
based cermet prepared through the MoB route
(Sintering temperature 1350°C)
- (a) $\text{Mo}_2(\text{Fe}_{0.5}\text{Ni}_{0.5})\text{B}_2$ - 11.51 vol.% $\gamma(\text{FeNi})$
 - (b) $\text{Mo}_2(\text{Fe}_{0.5}\text{Ni}_{0.5})\text{B}_2$ - 24.41 vol.% $\gamma(\text{FeNi})$
 - (c) $\text{Mo}_2(\text{Fe}_{0.5}\text{Ni}_{0.5})\text{B}_2$ - 37.22 vol.% $\gamma(\text{FeNi})$ 54
- Fig. 3.27 SEM Fractographs of $\text{Mo}_2(\text{Fe}_{0.5}\text{Ni}_{0.5})\text{B}_2$ and its
based cermet prepared through the MoB route
(Sintering temperature 1350°C) :
- (a) $\text{Mo}_2(\text{Fe}_{0.5}\text{Ni}_{0.5})\text{B}_2$
 - (b) $\text{Mo}_2(\text{Fe}_{0.5}\text{Ni}_{0.5})\text{B}_2$ - 11.51 vol.% $\gamma(\text{FeNi})$
 - (c) $\text{Mo}_2(\text{Fe}_{0.5}\text{Ni}_{0.5})\text{B}_2$ - 24.41 vol.% $\gamma(\text{FeNi})$
 - (d) $\text{Mo}_2(\text{Fe}_{0.5}\text{Ni}_{0.5})\text{B}_2$ - 37.22 vol.% $\gamma(\text{FeNi})$ 55
- Fig. 3.28 Optical microstructures of Mo_2NiB_2 and its
based cermet prepared through the MoB route
(Sintering temperature 1350°C)
- (a) Mo_2NiB_2
 - (b) Mo_2NiB_2 - 10.88 vol.% Ni
 - (c) Mo_2NiB_2 - 23.74 vol.% Ni 55
- Fig. 3.29 SEM Fractographs of Mo_2NiB_2 and its based
cermet prepared through the MoB route
(Sintering temperature 1350°C).
- (a) Mo_2NiB_2
 - (b) Mo_2NiB_2 - 10.88 vol.% Ni
 - (c) Mo_2NiB_2 - 23.74 vol.% Ni 56

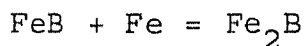
Fig. 3.30	Variation of boride grain mean intercept vs binder content of $\text{Mo}_2\text{Fe}(\text{Ni})\text{B}_2\text{-Fe}(\text{Ni})$ cermets.	56
Fig. 3.31	Variation of binder mean free path vs binder content of $\text{Mo}_2\text{Fe}(\text{Ni})\text{B}_2\text{-Fe}(\text{Ni})$ cermets.	57
Fig. 3.32	Variation of boride phase contiguity vs binder content of $\text{Mo}_2\text{Fe}(\text{Ni})\text{B}_2\text{-Fe}(\text{Ni})$ cermets.	57
Fig. 3.33	Lattice parameter variation of hard and binder phase in $\text{Mo}_2\text{FeB}_2\text{-}\alpha\text{Fe}$ cermets prepared through the MoB route and sintered at 1350°C .	58
Fig. 3.34	Lattice parameter variation of hard and binder phase in $\text{Mo}_2(\text{Fe}_{0.5}\text{Ni}_{0.5})\text{B}_2\text{-}\gamma(\text{FeNi})$ cermets prepared through the MoB route and sintered at 1350°C .	58
Fig. 3.35	Lattice parameter variation of hard and binder phase in $\text{Mo}_2\text{NiB}_2\text{-Ni}$ cermets prepared through the MoB route and sintered at 1350°C .	58
Fig. 3.36	Saturation magnetic flux density variation of $\text{Mo}_2\text{Fe}(\text{Ni})\text{B}_2\text{-Fe}(\text{Ni})$ cermets prepared through the MoB route and sintered at 1350°C .	59
Fig. 3.37	Corrosion rate of $\text{Mo}_2\text{Fe}(\text{Ni})\text{B}_2\text{-Fe}(\text{Ni})$ cermets in 10 wt.% HCl and 10 wt.% HF solutions for 10 hours respectively.	60

SYNOPSIS

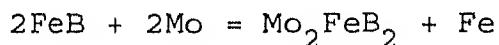
Boride based hard alloys possess high refractoriness, extremely high hardness and excellent wear resistance properties. These intrinsic physical, mechanical and tribological properties have attracted the attention of many researchers in developing the new generation of hard alloys.

The present research is divided into two parts. First part covers the preparation and properties of Mo_2FeB_2 - α Fe (0 - 38.57 vol.%) cermet prepared by two routes viz. elemental route and the MoB route. The effect of binder content and sintering temperature (1250° - 1350°C) on various properties like sintered density, Vickers hardness, transverse rupture strength and indentation fracture toughness were studied. The second part covers the role of different binders viz. Fe, Ni and $\text{Fe}_{0.5}\text{Ni}_{0.5}$ in affecting the properties of individual Mo-boride based cermets, which were produced by MoB route only.

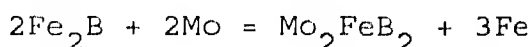
The sintering process undergoing during synthesis in case of such cermets corresponds to reactive liquid phase sintering. In the initial stage, sintering occurs leading to the formation of Fe_2B in the temperature range 452° - 462°C . The exothermic reaction is:



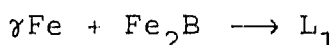
During the progress of solid state sintering a complex Mo_2FeB_2 ternary boride phase is formed above 852°C by the reaction between FeB and molybdenum powders. The exothermic reaction is as follows:



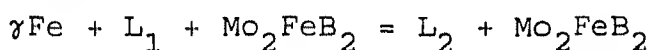
Prior to the liquid phase formation, Mo_2FeB_2 boride phase is also formed above 927°C according to the following exothermic reaction:



In the initial stage of the liquid phase sintering, an eutectic liquid phase is formed above 1092°C by the reaction between γFe and Fe_2B according to the following reaction:



The surface tension associated with the liquid (L_1) exerts a capillary force, due to this capillary action the interconnected pores are filled up by the liquid (L_1) and the particle rearrangement starts in the initial stage of the densification process. In the second stage of the liquid phase sintering above 1142°C another liquid (L_2) phase is formed by the reaction between γFe , Mo_2FeB_2 and L_1 phases. The reaction is as follows:



Fragmentation of γFe phase and Mo_2FeB_2 particle rearrangement in the liquid (L_2) are predominant in this stage of densification process. Particle coarsening of Mo_2FeB_2 phase occurs in the latter stage of the sintering.

The as received powders and ball milled powder premixes were characterized in terms of particle size and shape with the help of Coulter Counter analysis and Scanning Electron Microscopy studies respectively. The powder metallurgy (P/M) processing route involved ball milling in acetone for 38 hrs. with 2 mass % micronized wax powder. Cold compaction of the dried and granulated powder premixes was carried out in the pressure range between 330 to 340 MPa. Vacuum dewaxing was performed at 380°C for 45 mins. followed by vacuum sintering in the temperature range between

1250°C to 1350°C for 1 hour. Phase identification was carried out on diamond polished specimens with the help of X-ray diffraction analysis. Quantitative metallography study viz. boride grain mean linear intercept, binder mean free path and boride phase contiguity was performed with the help of optical metallography. Fractography study in case of TRS fractured specimens was also carried out with the help of Scanning Electron Microscopy study.

It is observed that the straight Mo_2FeB_2 boride prepared through the MoB route after any sintering temperature exhibits lower porosity as compared to the elemental route. This is attributed to the faster solid state reaction in the former. In case of Mo_2FeB_2 - αFe cermets such enhanced densification is quite predominant after 1250°C sintering. The other two sintering temperatures viz. 1300°C and 1350°C exhibit almost identical densification in either processing route. This reflects that the attainment of equilibrium is identical in case of 1300°C and 1350°C sintering temperature in either processing route.

Vickers hardness and Transverse Rupture Strength of Mo_2FeB_2 boride and its αFe bonded cermets increase with the increase in binder content and sintering temperature in either processing route. The MoB processing route exhibits higher value, which is attributed to less volume fraction of % total sintered porosity in the cermets. Mo_2FeB_2 -25.62 vol.% αFe cermet prepared through the elemental route after 1350°C sintering exhibits a maximum hardness and TRS of 1149 VHN and 630 MPa respectively. In case of MoB route, cermet containing 25.63 vol.% αFe binder prepared after

Indentation fracture toughness of Mo_2FeB_2 - αFe cermet prepared through the MoB route after 1350°C sintering increases with the increase in αFe binder content. This is attributed to the fact that the increase in volume fraction of αFe binder toughens the Mo_2FeB_2 - αFe cermet. Mo_2FeB_2 boride based cermet containing 25.62 vol.% αFe binder exhibits a maximum indentation fracture toughness of 10.65 MPa $\sqrt{\text{m}}$.

Saturation magnetic flux density in case of Mo_2FeB_2 - αFe cermet prepared through either route after 1350°C sintering increases with the increase in αFe binder content and decrease in % total sintered porosity. This is attributed to the fact that αFe binder is ferromagnetic in nature and reduction in the porosity level in the sintered cermet decreases the hysteresis loss. Cermet containing 25.62 vol.% αFe binder prepared through the elemental route gives rise to a maximum saturation magnetic flux density of 46.3 T.

Thermal shock resistance (ΔT) of Mo_2FeB_2 - αFe cermet prepared through the MoB route after 1350°C sintering is independent of the binder content and ΔT exhibits $<340^\circ\text{C}$.

The corrosion resistance of the straight Mo_2FeB_2 boride prepared through the MoB route after 1350°C sintering is superior in 10 wt.% HF solution as compared to 10 wt.% HCl solution, whereas, in case of αFe bonded cermet corrosion resistance is superior in 10 wt.% HCl solution. The difference in corrosion potential between Mo_2FeB_2 boride phase and the αFe binder is higher in 10 wt.% HF solution.

Coming to the second part of the investigation, it is evident from the results that αFe and $\gamma(\text{FeNi})$ bonded cermet show a

hardness peak, whereas, Ni bonded cermets show a uniform hardness fall. The peak hardness in Fe(Ni) bonded cermets is attributed to better densification. The fall in hardness after ~12 vol.% Fe(Ni) binder addition is due to the softening effect of Fe(Ni) binder, which is quite predominant in case of nickel bonded cermets. The hardness decrease in case of straight ternary borides follow the order $\text{Mo}_2\text{NiB}_2 \rightarrow \text{Mo}_2(\text{Fe}_{0.5}\text{Ni}_{0.5})\text{B}_2 \rightarrow \text{Mo}_2\text{FeB}_2$. The straight Mo_2NiB_2 ternary boride exhibits a hardness value of 1163 kgf/mm². Mo_2FeB_2 -12.43 vol.% αFe cermet shows a maximum hardness of 1195 kgf/mm².

Transverse rupture strength of $\text{Mo}_2\text{Fe}(\text{Ni})\text{B}_2$ -Fe(Ni) cermets increases rapidly with the increase in Fe(Ni) binder content. This is attributed to the better densification of the cermets with increase in volume fraction of the binder phase which contributes to better composite strengthening. TRS of the cermets decreases in the binder sequence $\text{Ni} \rightarrow \gamma(\text{FeNi}) \rightarrow \alpha\text{Fe}$. Mo_2NiB_2 - 23.74 vol.% Ni cermet shows a maximum TRS of 1380 MPa.

Indentation fracture toughness increases uniformly with the increase in Fe(Ni) binder content with the exception in 37.22 vol.% $\gamma(\text{FeNi})$ bonded cermet, where it shows a rapid decrease. The sequence in indentation fracture toughness variation also follows the pattern identical to TRS. $\text{Mo}_2(\text{Fe}_{0.5}\text{Ni}_{0.5})\text{B}_2$ -24.41 vol.% $\gamma(\text{FeNi})$ cermet shows a maximum indentation fracture toughness of 29.59 MPa√m.

Boride grain mean liner intercept (\bar{I}_α) of Mo_2FeB_2 based cermets increases with the initial binder addition. After 12.43 vol.% αFe binder addition it gets reduced. In case of $\gamma(\text{FeNi})$ bonded cermets, \bar{I}_α reduces initially, with binder addition.

Nickel bonded cermets exhibit a uniform increase in T_{α} with increase in the binder content. Cermets containing 12.43 vol.% αFe , 11.51 vol.% $\gamma(\text{FeNi})$ and 23.74 vol.% Ni binders respectively exhibit maximum boride grain coarsening. In general the coarsening sequence is $\text{Ni} > \gamma(\text{FeNi}) > \alpha\text{Fe}$.

Binder mean free path (\bar{l}_{β}) of $\text{Mo}_2\text{Fe}(\text{Ni})\text{B}_2\text{-Fe}(\text{Ni})$ cermets increases with the increase in binder content, whereas, the boride phase contiguity decreases with the increase in binder content. It is interesting to note that the boride phase contiguity decreases in the binder order $\text{Ni} < \gamma(\text{FeNi}) < \alpha\text{Fe}$.

The saturation magnetic flux density of $\text{Mo}_2\text{FeB}_2\text{-}\alpha\text{Fe}$ and $\text{Mo}_2(\text{Fe}_{0.5}\text{Ni}_{0.5})\text{B}_2\text{-}\gamma(\text{FeNi})$ cermets increases almost linearly with the increase in $\text{Fe}(\text{Ni})$ binder content. It is interesting to note that the αFe bonded cermets show higher saturation magnetic flux density as compared to $\gamma(\text{FeNi})$ bonded ones. This is attributed to higher spin dipole magnetic moment of αFe phase as compared to $\gamma(\text{FeNi})$ binder.

A significant improvement in thermal shock resistance is achieved in case of $\text{Mo}_2(\text{Fe}_{0.5}\text{Ni}_{0.5})\text{B}_2\text{-}\gamma(\text{FeNi})$ and $\text{Mo}_2\text{NiB}_2\text{-Ni}$ cermets with the increase in binder content. These cermets give rise to a thermal shock resistance ΔT equal to 770°C . This is attributed to small difference in coefficient of volume thermal expansion between the hard and binder phases.

Corrosion weight loss study in 10 wt.% HCl and 10 wt.% HF solutions in case of $\text{Mo}_2\text{Fe}(\text{Ni})\text{B}_2\text{-Fe}(\text{Ni})$ cermets reveals that the corrosion resistance follows a trend $\text{Ni} > \gamma(\text{FeNi}) \gg \alpha\text{Fe}$ in either corrosive medium. It is interesting to note that $\text{Mo}_2\text{Fe}(\text{Ni})\text{B}_2\text{-Fe}(\text{Ni})$ cermets, in general, exhibit poor corrosion resistance in

10 wt.% HF solution as compared to 10 wt.% HCl solution, with the exception in nickel bonded cermets, where the values are in proximity. Also the unique feature is that the straight Mo_2FeB_2 corrodes maximum in 10 wt.% HCl solution. The maximum porosity level in Mo_2FeB_2 attributes to more exposed effective surface area to corrosive medium, while lower corrosion potential favours more corrosion. The corrosion potential of the ternary boride increases in the order $\text{Mo}_2\text{FeB}_2 \longrightarrow \text{Mo}_2(\text{Fe}_{0.5}\text{Ni}_{0.5})\text{B}_2 \longrightarrow \text{Mo}_2\text{NiB}_2$, whereas, the binder corrosion potential increases in the order $\alpha\text{Fe} \longrightarrow \gamma (\text{FeNi}) \longrightarrow \text{Ni}$.

CHAPTER I

LITERATURE REVIEW

1.1 INTRODUCTION

The conventional heat, wear and corrosion resistant alloys suffer from the disadvantages of the unstable source of supply of the expensive materials like tungsten, cobalt and lack of combination of superior physical and mechanical properties. To achieve the equivalent or higher property level at the expense of higher production cost, extensive research have been carried out by various authors [1-6]. The recently developed boride based hard alloys serve the above criteria. The boride based hard alloys were first commercially developed in Japan in the end of the last decade (1986) by Japanese firm named Toyo Kohan. These hard alloys are designated by the trade name KH (sintered boride) group. According to their specific properties the KH group has been further divided into four subgroups such as general purpose wear resistant alloys, the corrosion and wear resistant alloys, the heat and wear resistant alloys and the ferromagnetic wear resistant alloys designated by V, C, H and M respectively.

Boride based hard alloys comprise of a hard $M_2M'B_2$ (M = Refractory Metal, M' = Transition Metal of iron group) mixed double boride phase with a metal binder. The binder phases are straight one or alloyed with various transition and refractory metals. These cermets are produced during the liquid phase sintering process. The binder content in these cermets varied from 0 to 40 vol %.

These alloys suffer from the disadvantage of inferior transverse rupture strength, primarily due to poor wettability

between the boride phase and metal binders. The boride based hard alloys are almost equivalent to cemented carbide because of their light weight and superior corrosion resistance property. The specific gravity of such cermets is three fifth of cemented carbide and almost equivalent to steel. The hardness, transverse rupture strength, as well as wear and corrosion resistance properties are also superior to tool steel, high speed steel and stainless steel respectively.

The Fe-B-Mo boride based hard alloys are extensively used as forming tools, machine parts, powder treatment equipment parts and in other various applications.

1.2 Mo-Fe-B BASED CERMETS

1.2.1 Phase Equilibria and Crystal Structures

Reiger et al. [7] established the crystal structure of Mo_2FeB_2 boride phase in the ternary Fe-B-Mo alloy. The Mo_2FeB_2 has tetragonal lattice configuration with the lattice parameter $a = 5.782\text{\AA}$, $c = 3.148\text{\AA}$ and $c/a = 0.544$. The crystal structure is isotype with that of U_3Si_2 super-structure.

Gradyshevsky et al. [8] established the Fe-B-Mo phase equilibria in details at 1000°C . The isothermal ternary Fe-B-Mo phase equilibrium diagram is shown in Fig. 1.1. The authors reported the crystal structures of Mo_2FeB_2 and MoFeB_4 phases in details.

Haschke et al. [9] investigated the isothermal ternary Fe-B-Mo phase equilibria in details at 1050°C , which is shown in Fig. 1.2.

Various phases present in this ternary alloy system, their crystal structures, structure type, lattice parameters as reported

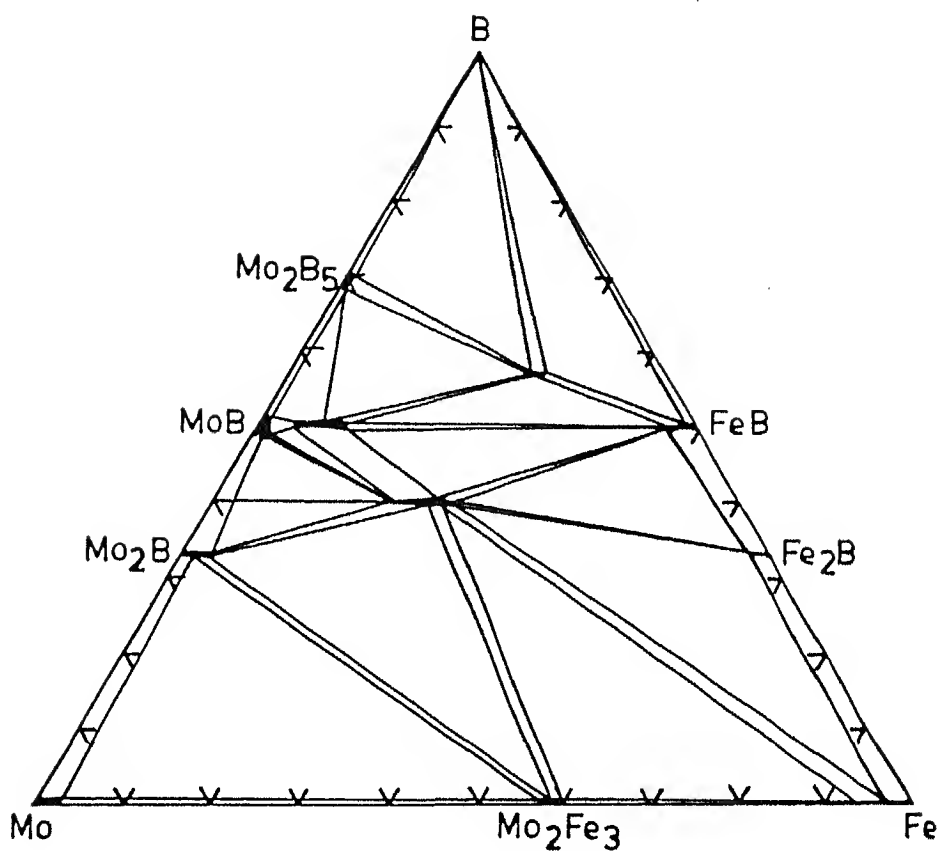


Fig. 1.1. Isothermal Fe-B-Mo ternary equilibrium phase diagram at 1000 °C.

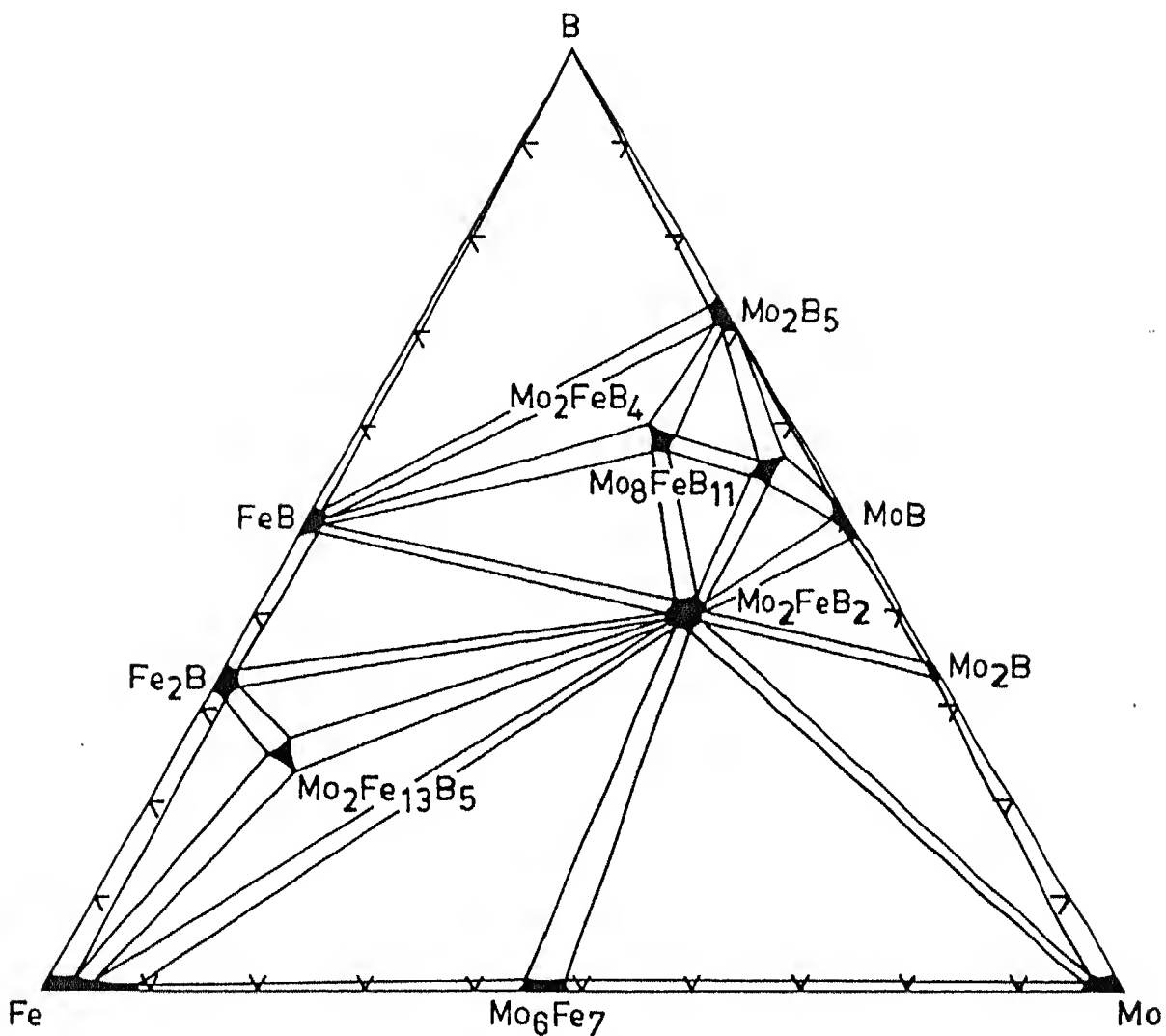


Fig. 1.2. Isothermal Fe-B-Mo ternary equilibrium phase diagram at 1050 °C.

are listed in Table 1.1.

Table 1.1 : Crystallographic details including Theoretical Densities of various Metallic-Intermetallic Binders and Hard Boride Phases in the Ternary Fe-B-Mo Alloy System

Phase	Crystal Struct.	Struct. Type	Lattice Parameter (Å)			Theoretical Density Mg/m ³	Ref
			a	b	c		
αFe	Cubic (BCC)	W	2.8604	-	-	7.8648	52
Mo	"	"	3.1472	-	-	10.2206	53
B	Tetragonal	B	10.1	-	14.28	2.366	54
MoFe	Tetragonal	CrFe	9.218	-	4.813	9.2439	55
Mo ₆ Fe ₇	Hexagonal	W ₆ Fe ₇	4.751	-	25.68	9.5913	56
Mo ₂ B	Tetragonal	Al ₂ Cu	5.547	-	4.739	9.2329	57
Mo ₃ B ₂	"	U ₃ Si ₂	6.002	-	3.146	9.0673	58
MoB	"	MoB	3.105	-	16.97	8.6671	59
MoB ₂	Hexagonal	AlB ₂	3.04	-	3.07	7.9445	60
MoB	Orthorombic	CrB	3.16	8.61	3.08	8.4608	61
Mo ₂ B ₅	Hexagonal	Mo ₂ B ₅	3.011	-	20.93	7.4548	62
FeB	Orthorombic	FeB	4.0587	5.5032	2.947	6.7025	63
Fe ₂ B	Tetragonal	Al ₂ Cu	5.099	-	4.24	7.3807	64
MoFe ₂ B ₄	Orthorombic	Ta ₃ B ₄	3.128	12.70	2.984	7.0282	65
Mo ₂ FeB ₄	"	Ta ₃ B ₄	3.11	14.27	3.19	6.8253	66
Mo ₂ FeB ₂	Tetragonal	U ₃ Si ₂	5.782	-	3.148	8.4991	67

1.2.2 Powder Metallurgy (P/M) Processing and Microstructural Aspects

The initial stage of preparation of Fe-B-Mo ternary alloy is the blending of FeB or iron-boron master alloy powder with pure molybdenum and carbonyl iron powders in the stoichiometric ratio

care of any oxygen in the powder mixture. Paraffin and micronized wax powder are added prior to the mechanical alloying process. The blended powder is subsequently mechanically alloyed in the vibratory mill or in the ball mill. Mechanical alloying is carried out in an inert medium like CH_3OH , $\text{C}_2\text{H}_5\text{OH}$ or in $(\text{CH}_3)_2\text{CO}$ to prevent oxidation of powders as well as to facilitate homogeneous slurry mixing of the blended powder mixture. The mechanically alloyed powder is warm - dried in an oven in vacuum or in an inert atmosphere like He, Ar or N_2 .

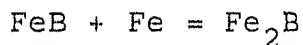
Micronized wax powder (4-5 mass%) added to the blended powder prior to the mechanical alloying process acts as a bonding agent by coating the powder particles during the mechanical alloying process. Paraffin added to the powder mixture reduces the friction between the powder particles.

The warm dried powder is granulated and cold compaction is carried out at a compaction pressure range of 147-265 MPa. Dewaxing is carried out in vacuum ($6.7 - 6.7 \times 10^{-2}$ Pa). The dewaxed specimens are subsequently sintered in vacuum in the temperature range between $1200^\circ - 1327^\circ\text{C}$. The optimum percentage (~0.4 mass %) of graphite powder is added to the powder mixture in order to reduce the oxides present in the as received powder or oxides formed during the mechanical alloying process. According to authors [3] the significant improvement in the mechanical properties are achieved by carbon addition to the powder mixture.

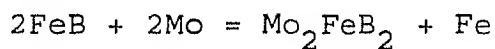
German et al. [10] investigated the liquid phase sintering process in Fe-0-1.1B-0-5 Mo (mass%) ternary alloys. According to them, an iron rich boron (Fe_2B) eutectic liquid phase is formed during the sintering process. The porosity level is quite

significantly reduced by the presence of this liquid phase at the interparticle regions and pore rounding occurs as the sintering proceeds. The molybdenum added to the alloy acts as a ferrite stabilizer. It enhances the diffusion process and thereby leading to the improvement in densification efficiency. At the same time molybdenum degrades the densification efficiency along with the formation of a complex ternary Mo_2FeB_2 boride superhard phase.

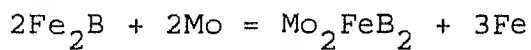
Ide et al. [11] developed an excellent microstructure in Fe-6B-48Mo(% m) ternary alloy by the liquid phase sintering process. The initial stage of solid state sintering process involves the formation of Fe_2B phase in the temperature range between 452°C - 462°C . The exothermic reaction is



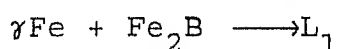
During the progress of solid state sintering process a complex Mo_2FeB_2 ternary boride phase is formed above 852°C by the reaction between FeB and molybdenum powders. The exothermic reaction is as follows:



Prior to the liquid phase formation, Mo_2FeB_2 boride phase is also formed above 927°C according to the following exothermic reaction:



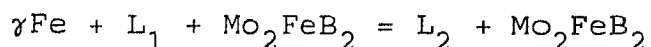
In the initial stage of the liquid phase sintering process, an eutectic type liquid phase is formed above 1092°C by the reaction between γFe and Fe_2B according to the following reaction:



The surface tension associated with the liquid (L_1) exerts a capillary force, due to this capillary action the interconnected

pores are filled up by the liquid (L_1) and the particle rearrangement starts in the initial stage of the densification process.

In the second stage of the liquid phase sintering process, above 1142°C another liquid (L_2) phase is formed by the reaction between γFe , Mo_2FeB_2 and L_1 phases. The reaction is as follows:



Fragmentation of γFe phase and Mo_2FeB_2 particle rearrangement in the liquid (L_2) are predominant in this stage of densification process.

Particle coarsening of Mo_2FeB_2 phase occurs in the latter stage of the sintering process. The optimum mechanical properties are achieved by the proper control of sintered microstructures [11]. The characteristic features of these alloys are that the atomic ratio between Mo and B less than unity favours the formation of L_1 liquid phase, while excessively deficient Mo content facilitates the formation of a brittle Fe_2B phase, which has detrimental effect on the mechanical properties. The optimum atomic ratio between Mo and B $X_{\text{Mo}}/X_{\text{B}} = 0.9$ is best suited for better control of sintered microstructures in the ternary Fe-B-Mo alloy.

1.2.3 Physical and Mechanical Properties

Various physical and mechanical properties of the heat and wear resistance boride based hard alloys are discussed in the present section.

1.2.3.1 Sintered Density and Porosity

The work of German et al. [10] on Fe-0-1.1B-0-5Mo (% m) alloys clearly reveals that the densification rate is little

affected by Mo addition upto 3 mass % in contrast to B. Molybdenum stabilizes the ferrite, the diffusion rate is quite significantly faster in ferrite as compared to the austenitic phase. Boron addition enhances the densification efficiency quite significantly. It forms a low melting (iron rich boron (Fe_2B) + (Fe) eutectic liquid phase. The interparticle regions are completely filled up by the presence of this liquid. The formation of Mo_2FeB_2 complex boride phase gives rise to less densification efficiency as compared to the individual components. Sintered density is also affected by the degree of sintering. In case of sintering at 1200°C for 1 hr. in Fe-B-Mo ternary alloys containing Mo and B atomic ratios close to 1.1, 2.8, 0.1 gave rise to sintered densities approximately 6.69, 6.9, 7.63 Mg/m^3 respectively [10]. The atomic ratio of Mo and B close to unity gave rise to approximately 15% total porosity in the sintered product. In case of higher Mo and B atomic ratio, i.e. $x_{\text{Mo}}/x_{\text{B}} \approx 2.8$ reduced the porosity level upto approximately 12.9 %, it clearly indicated that Mo stabilizes the ferrite, thereby enhances the diffusion process. Lower level of the Mo and B atomic ratios favoured the liquid phase sintering process. The atomic ratio of Mo and B close to 0.1 gave rise to sintered density close to approximately the theoretical value in case of the above isothermal and isochronal sintering condition.

Ide et al. [4] carried out liquid phase sintering on Fe-6B-XMo (X = 0, 15, 30, 38, 43, 48 and 58 mass %) alloys in the partial pressure range between 6.7 to 6.7×10^{-2} Pa, the sintering temperature range between 1077°C to 1327°C for a period of 20 minutes. The sintered density increased monotonically with the

increase in Mo content approximately from 7.5 Mg/m^3 to 8.5 Mg/m^3 . The characteristic feature is that the ultimate sintered density remains almost constant in the above sintering temperature range for isocomposition alloy.

In Fe-B-Mo ternary alloys the density increases primarily with the increase in Mo content. The ultimate sintered density did not vary significantly in the temperature range between 1125°C - 1300°C . Maximum sintered densities as reported [1] in Fe-5B-XMo (X = 40, 44.4, 48.8 mass %) alloys were approximately 7.8, 7.9 and 8.05 Mg/m^3 respectively in case of vacuum sintering in the above mentioned sintering temperature range for a period of 20 minutes. Without carbon addition approximately 96% of the theoretical density was achieved. In Fe-5B-44.4Mo (%m) alloy maximum sintered density close to the theoretical density was achieved by optimum percentage of carbon addition. The atomic ratio of Mo and B close to unity favours the maximum density with the optimum percentage of carbon addition e.g. 0.7 and 1.0 mass% respectively. A reduction stage at 1050°C for 1 hr. prior to the vacuum sintering in the above mentioned sintering parameter gives rise to a maximum sintered density of 8.2 Mg/m^3 , close to the theoretical value.

1.2.3.2 Hardness

The hardness of the heat and wear resistant boride based hard alloys is primarily affected by the presence of sintered porosities and strongly influenced by the presence of complex ternary Mo_2FeB_2 boride phase as well as on the structural morphologies of the sintered cermets.

German et al. [10] investigated that molybdenum addition increases the hardness in the absence of boron, the latter is

having the beneficial effect in the absence of molybdenum. The presence of both molybdenum and boron gave rise to an unsystematic variation in hardness.

In Fe-0-1.1B-0-5Mo (%m) alloys [10] containing equal atom percent of Mo and B corresponds to the stoichiometric atomic ratio of the extremely hard Mo_2FeB_2 boride phase formation. The hardness level increased to 17 HRB in case of the alloy containing Mo and B atomic ratio close to 2.8, the total sintered porosity level decreased to approximately 12.9% in the above sintering condition. Mo and B atomic ratio close to 0.1 gave rise to sintered density very near to the theoretical density value in the above isothermal and isochronal sintering condition. It resulted in a maximum hardness value of 83 HRB. The % total sintered porosity was completely eliminated by the presence of a low melting eutectic liquid phase, this gave rise to the increase in the sintered hardness upto the maximum level.

The addition of Mo in the binary Fe-6 mass% B alloy drastically increased the hardness by the formation of an extremely hard Mo_2FeB_2 complex boride phase. In ternary Fe-6B-XMo (X = 15, 20, 38, 43, 48, 53, 58 mass %) alloys the volume fraction of Mo_2FeB_2 phase increases with the increase in Mo content in the vacuum sintering temperature range between 1077°C to 1327°C for 20 minutes, this resulted in the monotonic increase in the hardness value [4]. The liquid phase sintering process in the above ternary alloys gave rise to maximum densification efficiency. Sintered density close to the theoretical density was achieved by the above process resulting in the maximum sintered hardness value of 88 HRA.

The research of Takagi et al. [1] on Fe-5B-XMo (X = 40.0, 44.4, 48.8 mass %) alloys reveals that the sintered hardness did not vary in a systematic manner in the sintering temperature range between 1125°C-1300°C. The presence of various oxides in the powder compact gave rise to incomplete maximum densification efficiency, it resulted in an unsystematic variation in the sintered hardness. In Fe-5B-44.4 Mo (mass %) alloy the sintered hardness increased monotonically with the increase in γ percent carbon (γ = 0.5, 0.7, 1.0, 1.5 mass %) addition. A reduction stage at 1050°C for 1 hr. prior to the above isothermal and isochronal sintering condition gave rise to approximately constant sintered hardness in each case. The optimum percentage of carbon addition (0.7 mass %) resulted in a minimum residual oxygen content in the powder compact. Higher percentage of carbon addition gave rise to higher residual oxygen content, which resulted in incomplete reduction of the oxides and the inhibition of low melting eutectic liquid phase in the interparticle regions. The increase in the residual carbon content of the alloys gave rise to the increase in the volume fraction of $\text{Fe}_3(\text{BC})$ phase along with the complex Mo_2FeB_2 boride phase in the αFe binder. The sintered hardness increased from 84 HRA to 90 HRA with the increase in residual carbon content.

1.2.3.3 Tensile Strength and Ductility

The sintered strength is inversely proportional to the total sintered porosities and strongly depends on the nature and morphologies of various boride phases. Fe-0-1.1B-0.5 Mo (%m) alloys [10] after sintering at 1200°C for 1 hr. in dry hydrogen atmosphere gave rise to sintered strength behaviour similar to

density and hardness trend as described earlier. The Mo and B atomic ratio greater than unity resulted in the increase in tensile strength from 200 to 260 MPa approximately. Equal Mo and B stoichiometric atomic ratio resulted in the formation of a brittle Mo_2FeB_2 complex ternary hard boride phase. The excess Mo stabilizes the ferrite binder, causing an increase in the percentage elongation from 8 to 11% approximately. The molybdenum and boron atomic ratio less than unity favoured the formation of a low melting iron rich boron extremely brittle (Fe_2B) phase. In this region the tensile strength increased approximately from 210 to 385 MPa at the expense of ductility. Ductility drastically reduced approximately from 11.5% to zero with the increase in the volume fraction of Fe_2B brittle phase.

1.2.3.4 Transverse Rupture Strength (TRS)

The transverse rupture strength primarily depends on the porosities in the powder compact and is strongly affected by the nature and morphologies of the complex boride phases in the sintered cermet.

Takagi et al. [1] investigated that vacuum sintering of Fe-5B-xMo (X = 40.0, 44.4, 48.8 mass%) alloys in the temperature range between 1125°C to 1300°C for 20 minutes gave rise to a monotonic increase in the transverse rupture strength in the lower sintering temperature range, while it decreased drastically beyond the critical temperature in the higher sintering temperature range. Maximum transverse rupture strength of 1630 MPa was achieved at 1250°C for the stoichiometric Mo and B atomic ratio. The Mo and B atomic ratio close to unity in Fe-5B-44.4Mo (%m) alloy favoured the formation of maximum volume percent of Mo_2FeB_2

boride phase along with the α Fe binder. This resulted in the increase in transverse rupture strength. Lower atomic ratio of Mo and B i.e. $X_{\text{Mo}}/X_{\text{B}} \approx 0.9$ gave rise to the formation of an intrinsic brittle Fe_2B boride phase along with the complex Mo_2FeB_2 boride phase in the α Fe binder. The transverse rupture strength drastically reduced by the presence of intrinsic brittle Fe_2B boride phase. A reduction stage at 1050°C for 1 hr. prior to vacuum sintering in the above sintering condition in $y\% \text{C}$ ($y = 0.5, 0.7, 1$ mass %) added alloy significantly increased TRS. The maximum TRS value of 2050 MPa was achieved in case of vacuum sintering at 1250°C . Higher percentage (1 mass %) carbon addition resulted in incomplete reduction of oxides and the formation of $\text{Fe}_3(\text{BC})$ phases in the powder compact. Incomplete densification resulted in significant reduction in TRS value.

Ide et al. [4] investigated that the TRS in Fe-6 mass% B binary alloy drastically increased with the increase in Mo content, the addition of Mo gave rise to the formation of high strength Mo_2FeB_2 complex boride phase. In Fe-6B-XMo ($X = 15, 30, 38, 43, 48, 53, 58\% \text{m}$) alloys vacuum sintering in the temperature range 1077°C to 1327°C for 20 minutes resulted in a monotonic increase in TRS. At the same time it decreased with the increase in sintering temperature. Maximum TRS of 1900 MPa was achieved in Fe-6B-48Mo (%m) alloy after sintering at 1227°C for the above isochronal sintering condition. The molybdenum and boron atomic ratio close to 0.9 gave rise to a small volume fraction of extremely brittle Fe_2B boride phase along with the complex Mo_2FeB_2 boride grains along with the α Fe binder. The fractograph reveal the ductile failure of the α Fe binder along with the

intergranular failure between Mo_2FeB_2 complex boride grains and the α Fe binder. The alloy containing Mo and B atomic ratio close to 0.7 gave rise to approximately 22 vol % of Fe_2B boride phase. The fractographs reveal the transgranular fracture mode due to intrinsic brittleness of Fe_2B boride grains. The TRS was significantly reduced by the presence of the extremely brittle Fe_2B boride phase. In 53 mass % Mo containing alloy sintered at high temperature resulted in a drastic reduction in TRS. Failure took place by the transgranular brittle fracture mode. The complex Mo_2FeB_2 ternary boride grain coarsening at high temperatures played a predominant role in the significant reduction in the TRS value.

1.3 Mo-Fe-Ni-B BASED CERMETS

1.3.1 Phase Equilibria and Crystal Structures

There is lack of sufficient information available regarding the quaternary Fe-B-Mo-Ni alloy equilibrium phase diagram. Takagi et al. [3] investigated various phases in the above quaternary alloy system (0-10 mass % Ni addition in the ternary Fe-5B-44.4 Mo alloy), namely complex Mo_2FeB_2 boride phase, α Fe, γ Fe and Fe_2B phases in the ferrite (α), austenitic (γ) and martensitic (α') binders respectively. Ferrite is the interstitial solid solution of carbon in bcc αFe . Austenite has the cubic lattice configuration, the structure type is isotype with that of NaCl structure. Martensite (FeC) phase has the metastable body centered tetragonal lattice configuration. Ni addition in the ternary Fe-5B-44.4 Mo (% m) alloy resulted in the formation of a substitutional solid solution with Fe, the crystallographic details of which has not been investigated.

1.3.2 Powder Metallurgy (P/M) Processing and Microstructural Aspects

Takagi et al. [3] investigated the P/M processing of the quaternary Fe-5B-44.4Mo-XNi (X = 1, 2.5, 5, 7.5, 10 mass %) alloys. It consisted of the milling of the Fe-14.9B (% m) master alloy powder along with pure molybdenum, carbonyl nickel and carbonyl iron powders in the stoichiometric ratio. Graphite powder (0.4 %m) was added in the powder mixture in order to reduce any oxides formed during the milling process. Milling was carried out in an inert medium like acetone with 5 mass % paraffin. Cold compaction was performed at a compaction pressure of 147 MPa followed by dewaxing and subsequently vacuum sintering at 1250°C for 20 minutes. Ni addition in the ternary Fe-5B-44.4 Mo (% m) alloy enhanced the liquid phase sintering process and corrosion resistance quite significantly. The sintered microstructures mainly consisted of the complex Mo_2FeB_2 ternary boride phase along with the small volume fraction of intrinsic brittle Fe_2B boride phase in the ferrous binder. The characteristic features of these quaternary alloys were that, with the increase in Ni content from 1 to 2.5 (mass %) the binder phase transformed from ferritic (α) to martensitic (α') phase. Ni content at 5 mass % or above resulted in the formation of austenitic (γ) binder phase. The Auger Electron Spectroscopy revealed that Ni addition in the Fe-5B-44.4 Mo (% m) ternary alloy resulted in the formation of substitutional solid solution of the ferrous binder, the crystallographic details of which was not clear.

1.3.3 Physical and Mechanical Properties

The important physical and mechanical properties in the quaternary Fe-B-Mo-Ni alloys related to the research, such as, the

sintered density, hardness and transverse rupture strength are described in this section.

1.3.3.1 Sintered Density

Sintered density is primarily dependent on the volume fraction of the porosities in the sintered cermets. Ni addition strongly enhanced the liquid phase sintering process thereby resulting in a significant increase in the densification efficiency [3]. The sintered density increased monotonically from 8.21 to 8.28 Mg/m³ with the increase in Ni content from 0 to 10 mass%.

1.3.3.2 Hardness

Sintered hardness is primarily dependent on the nature and morphologies of the pores and is strongly affected by the microstructural morphologies of various boride phases in the sintered cermets. Hardness value increased monotonically from approximately 86.5 to 87.5 HRA with the increase in Ni content from 1 to 5 mass%. The sintered hardness drastically reduced to 84.8 HRA in case of alloy containing 10 mass% Ni [3].

1.3.3.3 Transverse Rupture Strength (TRS)

The transverse rupture strength property [3] of the quaternary Fe-5B-44.4Mo-XNi (X=1,2.5,5,7.5,10 mass%) alloys are primarily dependent on the pore morphologies of the sintered cermets. It is strongly affected by the microstructural morphologies of the various boride phases as well as on the characteristics of various binder phases in the sintered cermets. TRS value increased approximately from 2.1 GPa to a maximum of 2.24 GPa with the increase in nickel content from 1 to 2.5 mass%, and was drastically reduced beyond the optimum nickel content level.

Minimum value of TRS was reported as 1.4 GPa in case of alloy containing 10 mass% nickel. Alloy containing 2.5 mass% nickel resulted in the formation of a comparatively high strength martensitic (α') binder phase and it gave rise to a maximum TRS. Above this nickel content the TRS drastically reduced by the stabilization of the comparatively low strength austenitic (γ) binder phase.

1.4 MO-Ni-B BASED CERMETS

1.4.1 Phase Equilibria and Crystal Structures

Very little research has been carried out on the ternary Mo-Ni-B alloy system. Kolomystesev and Moskaleva [12] established the ternary Mo-Ni-B alloy isothermal equilibrium phase diagram up to 50 atom% boron addition at 800°C, 1000°C and 1200°C respectively. The isothermal ternary equilibrium phase diagrams at 1000°C and 1200°C are identical ones. Isothermal ternary Mo-Ni-B alloy equilibrium phase diagram at 800°C and 1000°C/1200°C are shown in the Fig. 1.3 and 1.4. Various metallic, intermetallic and boride phases corresponding to 1000°C/1200°C isothermal equilibrium phase diagram are Mo, Ni, MoNi, MoB, Mo₂B, Mo₂NiB₂, NiB, Ni₂B, Ni₃B and Ni₄B₃ respectively. Isothermal ternary Mo-Ni-B equilibrium phase diagram at 800°C contains the above phases along with Ni₄Mo and Ni₃Mo intermetallic phases. Mo₂NiB₂ has a tetragonal lattice configuration [13]. The structure types isotype with that of U₃Si₂ superlattice configuration [7]. The ternary Mo₂NiB₂ complex boride phase also crystallizes to an orthorhombic crystal lattice configuration [13]. The structure type is isotype with that of W₂CoB₂ superstructure [14]. Various crystallographic details including theoretical densities of these

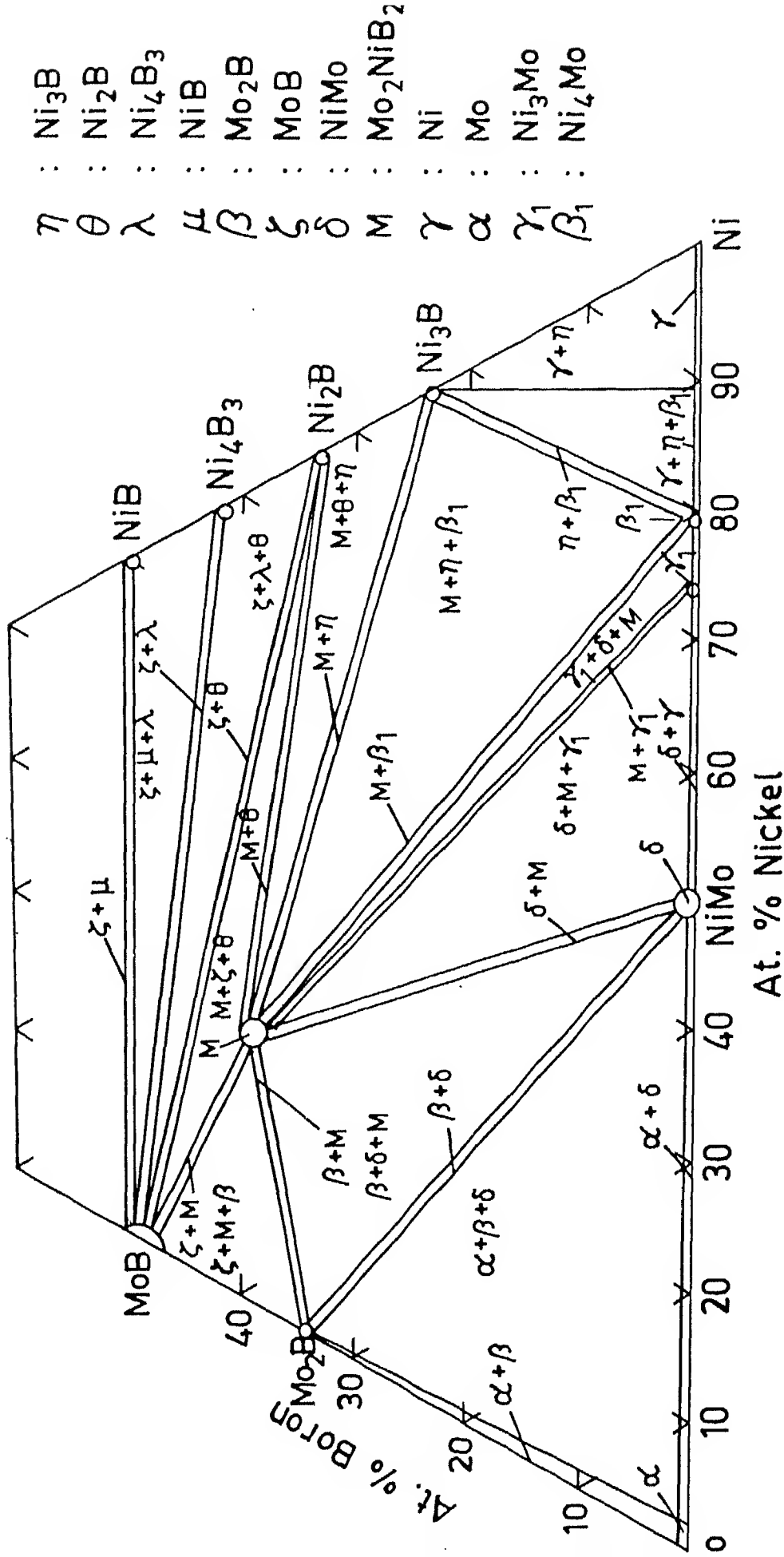


Fig. 1.3. Isothermal Section of Molybdenum - Nickel - Boron Phase Diagram at 800 °C.

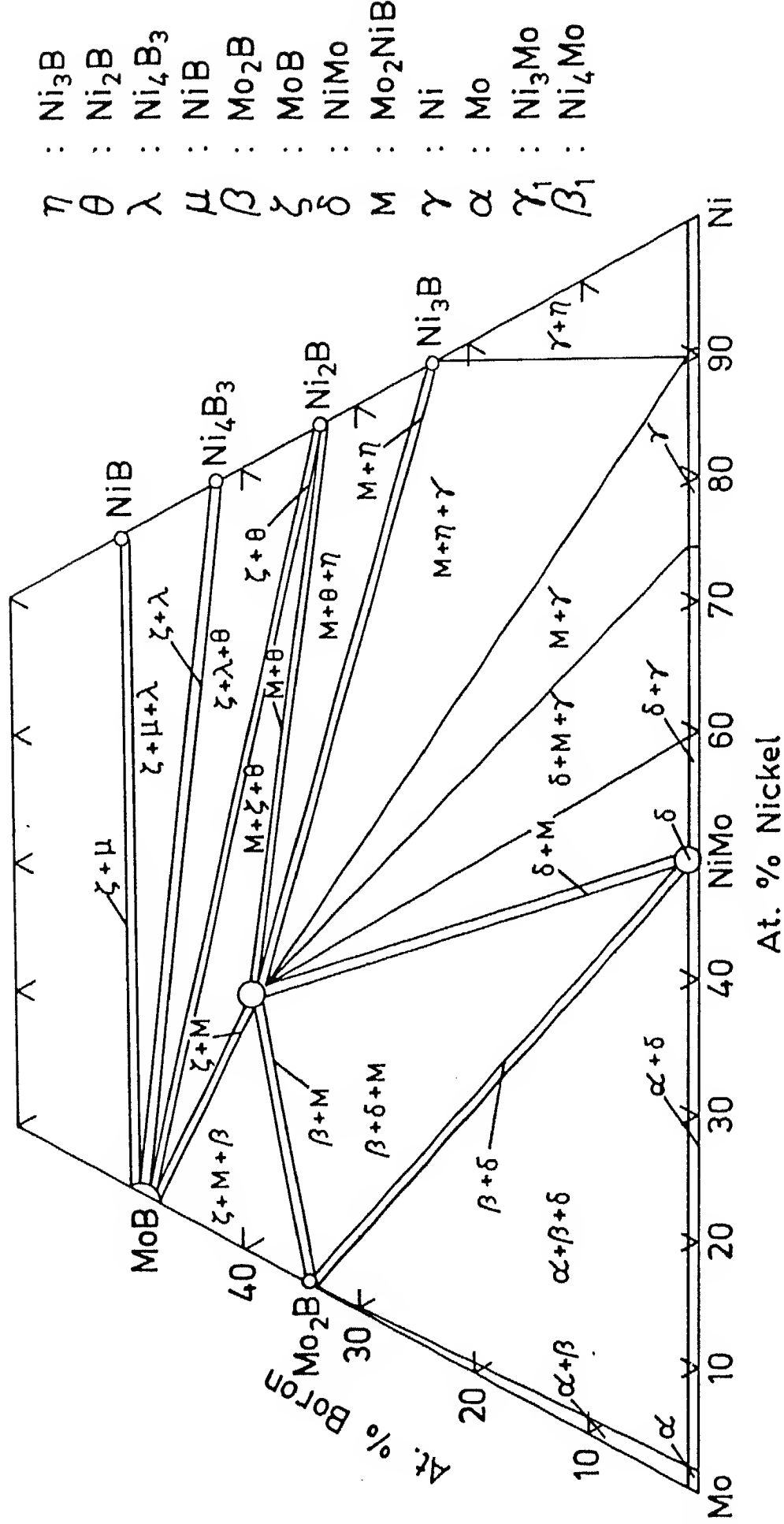
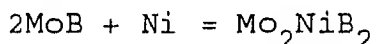


Fig. 1.4. Isothermal Section of Molybdenum - Nickel - Boron Phase Diagram at 1000 / 1200 °C.

metallic intermetallic binders and superhard boride phases are listed in the Table 1.2.

1.4.2 Powder Metallurgy (P/M) Processing and Microstructural Aspects

The powder metallurgy (P/M) processing route of Mo_2NiB_2 boride based cermets is identical to that of Mo_2FeB_2 boride based cermets as described in section 1.2.2. The P/M processing of Mo_2NiB_2 boride based cermets followed by Komai et al. [13] involved the ball milling of MoB powder, pure Ni and pure Mo powders in acetone, followed by compaction of the powder mixture and subsequent vacuum sintering of the green compact at 1300°C for 20 minutes. The authors [15] investigated the mechanism of liquid phase sintering process of Mo_2NiB_2 boride based cermets by using a ternary model alloy containing Ni-6B-58.6Mo (%m). During the first stage of solid state sintering process the complex Mo_2NiB_2 ternary boride phase is formed below 955°C according to the following reaction:



In the second stage above 955°C , the quasi-eutectic reaction between the Mo_2NiB_2 and Ni based binder phase forms an eutectic liquid and considerable densification of the compact occurs by particle rearrangement and solution/reprecipitation of Mo_2NiB_2 boride phase. The sintered microstructures mainly consisted of uniform distribution of Mo_2NiB_2 boride grains with nickel based binder. The complex Mo_2NiB_2 ternary boride phase prepared by the above process had an orthorhombic lattice configuration [14] as described in the previous section.

Table 1.2 : Crystallographic details including Theoretical Densities of various Metallic-Intermetallic Binders and Hard Boride Phases in the Ternary Mo-Ni-B Alloy System

Phase	Crystal Struct.	Struct. Type	Lattice Parameter (Å°)			Theoretical Density Mg/m ³	Ref
			a	b	c		
Mo	BCC	W	3.1472	-	-	10.2206	53
Ni	FCC	Cu	3.5238	-	-	8.9116	68
MoNi ₄	Tetragonal	MoNi	9.108	-	8.852	9.7913	69
Ni ₄ Mo	Tetragonal	MoNi ₄	5.720	-	3.564	9.4201	70
Ni ₃ Mo	Orthorhombic	Cu ₃ Ti	5.064	4.224	4.448	9.4961	71
MoB	Tetragonal	MoB	3.105	-	16.97	8.6671	59
Mo ₂ B	Tetragonal	Al ₂ Cu	5.547	-	4.739	9.2323	57
NiB	Orthorhombic	CrB	2.936	7.38	2.968	7.1799	72
Ni ₂ B	Tetragonal	Al ₂ Cu	4.991	-	4.247	8.0503	73
Ni ₃ B	Orthorhombic	Fe ₃ C	4.392	5.223	6.615	8.1822	74
Ni ₄ B ₃	Orthorhombic	Ni ₄ B ₃ [*]	11.96	2.98	6.57	7.5809	75
Ni ₄ B ₃	Monoclinic	Ni ₄ B ₃	6.430	4.882	7.818	7.4325	76
Mo ₂ NiB ₂	Tetragonal	Mo ₂ NiB ₂	10.036	-	11.952	8.2601	76
Mo ₂ NiB ₂	Orthorhombic	W ₂ CoB ₂	7.075	4.557	3.179	8.8198	15

1.4.3 Mechanical Properties

Among the various mechanical properties, sintered hardness and transverse rupture strength (TRS) as available in the literature are described below.

1.4.3.1 Hardness

Komai et al. [13] reported that Mo₂NiB₂ boride based sintered cermet containing 23 vol.% nickel binder phase gives rise to a hardness value of 85 HRA at room temperature.

1.4.3.2 Transverse Rupture Strength (TRS)

The TRS of the Mo-6B-35.4Ni (% m) ternary alloy is strongly affected by the grain size and structural morphologies of hard boride phases and binder phases. A TRS value of approximately 1.7

GPa was reported at room temperature [13].

1.5 WEAR BEHAVIOUR OF BORIDE BASED CERMETS

The boride based hard alloys have superior wear resistant properties. Takagi et al. [16] studied the sliding wear property in details along with the abrasive wear property. The sliding wear test consisted of pressing a fixed sintered specimen with a constant load against a rotating standard wheel (e.g., JIS SKH3, ASTM T-4 equivalent, HRA 80.4 and SUS 440C, HRA 80.0 etc.). The specific wear rate (S.W.R.) is defined as the loss of volume of the sintered material during sliding wear per unit load per unit sliding distance as given by the following formula:

$$\text{S.W.R.} = \frac{954.93 (m_1 - m_2)}{L r n T \rho} \quad \text{mm}^2 / \text{kgf}$$

where

m_1 = Mass of the sintered specimen before the test (gms)

m_2 = Mass of the sintered specimen after the test (gms)

L = Applied load (kgf)

ρ = Density of the sintered specimen (Mg/m^3)

r = Radius of the wheel (cm)

n = r.p.m.

T = Time (sec.)

It was pointed out by various authors [16] that the SUS 440 C wear test at a constant load of 18.86 kgf with a sliding distance of 600 m having the sliding velocities 0.62, 0.94, 1.65 m/s gave rise to the specific wear rate of 4.337×10^{-8} , $36.63 \times 10^{-8} \text{ mm}^2/\text{kgf}$ respectively.

Another sliding wear test with the identical specimen and wheel material with the sliding velocities 0.62, 0.94, 1.65, 2.38,

4.39 m/s gave rise to the specific wear rate of 0.649×10^{-8} , 1.022×10^{-8} , 0.468×10^{-8} , 0.255×10^{-8} , 0.123×10^{-8} mm²/kgf respectively under identical test conditions.

During the abrasive wear test a fly ash (CaO-60 SiO₂-20 Al₂O₃ etc. (mass%)) with an average particle size of 17 µm was blasted on the sintered specimen at an angle of 0.789 rad. for 30 minutes. It was established that the Fe-5.4B-46.6Mo-1.9Cr-2.9Ni (%m) boride based hard alloy exhibited superior wear resistant property.

Takagi et al [16] studied the abrasive wear behaviour [ASTM B611-76] in the boride based hard alloys containing Fe-5B-43 Mo-8Cr-2.5Ni-XC (X=0.014, 0.073, 0.102, 0.156 mass%). The spherical silica-water abrasive wet slurry concentration as reported was 1 kg/l with an average particle size of 10 µm. It was found out that the abrasive wear resistance increases with the increase in the volume fraction of the boride phases in the martensitic binder.

SUS 440 C sliding wear test [18] with a final load of 18.86 kgf with a sliding distance of 600m having the velocities 0.62, 0.94, 2.38, 4.39 m/s respectively resulted in a superior sliding wear resistance in the V 30 (Fe-5.4B-46.6 Mo-2.9 Ni-1.9Cr (%m)) boride based hard alloys.

1.6 CORROSION BEHAVIOUR OF BORIDE BASED HARD ALLOYS

Corrosion weight loss, high temperature oxidation and potentiodynamic studies of boride based hard alloys as available in literatures are described in the following sections.

1.6.1 Corrosion Weight Loss Study

Takagi et al [17] presented corrosion data on several boride based hard alloys (KHM) grade : Fe-3-7B-23-54Mo-1-25Cr-1- 8Ni (%m)

using various corrosive media especially in 10% HCl, 10% HNO₃, Conc. H₂SO₄, Conc. H₃PO₄, 10% CH₃COOH, 15% NaOH, 15% KOH, sea water and drinking water at room temperature as well as in Coca-Cola and a model solution of tomato juice (4.5 g Citric acid + 50 g Sugar + 5 g Sodium Chloride + 42 g Sodium Nitrate/l, adjusted pH 4.06 with Sodium Citrate) at 80°C for 10/20 hours. Coca-Cola and tomato juice were used as corrosive media in reference to can making tool.

Komai et al [18] carried out corrosion weight loss study in Mo₂FeB₂ boride based hard alloys containing Fe-5.5B-44.4 Mo-XNi (X=0, 1, 2.5, 5, 7.5, 10 %m)) using a non-oxidizing 10 wt% HCl solution at 27°C for 24 hours. It was pointed out that the corrosion resistance increased with the increase in Ni binder content. Corrosion weight loss study in Mo₂FeB₂ boride based hard alloys containing Fe-5.5B-44.4Mo-XCr (X= 0, 2.5, 5, 10, 15 (%m)) in an oxidizing 10 wt% HNO₃ solution for the above identical conditions revealed that corrosion resistance also increased with the increase in Cr binder content. The authors also performed the corrosion weight loss study in case of four Mo₂FeB₂ boride based model hard alloys containing Fe-6.0B-47.5Mo-2.5Cr-3.0Ni, Fe-6.0B-46.0Mo-2.5Cr-6.5Ni, Fe-5.0B-42.5Mo-10.0Cr-3.0Ni, Fe-5.5B-41.5Mo-20.0Cr -8.0Ni (%m) using 10 wt% HCl and 10 wt% HNO₃ solutions. It was pointed out that high Ni containing alloys exhibited superior corrosion resistance in 10 wt% HCl solution with the exception in case of 10Cr-3Ni(%m) alloy. This was attributed to severe localized corrosion of binder phases. In 10 wt% HNO₃ solution corrosion resistance increased with the increase in Cr content in the ferrous binder.

In another investigation Komai et al. [14] performed the corrosion weight loss study in Mo_2NiB_2 boride based cermets containing Ni-6.0B-58.6 Mo-XCr (X=0, 5, 10, 15 (%m)) using 10wt% HCl and 10 wt% HNO_3 solutions at 40°C for 10 hours. It was found that the corrosion resistance increased with the increase in Cr content. The authors also reported that corrosion resistance of Mo-Ni-Cr boride based Cermets in 10 wt.% HCl solution exhibited superior corrosion resistance than that of cemented carbide (WC-10 Co), P/M high speed steel (Fe-12.9Cr-5.2V-2.6C-1.8 Mo), SUS 405 ferritic stainless steel (Fe-11.5-14.5Cr-<0.6Ni- <0.12C-<1Si) SUS 440C martensitic stainless steel (Fe-16-18Cr-0.6Ni-<0.95-1.2C-<1Si), SUS 316L austenitic stainless steel (Fe, 16-18Cr, 12-16Ni, 2-3Mo <0.03C<1Si), SUS 304 austenitic stainless steel (Fe, 18-20Cr, 8-11Ni <0.08C, 1Si), SKD 11 tool steel (Fe, 11-13Cr, 0.8-1.2Mo, 0.2-0.5V, 1.4-1.6C), Hastelloy C (Ni, 14.5-16.5Cr, 15-17Mo, 4-7Fe, 3-4W, 2.5Co) respectively. In 10wt% HNO_3 oxidizing solution non Cr containing cermet exhibited less corrosion resistance than those of cemented carbide, Hastelloy C and was almost in proximity to high speed steel and SKD 11 tool steel respectively.

Corrosion weight loss study in 10 wt% HF solution also revealed quite significant improvement in corrosion resistance with the increase in Cr content [15]. The authors also found that the corrosion resistance of Mo-Ni-Cr boride based cermets in 10 wt% HF solution was better than those of cemented carbide (WC-10 wt% Co), powder metallurgy (P/M) high speed steel, stainless steels (SUS 405, 440C, 316L and 304) and an alloy steel and comparable to that of Hastelloy C respectively.

1.6.2 High Temperature Oxidation Studies

Komai et al [13] carried out high temperature oxidation studies of Mo_2NiB_2 boride based cermets containing Ni-6B-58.6Mo-XCr (X=0, 5, 10, 15 (%m)) in air at 900°C for 1 hour. It was found that the corrosion resistance increased with the increase in chromium content. It was also reported that the corrosion resistance of Mo_2NiB_2 boride based cermets was superior to SKD 11 tool steel (Fe, 11-13Cr, 0.8-1.2Mo, 0.2-0.5V, 1.4-1.6C (%m)) and were almost in proximity to SUS 304 austenitic stainless steel (Fe, 18-20Cr, 8-11Ni, <0.8C, <1Si (%m)).

1.6.3 Potentiodynamic Studies

Komai et al [18] carried out potentiodynamic studies in Mo_2FeB_2 boride based model hard alloys of compositions, Fe-6.0B-47.5Mo -2.5Cr-3.0Ni, Fe-6.0B-46.0Mo-2.5Cr-6.5Ni, Fe-5.0B -42.5Mo -10.0Cr-3.0Ni, Fe-5.5B-41.5Mo-22.0Cr-8.0Ni(%m), using a non-oxidizing 10 wt% HCl and an oxidizing 10 wt% HNO_3 solutions at 27°C. It was found that the corrosion potential of Mo_2FeB_2 complex boride phase in 10 wt% HCl solution ranged from approximately 0 to 50 mv with respect to Ag/AgCl electrode. The corrosion potential of the binder phase was reported in the range from 450 mv to -280 mv. Preferential attack of the binder phase was noticed because the ferrous binder was more active than the complex Mo_2FeB_2 boride phase. The authors also reported that the corrosion potential of the complex Mo_2FeB_2 boride phase in 10 wt% HNO_3 solution ranged from approximately 100 to 200 mv, whereas the ferrous binder had a wider range of corrosion potential from -250 to 250 mv. Preferential attack of the binder phase in lower chromium containing cermets was reported because of lower

corrosion potential of the binder phase with respect to the complex Mo_2FeB_2 boride phase. The transition of localized corrosion phase from ferrous binder to the complex Mo_2FeB_2 boride phase was found with increase in chromium content.

1.7 Scope of the Present Investigation

Not much research has been carried out on the Mo_2FeB_2 ternary boride, only the isothermal sections of Fe-B-Mo ternary alloy system at 1000°C and 1050°C have been investigated in details [8,9]. Similarly isothermal sections of Ni-B-Mo ternary alloy systems at 800°C , 1000°C and 1200°C have been reported [12]. The crystal structure of Mo_2FeB_2 is isotype with that of U_3Si_2 superstructure [7], while that of Mo_2NiB_2 corresponds to W_2CoB_2 superstructure [14].

In the present investigation an attempt has been made to prepare Mo_2FeB_2 - α Fe cermets by two routes viz elemental route where Mo, Fe and B powders were used and the other as MoB route, where MoB and iron were selected. Unlike Takagi et al [1] process the starting boride presently was MoB in place of FeB. An attempt has been made to study the effects of α -iron binder addition (0-38.57 vol%) and sintering temperature on various physical, mechanical, magnetic, thermal shock resistance and corrosion properties on these cermets.

Komai et al [13] also investigated the reaction sintered Mo_2NiB_2 based cermets in which certain interesting properties were reported. The literature survey reveals that no systematic work has been done on partly replacing the iron binder in Mo_2FeB_2 based cermets by nickel. As nickel is much more costlier than iron, such cermet design would be of great significance from the

technoeconomic view point. A possible trade off may be permissible in certain cases. In addition, literature does not systematically mention the effect of the increase in the binder volume fraction on the resultant properties of the ternary boride based particulate composites. An attempt is made to fill this gap too.

CHAPTER II

EXPERIMENTAL PROCEDURE

The detailed experimental procedure carried out in the present study are described in this chapter.

2.1 RAW MATERIALS

The raw materials with specific powder characteristics, used in the present research, are described below.

2.1.1 Carbonyl Iron Powder

The SF grade carbonyl iron powder manufactured by GAF Corporation, USA was used. Its chemical compositions and powder characteristics are as follows.

Chemical Compositions : Apparent Density : 2.26 Mg/m^3

High Purity - 99.99% Average Particle Size : $2.17 \mu\text{m}$

2.1.2 Boron Powder

The boron powder manufactured by Aldrich Chemical Company Inc., USA was used. Its chemical compositions and powder characteristics are given below:

Chemical Compositions : Apparent Density : 0.82 Mg/m^3

High Purity - 99.99% Average Particle Size : $3.72 \mu\text{m}$

2.1.3 Molybdenum Powder

The molybdenum powder manufactured by Metallwerk Planse, Austria was used in the present research. Its powder characteristics are as follows:

Chemical compositions : Apparent Density : 1.15 Mg/m^3

High Purity - 99.99% Average Particle Size : $2.11 \mu\text{m}$

2.1.4 Nickel Powder

Type 123 grade INCO nickel powder supplied by INCO EUROPE LTD. was used. Its various properties are given below:

Chemical Compositions : Apparent Density : 2.03 Mg/m^3

C 0.06% Average Particle Size : $1.59 \mu\text{m}$

Fe 0.005%

O 0.05%

Co 0.0003%

N 0.003%

S 0.003%

Other elements 0.001%

Ni Balance

2.1.5 Molybdenum Boride (MoB) Powder

The molybdenum boride (MoB) powder manufactured by CERAC Inc. U.S.A. was used. Its chemical compositions and powder characteristics are as follows:

Chemical Compositions Apparent Density : 1.98 Mg/m^3
(%m)

Mo 89.82% Average Particle Size : $2.16 \mu\text{m}$

Al 0.03

Ca 0.01

Fe 0.005

Mg 0.13

Si 0.01

Ti <0.001

B Balance

2.1.6 Paraffin Wax Powder

Source : La Ceresene, France

Melting Point : $60 - 62^\circ\text{C}$

Density at 25°C : 0.88 Mg/m^3

Maximum Oil Percentage : 0.07

Acidity Index : Nil

2.2 POWDER CHARACTERIZATION

The as received powders were characterized for particle shape, particle size and its distribution and apparent density. The ball milled powder premixes were characterized for particle size distribution.

2.2.1 Particle Shape

The as received powders were mixed with acetone and stirred well and also ultrasonically agitated. Few drops of turbid acetone containing powder specimen was taken on a polished brass/aluminium stub and dried at room temperature. The powder particle morphology was studied in the JEOL-JSM 840A SEM using 10-15 kV operating voltage in the Secondary Electron Imaging mode.

2.2.2 Particle Size

The particle size of the as received and milled powder premixes were characterized with the help of Z_B Coulter Counter. The principle is based on the change in electrical resistance when powder particles suspended in electrolyte passes through a small aperture. The change in the electrical resistance produces a voltage impulse which is proportional to the particle volume, thereby, the particle size is proportional to the cube root of particle volume. The number of counts (voltage impulse) were measured at various lower and upper thresholds with various current and amplifications. 1% NaCl electrolyte with coulter dispersant was used for analysis.

The average particle size (d_{av}) was calculated from the particle size distribution according to the formula given below:

$$d_{av} = \frac{\sum_{i=1}^n \frac{\% m_i}{d_i^2}}{\sum_{i=1}^n \frac{\% m_i}{d_i^3}} \quad \mu m$$

where, $\%m_i$ = mass % oversize

2.2.3 Apparent Density (ρ_{ap})

The apparent density of as received powders were measured by using Hall Cup. The apparent density was calculated according to the formula :

$$\rho_{Ap} = \frac{m}{V} \text{ Mg/m}^3$$

where, m = Mass of the powder filling the Hall Cup (g)

V = Volume of the Hall Cup (25 cm³)

2.3 POWDER METALLURGY (P/M) PROCESSING

Mo₂FeB₂ boride based cermets were prepared from the elemental carbonyl Fe, B and Mo powders (Elemental Route) as well as from carbonyl Fe and MoB powders (MoB route). The powder mixtures compositions were adjusted in such a manner that the cermets prepared from the elemental and MoB routes contained identical vol.% of binder phase along with the complex Mo₂FeB₂ boride phase. The binder content in these cermets varied from 0 to 38.6 vol. %.

Mo₂(Fe_{0.5}Ni_{0.5})B₂ - γ (FeNi) and Mo₂NiB₂-Ni cermets were prepared only through the MoB route. The binder content in these cermets varied from 0 to 37.22 vol. %. Chemical compositions of various constituents used for P/M processing of Mo₂Fe(Ni)B₂-Fe(Ni) cermets are given in Table 2.1 and 2.2. The schematic flow diagram of P/M processing carried out in the present study is shown in the Fig. 2.1.

ELEMENTAL ROUTE

MoB ROUTE

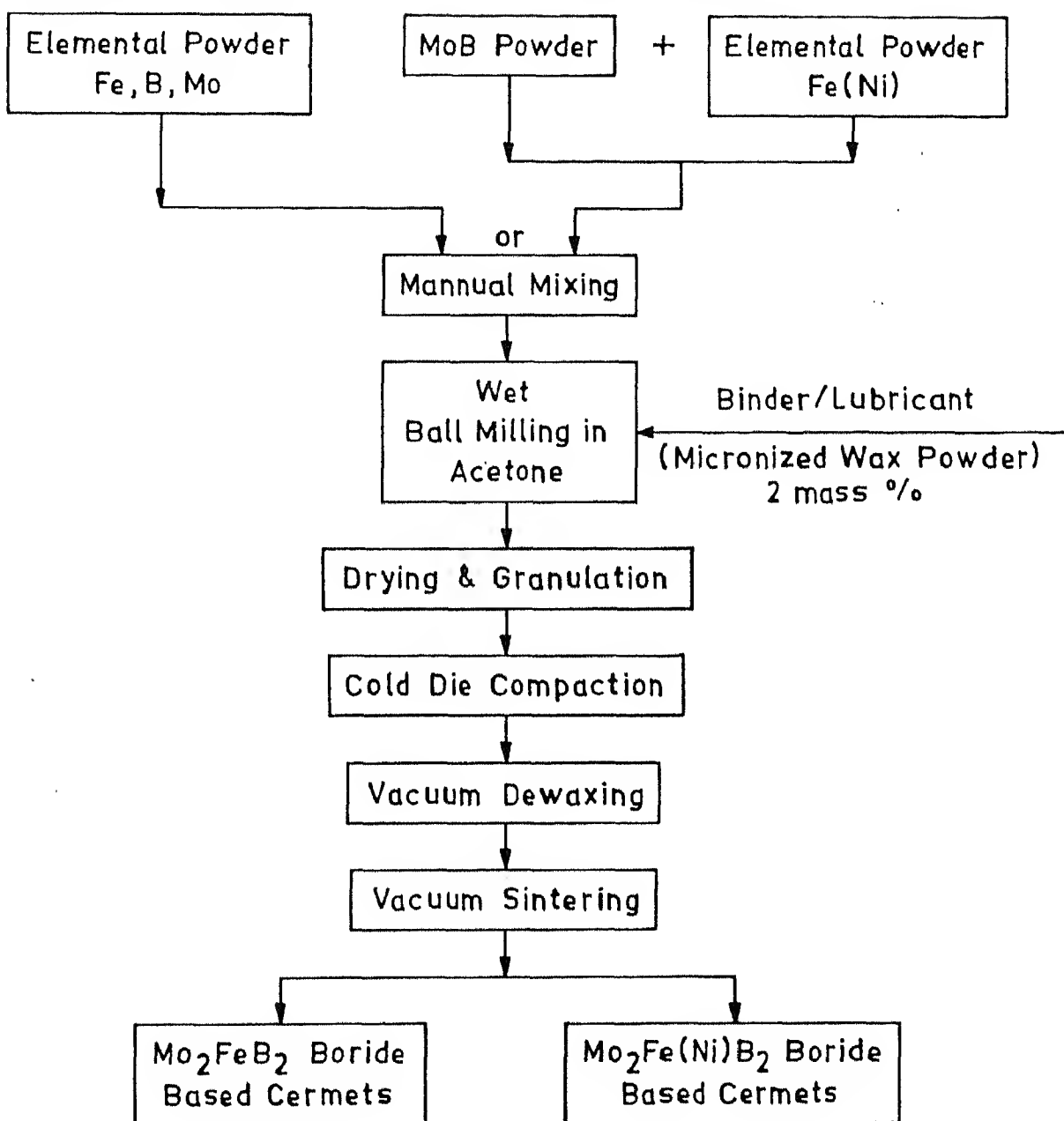


Fig. 2.1. Schematic Flow Diagram of the P/M Processing of Mo₂Fe(Ni)B₂-Fe(Ni) Cermets.

Table 2.1 : Compositions of various constituents in mass% used for the P/M processing of Mo_2FeB_2 - αFe cermet through the elemental route.

Mo_2FeB_2 - αFe Cermets			
Binder Content αFe (vol.%)	Mass %		
	Fe	B	Mo
0	20.72	8.02	71.26
12.43	30.00	7.09	62.91
25.62	40.00	6.08	53.92
38.57	50.00	5.06	44.94

Table 2.2 : Compositions of various constituents in mass% used for the P/M processing of $\text{Mo}_2\text{Fe}(\text{Ni})\text{B}_2$ - $\text{Fe}(\text{Ni})$ cermet through the MoB route

Mo_2FeB_2 - αFe Cermets		
Binder Content αFe (vol.%)	Mass %	
	Fe	MoB
0	20.73	79.27
12.43	30	70.00
25.62	40	60.00
38.57	50	50.00

$\text{Mo}_2(\text{Fe}_{0.5}\text{Ni}_{0.5})\text{B}_2$ - $\gamma(\text{FeNi})$ Cermets			
Binder Content $\gamma(\text{FeNi})$ (vol.%)	Mass %		
	Fe	Ni	MoB
0	10.31	10.84	78.85
11.51	15	15	70
24.41	20	20	60
37.22	25	25	50

Mo_2NiB_2 - Ni Cermets		
Binder Content Ni (vol.%)	Mass %	
	Ni	MoB
0	21.57	78.43
10.88	30	70
23.74	40	60

2.3.1 Powder Premix Preparation

Weighed quantity of powders were manually mixed with the help of mortar and pestle for 1/2 hr, followed by wet ball milling in acetone for 38 hours in 'Fritsch Pullverisette 5' centrifugal type ball mill using WC lined bowl containing 19.95mm ϕ WC balls. Prior to 4 hrs. of completion 2 mass% micronized wax powder was added as a binder to improve the green strength. The ratio of feed-to-ball by mass was kept at 1:5. The powder mixture slurries were dried at room temperature in a desiccator containing fused CaCl_2 . The dried powder mixture was later granulated manually.

2.3.2 Room Temperature Compaction

Rectangular parallelepiped shaped green compact of the size 25.1 x 8.2 x 5.9 mm³ were prepared from the granulated powder mixtures in a 50T electric driven Hydraulic press (Fuel Injection, India make) using a pressure range from 330-340 MPa to achieve 70% of the theoretical green density. Tungsten Carbide lined steel die was used for cold compaction. Prior to each powder filling, die and punch walls were cleaned with acetone and lightly lubricated with Zinc Stearate.

2.3.3 Vacuum Dewaxing and Sintering

Vacuum dewaxing and sintering were carried out in a laboratory type SiC-heated horizontal tubular furnace (Rating : 1.5 kVA, 220 V, 10 amps). The furnace tube was made up of recrystallized alumina (I.D = 38 mm, l = 980mm). One end of the recrystallized alumina tube was attached to a rotary pump (Hind High Vacuum Ltd. make) and the other to a vacuum thermocouple gauge sensor. The system was able to attain a

maximum vacuum of 5×10^{-2} m bar. The furnace had a heating zone of approximately 105 mm in the temperature range between 1250°C-1350°C with an accuracy of $\pm 3^\circ\text{C}$. The schematic furnace diagram, with the vacuum system and electrical circuit diagram are shown in the Fig 2.2.

Vacuum dewaxing of the green powder compact was carried out at 380°C for 45 mins in vacuum (pressure 5×10^{-2} m bar). Slow heating rate of approximately 6°C/min was used for the dewaxing stage to avoid any damage of the green specimen.

The dewaxed specimens were subsequently sintered at 1250°C, 1300°C and 1350°C in vacuum (pressure 5×10^{-2} m bar) for 1 hr respectively. An approximate heating rate of 7°C/min was maintained. The sintered specimens were subsequently cooled under vacuum at a rate of 2°C/min.

2.4 DENSIFICATION BEHAVIOUR

The following densification properties were measured for the sintered cermets.

2.4.1 % Volume shrinkage (% ΔV)

% Volume shrinkage of the sintered cermets was measured from the volume of the green compact (V_g) and the volume of the sintered cermets (V_s) according to the formula.

$$\% \Delta V = \left(\frac{V_s - V_g}{V_g} \right) \times 100 \%$$

Volume of the green compacts was measured from physical dimensions.

Volume of the sintered cermets was measured by volume displacement method (Archimedes' Principle) with the help of Mercury Densometer (Tecramics U.K. make), using the following formula:

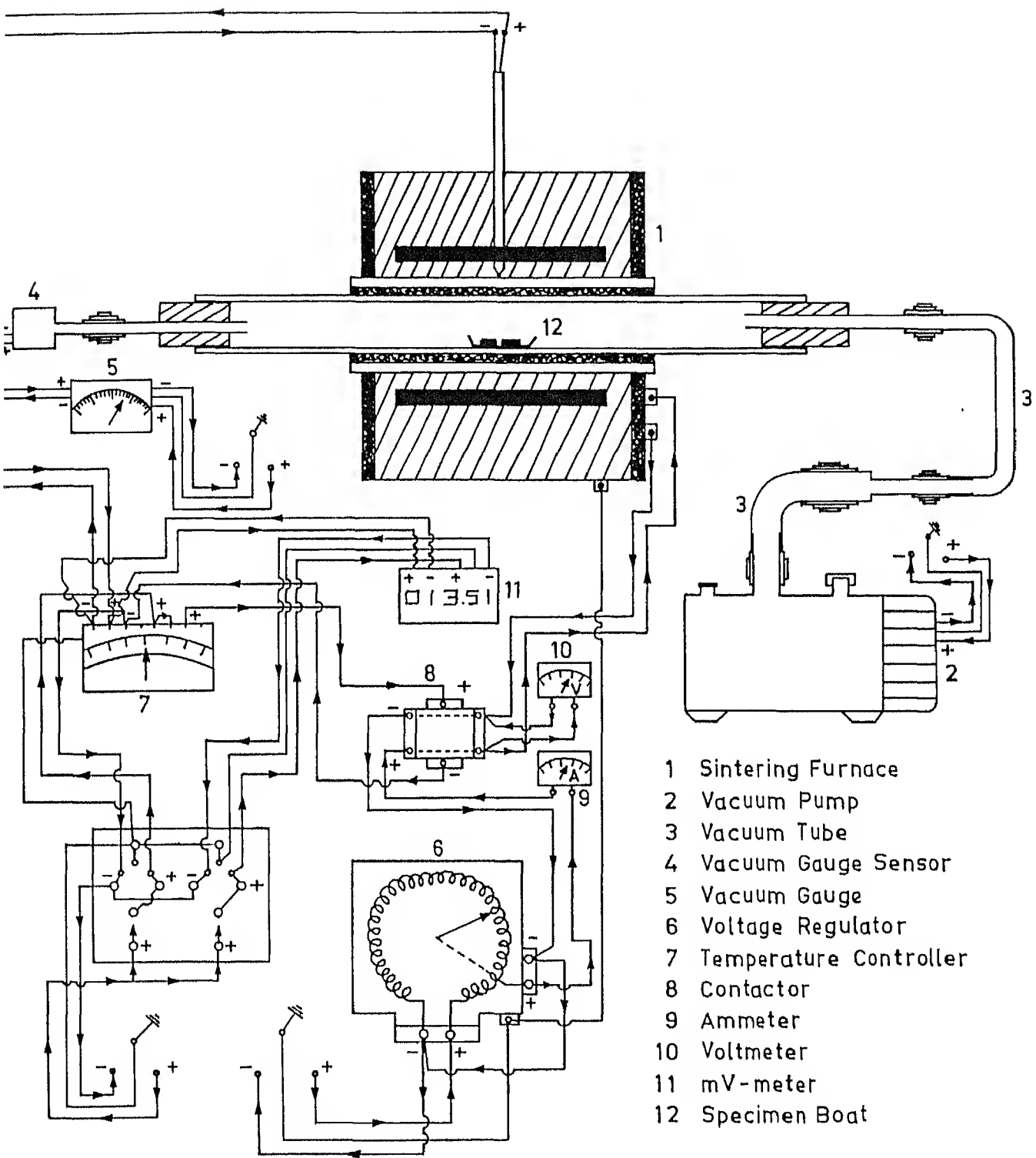


Fig. 2.2. Schematic Diagram of the Vacuum Sintering Furnace Including the Electrical Circuit Diagram .

$$\rho_s = \frac{A - B}{\rho_{Hg}} \text{ cm}^3$$

A = Mass of the sintered cermets in air (g)

B = Mass of the sintered cermets in mercury at the ambient temperature (g)

ρ_{Hg} = Density of mercury at the ambient temperature (Mg/m^3)

Sintered Density (ρ_s)

Sintered density of the cermets was measured by the same method as described in section 2.4.1 according to the following equation:

$$\rho_s = \frac{A \rho_{Hg}}{(A-B)} \text{ Mg/m}^3$$

% Total Sintered Porosity (% ϵ_{TS})

Total sintered porosity of the cermets was evaluated from sintered density and theoretical sintered density according to the following formula :

$$\epsilon_{TS} = \left[1 - \frac{\rho_s}{\rho_{th}} \right] \times 100 \%$$

Theoretical sintered densities of $\text{Mo}_2\text{FeB}_2 - \alpha\text{Fe}$, $(\text{Mo}_{0.5}\text{Ni}_{0.5})\text{B}_2 - \gamma(\text{FeNi})$ and $\text{Mo}_2\text{NiB}_2 - \text{Ni}$ cermets were calculated by the rule of mixture.

Densification Parameter (ΔD)

The densification parameter was calculated using the formula :

$$\Delta D = \frac{\rho_s - \rho_g}{\rho_{th} - \rho_g}$$

ρ_s = Sintered density

ρ_g = Green density

ρ_{th} = Theoretical density

MECHANICAL PROPERTIES

The following mechanical properties of the sintered cermets were evaluated as described below:

Vickers Hardness (HV)

Vickers hardness of the sintered diamond polished specimens

were measured on the HPO 250 Vickers Hardness Testing Machine (Fritz Heckert Leipzig make) with a square base diamond pyramid indenter (included angle $\psi = 136^\circ$) by using 15 kgf or 30 kgf load as per requirements. Vickers hardness was calculated according to the following equation:

$$HV = \frac{1.8544P}{d_{av}^2} \text{ kgf/mm}^2$$

where, P = Indenting load (kgf)

d_{av} = Average value of measurements of two diagonals of the pyramidal indentation (mm)

2.5.2 Transverse Rupture Strength (TRS)

The Transverse Rupture Strength of sintered specimens after final polishing with 2.5 μm size diamond paste was evaluated in the three point bending test using a fixture containing 3 mm ϕ WC rollers having 15 mm length with 15 mm span. Load was applied in the 10T capacity MTS testing machine with a crosshead speed 0.05 mm/min. The maximum load at fracture was used for the calculation of TRS according to the formula:

$$TRS = \frac{1.5 L l}{W t^2} \text{ MPa}$$

where, L = Fracture load (MN)

l = Span length (0.015 m)

W = Width of the test specimen (m)

t = Thickness of the test specimen (m)

For each set of specimen three tests were performed and the average value was reported.

2.5.3 Indentation Fracture Toughness (K_{IC})

Indentation Fracture Toughness of the sintered cermets prepared by MoB route and sintered at 1350°C, was measured based on Palmqvist Crack geometry [19] and using the following

expression:

$$K_{IC} = 0.899709 \left(\frac{HL}{\Sigma l_c} \right)^{1/2} \text{ MPa } \sqrt{\text{m}}$$

where, H = Hardness of the test specimen (MPa)

L = Indenting load (MN)

Σl_c = Total Crack Length (m)

Vickers indentations were made on the diamond polished specimen using a load range between 15 kgf - 30 kgf. Reproducibility of the results required to minimize the subsurface damage produced during specimen preparation. This was achieved by doubling the polishing time with 2.5 μm and 0.25 μm fine grade diamond pastes respectively. For each set of data point average of five indentations were taken into account.

2.6 MICROSTRUCTURAL STUDIES

Microstructural studies carried out with the help of optical metallography and scanning electron metallography are described below:

2.6.1 Optical Metallography

Optical microstructures of the as sintered specimens were prepared by grinding on a carborundum wheel, followed by belt grinding on a 120 grit size SiC endless belt. Prior to fine diamond polishing, coarse diamond polishing was performed with 7 μm size prepolishing diamond paste on a white cast iron wheel. The fine diamond polishing was carried out by polishing with 5 μm , 2.5 μm and 0.25 μm size diamond pastes respectively. Hiffin fluid was used as a lubricant. The polished specimens were chemically etched with the PPP* reagent [1] [10g $\text{K}_4\text{Fe}(\text{CN})_6$, 1g $\text{K}_3\text{Fe}(\text{CN})_6$, 300g KOH and 100 ml H_2O] for 4 to 5 minutes and observed at 1000 X magnification.

2.6.2 Scanning Electron Metallography

$\text{Mo}_2\text{Fe}(\text{Ni})\text{B}_2$ -Fe(Ni) cermet sintered at 1350°C were used for fractography study. This was carried out in case of TRS fractured specimens in JEOL-JSM-840A SEM at 10-15 kV operating voltage by using probe current ranged from 1×10^{-10} A to 5×10^{-8} A with WD ranged from 15 mm to 23 mm in the secondary electron imaging mode.

2.6.3 Boride Grain Mean Linear Intercept (\bar{I}_α) and Binder Mean Free Path (\bar{I}_β)

Boride grain mean linear intercept and binder mean free path were measured in $\text{Mo}_2\text{Fe}(\text{Ni})\text{B}_2$ -Fe(Ni) cermet. \bar{I}_α and \bar{I}_β were calculated in accordance with the following formulae as described by Gurland [20].

$$\bar{I}_\alpha = \frac{2}{m} \sum_{i=1}^m \left[\frac{V_{V\alpha}}{\left\{ 2 N_{L_{\alpha\alpha}}(i) + N_{L_{\alpha\beta}}(i) \right\}} * \frac{1}{M} \right] \mu\text{m}$$
$$\bar{I}_\beta = \frac{2}{m} \sum_{i=1}^m \left[\frac{V_{V\beta}}{N_{L_{\alpha\beta}}(i)} * \frac{1}{M} \right] \mu\text{m}$$

where, $V_{V\alpha}$ = Volume fraction of the hard phase

$V_{V\beta}$ = Volume fraction of the binder phase

$N_{L_{\alpha\alpha}}(i)$ = Contacts per unit test line length $L_{(i)}$ (μm)⁻¹

m = Number of test lines

M = Magnification

The average value of measurements in approximately 19-22 test lines containing boride and binder intercepting grains was reported for each data point.

2.6.4 Boride Phase Contiguity

$\text{Mo}_2\text{Fe}(\text{Ni})\text{B}_2$ boride phase contiguity ($C_{\alpha\alpha}$) of the investigated cermet was measured by counting the number of

boride - boride grain contacts and boride-binder grain contacts according to the formula as described by Gurland [20].

$$C_{\alpha\alpha} = \frac{1}{m} \sum_{i=1}^m \left[\frac{2N_{\alpha\alpha}(i)}{\left\{ 2 N_{\alpha\alpha}(i) + N_{\alpha\beta}(i) \right\}} \right]$$

where, $N_{\alpha\alpha}(i)$ = Number of $\text{Mo}_2\text{Fe}(\text{Ni})\text{B}_2$ - $\text{Mo}_2\text{Fe}(\text{Ni})\text{B}_2$ boride-boride grain contacts containing the i-th test line

$N_{\alpha\beta}(i)$ = Number of $\text{Mo}_2\text{Fe}(\text{Ni})\text{B}_2$ -Fe(Ni) boride-binder grain contacts containing the i-th test line

m = Number of test lines

The average value of measurements carried out over 19-22 test lines on each optical micrograph was reported for each data point.

2.7 X-RAY DIFFRACTION ANALYSIS

X-ray diffraction study of sintered cermets after diamond polishing was carried out with the help of Rich Seifert make (Germany) X-ray Diffractometer using $\text{Cr}_{K\alpha}$ and $\text{Cu}_{K\alpha}$ radiations respectively. The polishing details are described in subsection 2.6.1. Phase identification was carried out from the X-ray diffraction analysis. The various parameters used in the experiment are given below :

Target (Radiation)	Amperage mA	Voltage kV	Counts per Minutes	Time Constant sec	Scanning Rate ($^\circ/\text{min}$ in 2θ)	Chart speed mm/min
$\text{Cr}_{(K\alpha)}$	32	42	5	10	3 1.2	30 12
$\text{Cu}_{(K\alpha)}$	22	32	10	10	3 1.2	30 12

Interplanar spacings ($d_{h_i k_i l_i}$) of various hard and binder phases in $\text{Mo}_2\text{Fe}(\text{Ni})\text{B}_2$ - Fe(Ni) cermets were calculated from the X-ray

diffraction pattern using Bragg's law of diffraction.

$$d_{h_i k_i l_i} = \frac{\lambda}{2 \sin \theta_{h_i k_i l_i}} \text{ (Å)}^{\circ}$$

where, λ = Wave Length of X-ray radiation used ($\lambda_{\text{CrK}_\alpha} = 2.2909 \text{ Å}$;

$$\lambda_{\text{CuK}_\alpha} = 1.541838 \text{ Å}^{\circ}$$

$\theta_{h_i k_i l_i}$ = Bragg angle of the $\{h_i k_i l_i\}$ diffracting planes ($^{\circ}$)

Indexing of the X-ray diffraction patterns were carried out by direct matching method with the help of Powder Data File. Lattice parameters of various identified hard and binder phases in $\text{Mo}_2\text{Fe}(\text{Ni})\text{B}_2$ - $\text{Fe}(\text{Ni})$ cermets were calculated from the derived formulae based on least square approximation.

2.8 SATURATION MAGNETIC FLUX DENSITY

Saturation magnetic flux density was measured for $\text{Mo}_2\text{Fe}(\text{Ni})\text{B}_2$ - $\text{Fe}(\text{Ni})$ cermets prepared through the MoB route and sintered at 1350°C , so as to get an idea about the nature and distribution of the hard and binder phases. A Dr. Foerster make unit was used for the above measurements.

2.9 THERMAL SHOCK RESISTANCE

One portion of the TRS fractured specimen was ground and diamond polished as described in the section 2.6.1. Thermal shock resistance was measured on all the sintered cermets prepared by MoB route at 1350°C . The specimens were heated to 800°C in argon at an interval of 100°C , held for 10 minutes and finally oil quenched at room temperature. The as quenched specimens were observed under 100x magnification in optical microscope. The emergence of crack formation gave a qualitative index of the thermal shock resistance. The specimen heating was carried out in a vertical cylindrical type twin halve nichrome

resistance furnace. The schematic detail including electrical circuit diagram is shown in the Fig. 2.3. After reaching the elevated temperature the shutter was opened and the specimens were oil quenched at the ambient temperature so as to impart a thermal shock.

2.10 CORROSION WEIGHT LOSS STUDY

Corrosion weight loss study was carried out in case of $\text{Mo}_2\text{Fe}(\text{Ni})\text{B}_2$ -Fe(Ni) cermets prepared through the MoB route after 1350°C sintering. Approximately $12 \times 6 \times 4 \text{ mm}^3$ size specimens were prepared by machining with the help of low speed saw containing 0.3 mm thick diamond blade (Buehler Ltd., USA make) followed by diamond polishing with 7 μm size diamond paste respectively. The diamond polished specimens were dipped in 250 ml 10 wt% HCl (Sp. gr. 1.18, 35%) and 10 wt% HF (Sp. gr. 1.13, 40%) solutions respectively for 10 hours at the ambient temperature. The corrosion rate (C) was measured from the corrosion mass loss according to the formula as described in ASTM G31.

$$C = 3.449 \times 10^5 \frac{\Delta m}{\rho A T} \text{ mpy}$$

where, Δm = Corrosion mass loss (mg)

ρ = Density of the sintered specimen (Mg/m^3)

A = Surface area of the specimen exposed to the corrosive media (mm^2)

T = Exposure time (hours)

mpy = Mils per year

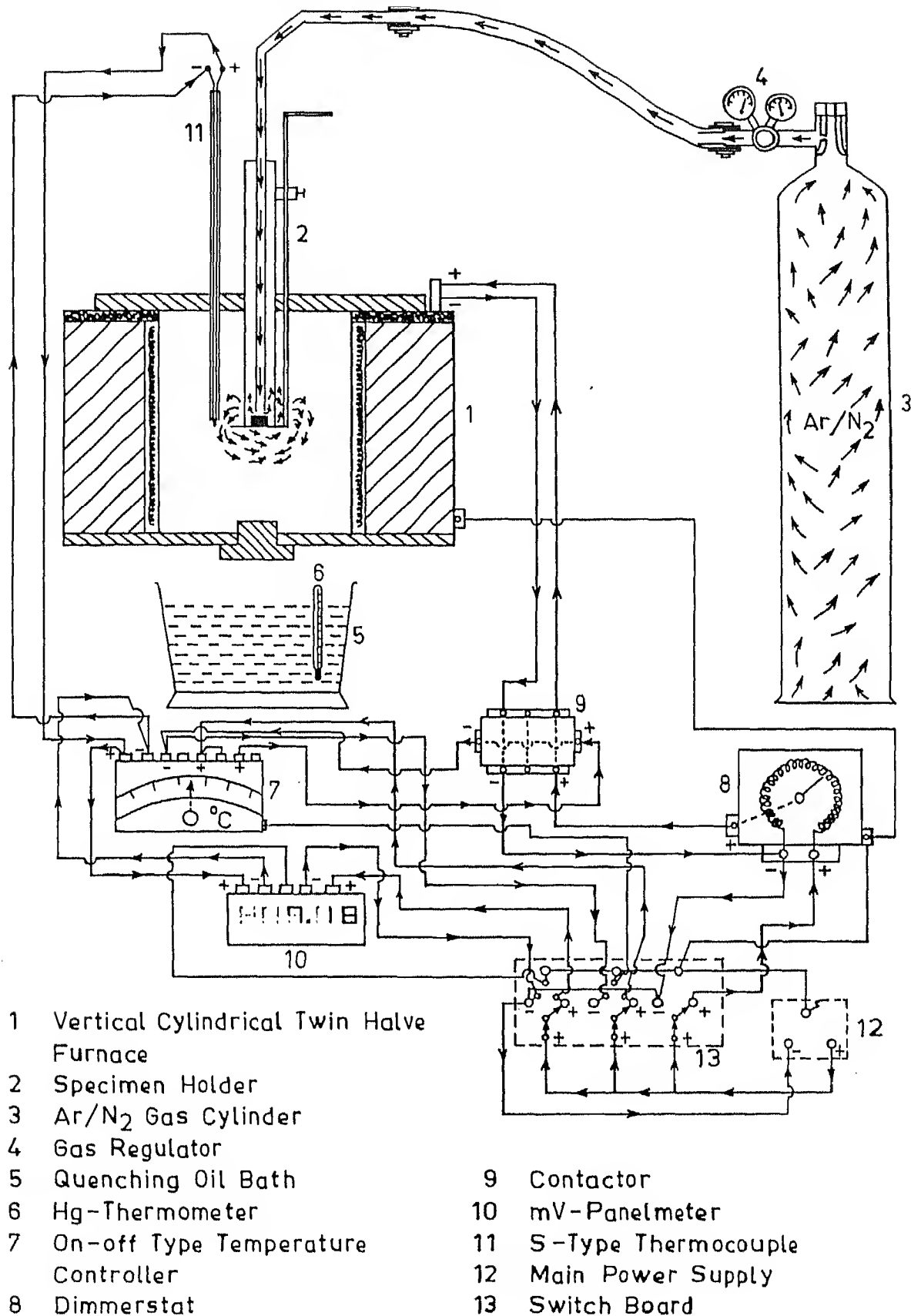


Fig. 2.3. Schematic Diagram of the Thermal Shock Measuring Furnace including Oil-Bath and Electrical Circuit Diagram .

CHAPTER III

EXPERIMENTAL RESULTS

PART I : SINTERING OF Mo_2FeB_2 - αFe CERMETS THROUGH ELEMENTAL AND MoB ROUTES

3.1 CHARACTERIZATION OF MILLED POWDERS

Fig. 3.1 - 3.3 reveal the particle size distribution of as received and various ball milled powder premixes prepared from the elemental and MoB routes. Tables 3.1 and 3.2 give the data of the average particle size of as received and milled powders corresponding to different cermet compositions. From the Tables it is evident that with increase in binder content, the average value in general increases. It is noteworthy that the particle size of charge from the elemental milling is lower than that obtained from the MoB route.

Fig. 3.4(a) - (e) show the secondary electron images of as received carbonyl iron, boron, molybdenum, molybdenum boride (MoB) and nickel powders respectively. Carbonyl iron powder consists of spherical particles, boron powder shows irregular geometrical shaped plate type particles, molybdenum powder reflects regular polygonal plate type particles and molybdenum boride (MoB) powder exhibits regular dumbbell shaped particles. Nickel powder is characterized by rosette type particles. The characteristic feature is that no micropores are present in the powder particles. In case of carbonyl iron and boron powder satellite formation is quite predominant.

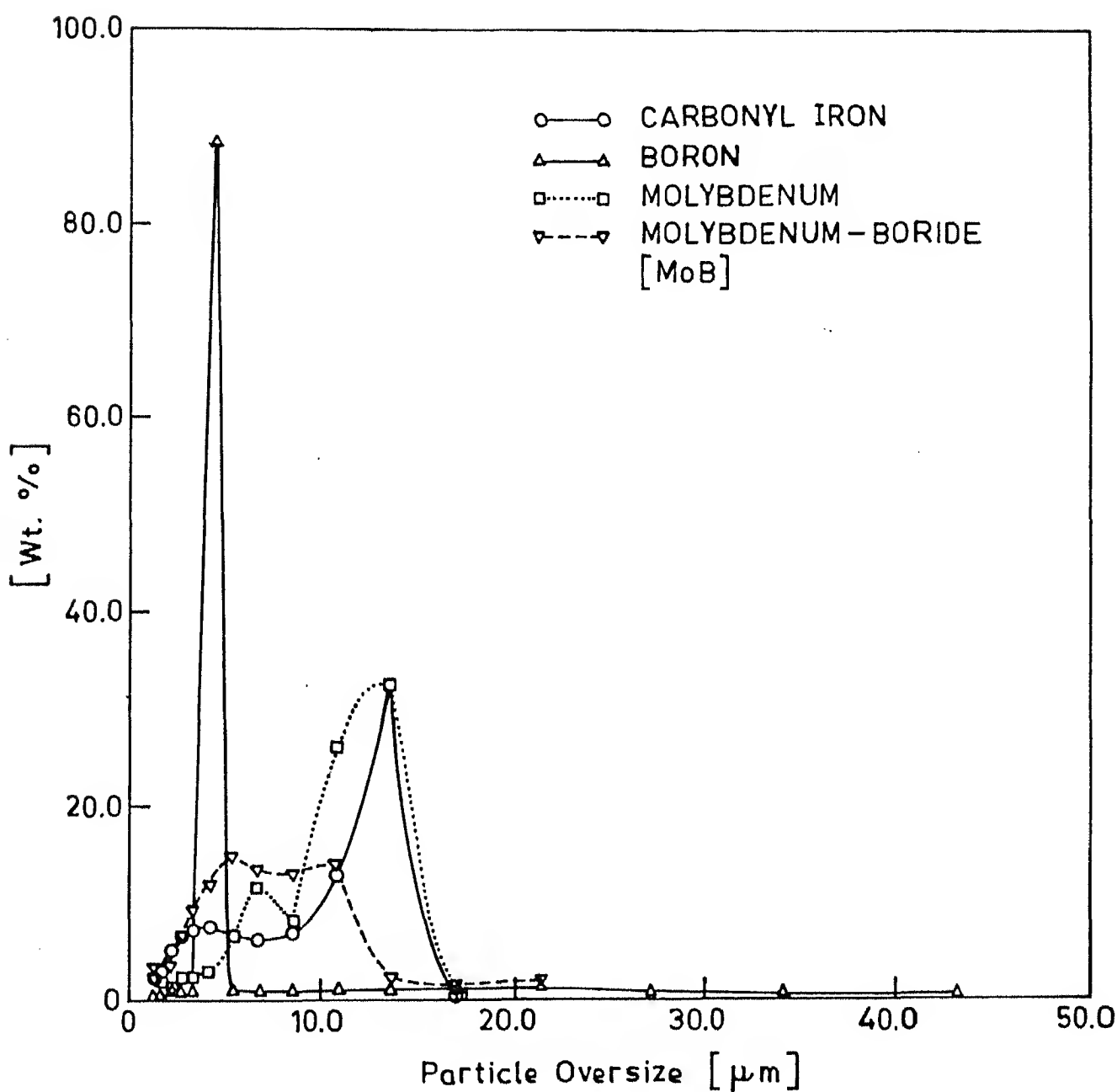


Fig. 3.1. Particle size distribution of the as received powders.

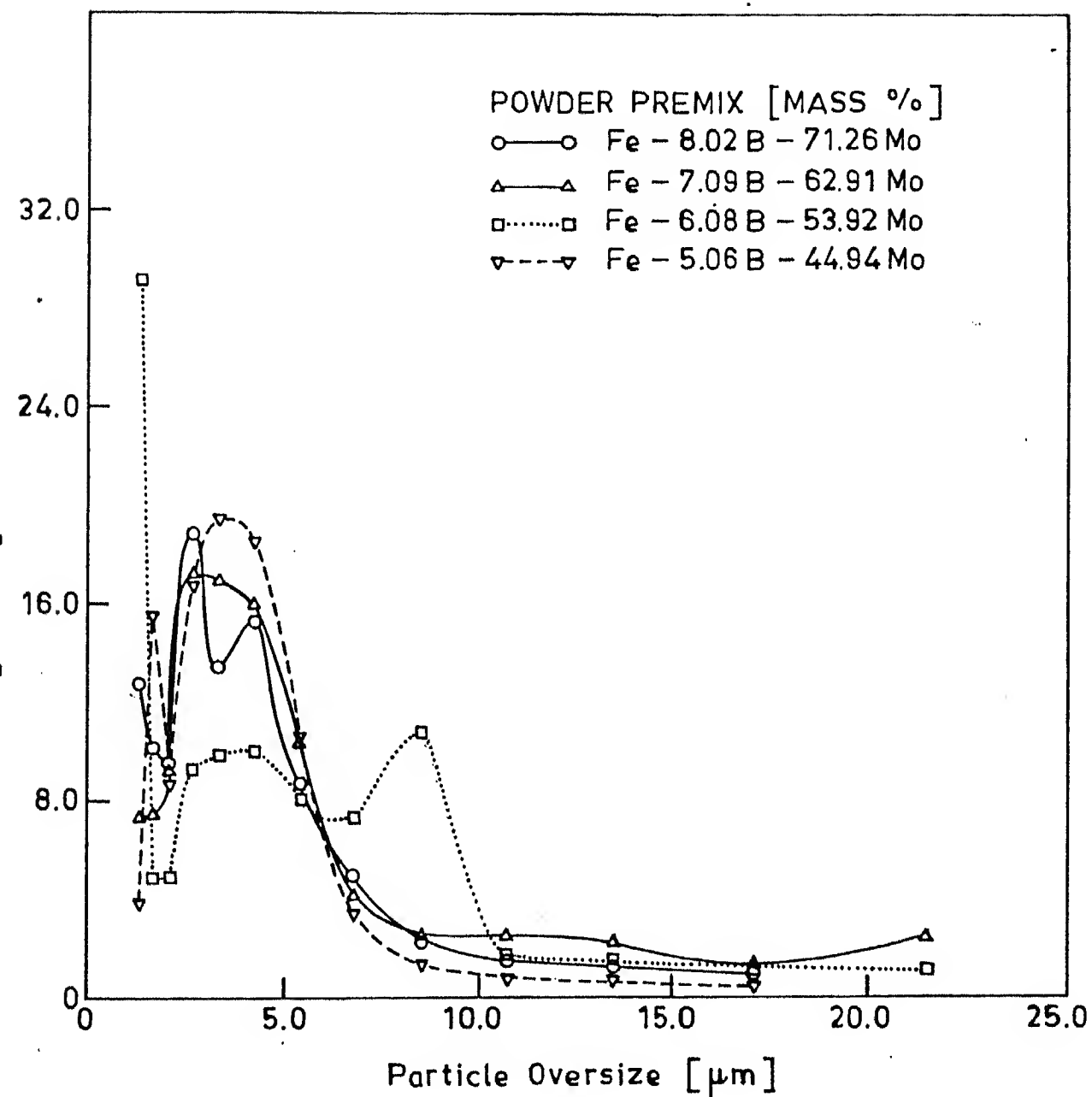


Fig. 3.2. Particle size distribution of the Mo-B-Fe elemental powder premixes.

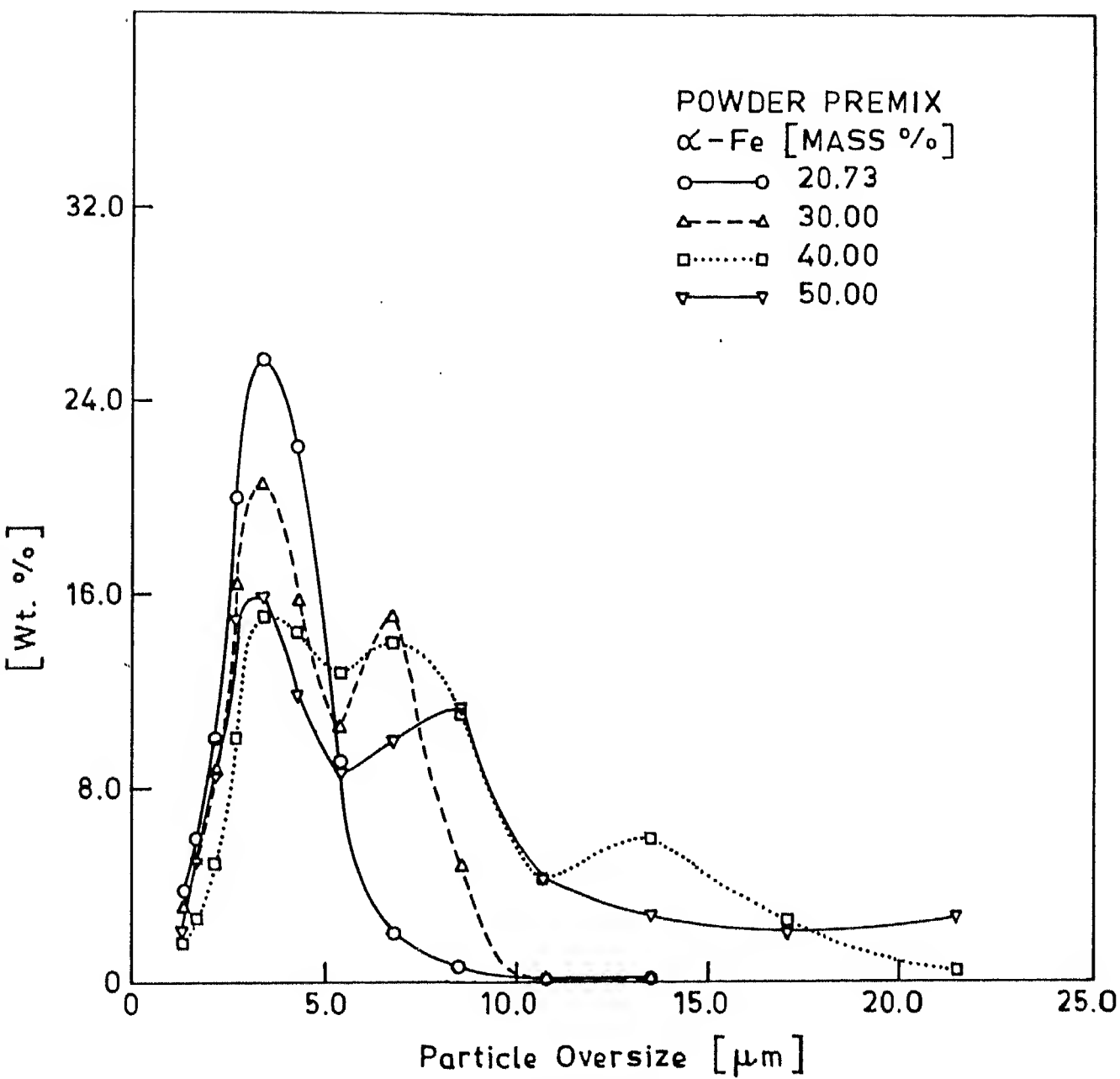
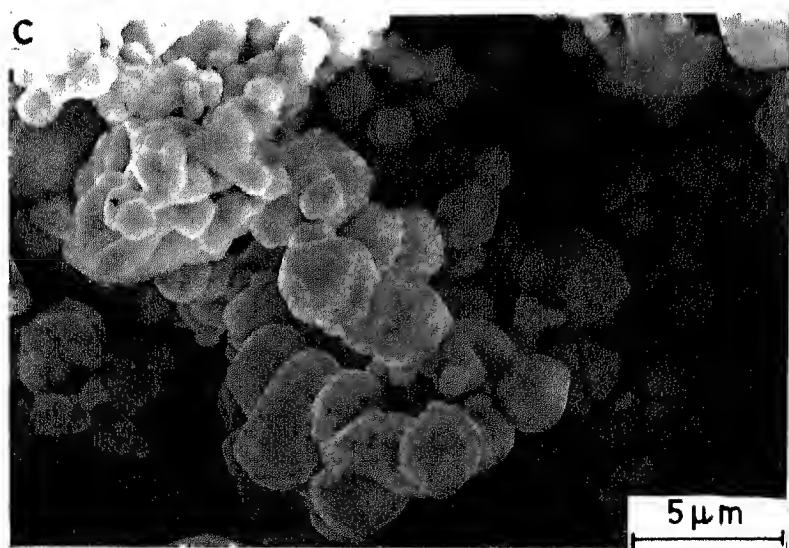
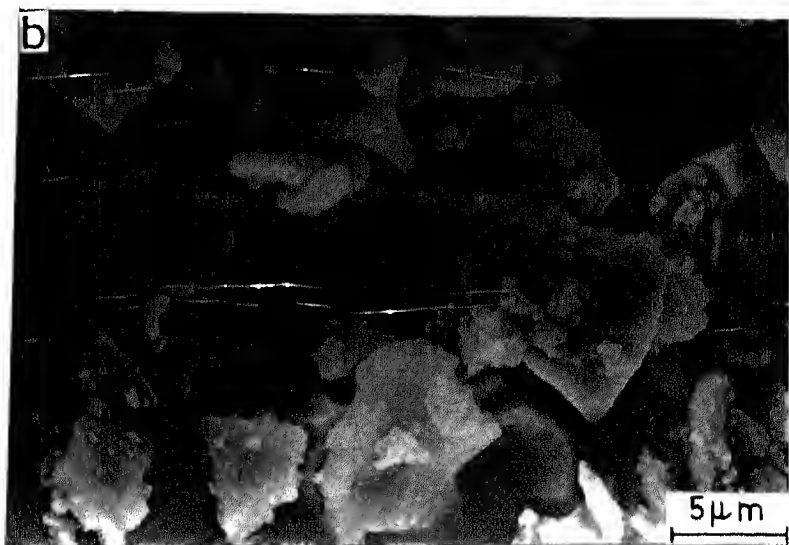
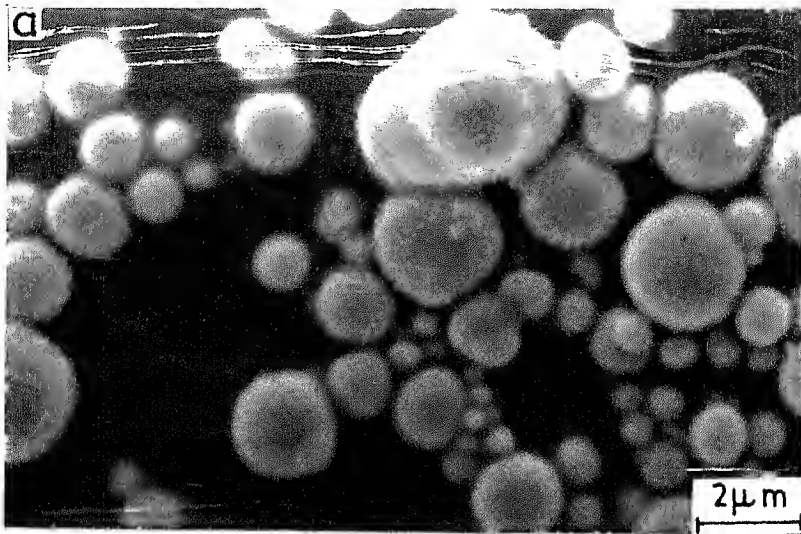


Fig. 3.3. Particle size distribution of the MoB-Fe powder premixes.



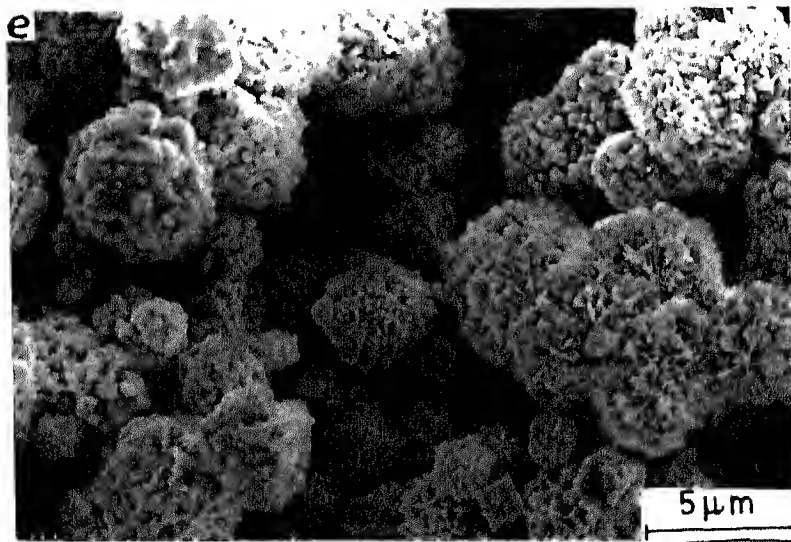
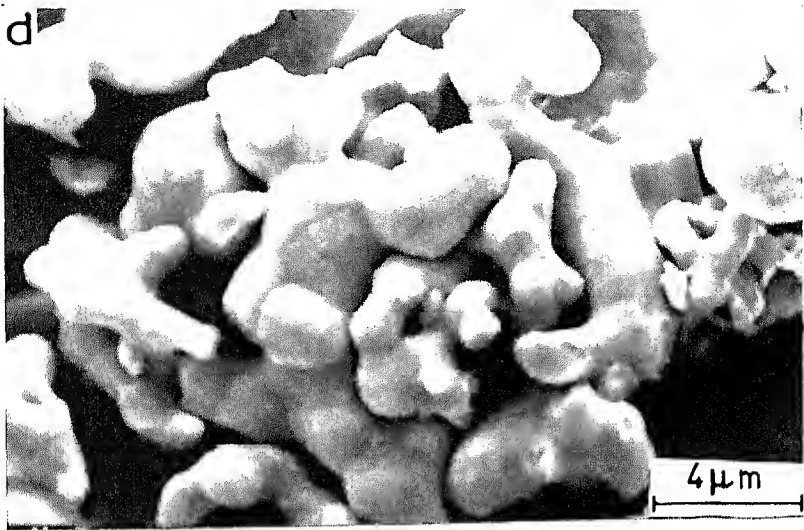


Fig. 3.4 Secondary electron images of various powders:
(a) Carbonyl Fe (b) B (c) Mo (d) MoB (e)
Carbonyl Ni

3.2 DENSIFICATION BEHAVIOUR

Various densification properties i.e. % Volume shrinkage, Sintered density, % Total sintered Porosity and Densification Parameter are described in the following subsections:

3.2.1 % Volume Shrinkage

% Volume shrinkage of Mo_2FeB_2 - αFe cermet in general increases with the increase in αFe binder content and sintering temperature (Fig. 3.5). Elemental powder route exhibits a drastic increase in the % Volume shrinkage in the initial stage. After 12.43 vol.% binder addition, 1250°C sintering reflects a slow increase in % Volume shrinkage, whereas in case of 1300°C and 1350°C sintering % Volume shrinkage does not change quite significantly and are almost in proximity. The straight Mo_2FeB_2 boride phase after 1250°C and 1300°C sintering exhibits swelling followed by a drastic increase in % Volume shrinkage after 1350°C sintering. In case of MoB route the straight Mo_2FeB_2 boride phase does not show any swelling. The increase in αFe binder content shows an identical pattern in % Volume shrinkage variation with the exception in case of 12.43 vol. % αFe binder at 1300°C, where it shows a maximum. At sintering temperature of 1250°C the % Volume shrinkage variation follows almost a linear relationship with the binder content. The 1350°C sintering does not reflect much change in % Volume shrinkage variation in case of 12.43 vol.% binder addition.

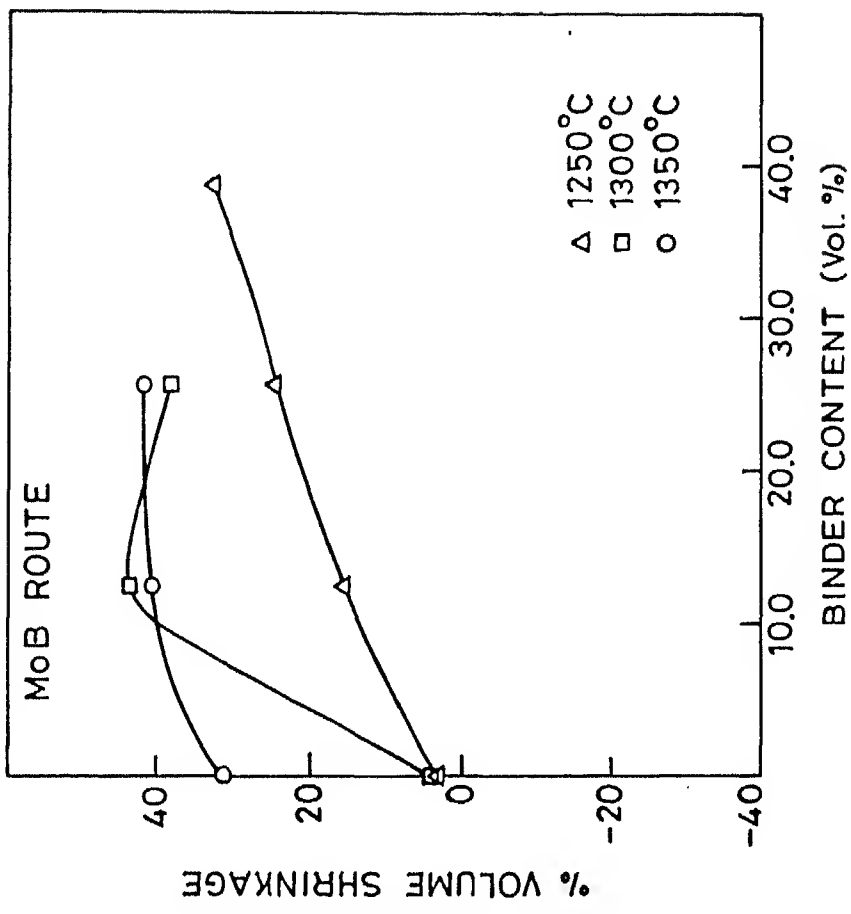
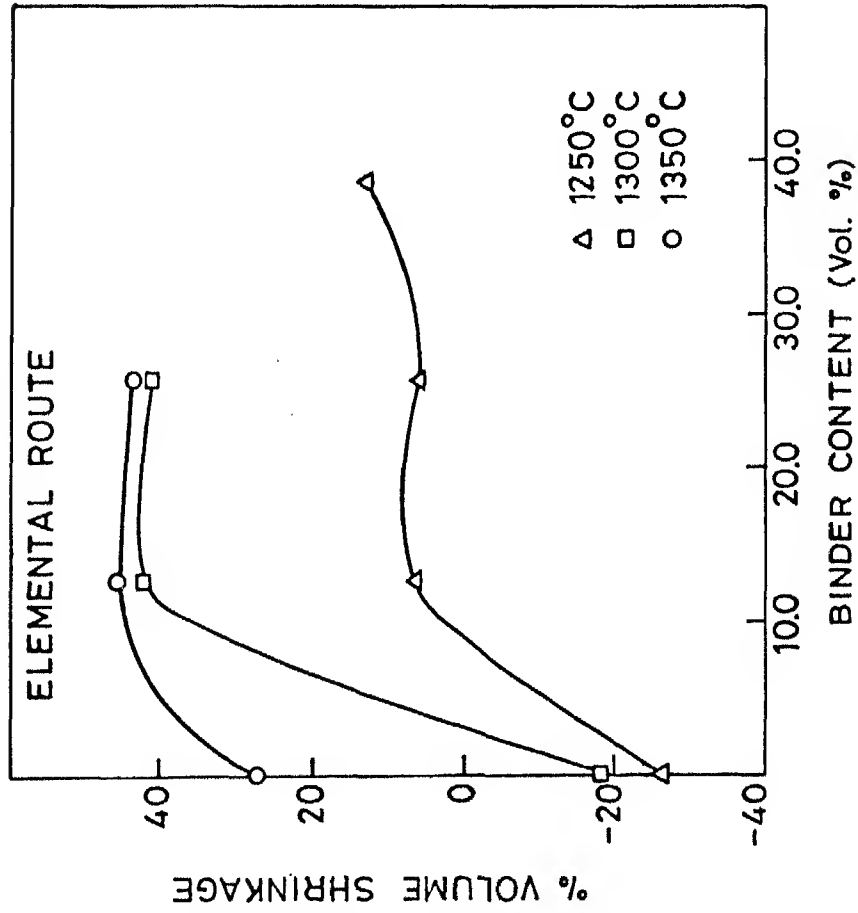


Fig. 3.5. % Volume shrinkage variation of $\text{Mo}_2\text{FeB}_2\text{-}\alpha\text{Fe}$ cermet prepared through the elemental and MoB routes and sintered at different temperatures.

Table 3.1 : Average particle size of as received powders

Powder	Average Particle Size (μm)
Mo	2.11
Carbonyl Fe	2.17
Ni	1.59
B	3.72
MoB	2.16

Table 3.2 : Average particle size of ball milled powders corresponding to different Mo_2FeB_2 - α Fe Cermets prepared through elemental and MoB routes

Binder Content (vol.%)	Average Particle Size, μm	
	Elemental Route	MoB Route
0	1.79	2.21
12.43	1.95	2.25
25.62	1.53	2.47
38.57	2.03	2.27

3.2.2 Sintered Density

Sintered density of the cermets increases with the increase in the binder content (Fig. 3.6). In the initial stage the increase is rapid but after 12.43 volume% binder addition the variation is insignificant. In case of cermets prepared through MoB route the nature of plots is similar, but in magnitude the sintered density values are higher than those for cermets prepared from the elemental route. Cermets prepared from either route follow almost an identical pattern in density variation at any sintering temperature. In case of straight Mo_2FeB_2 , on

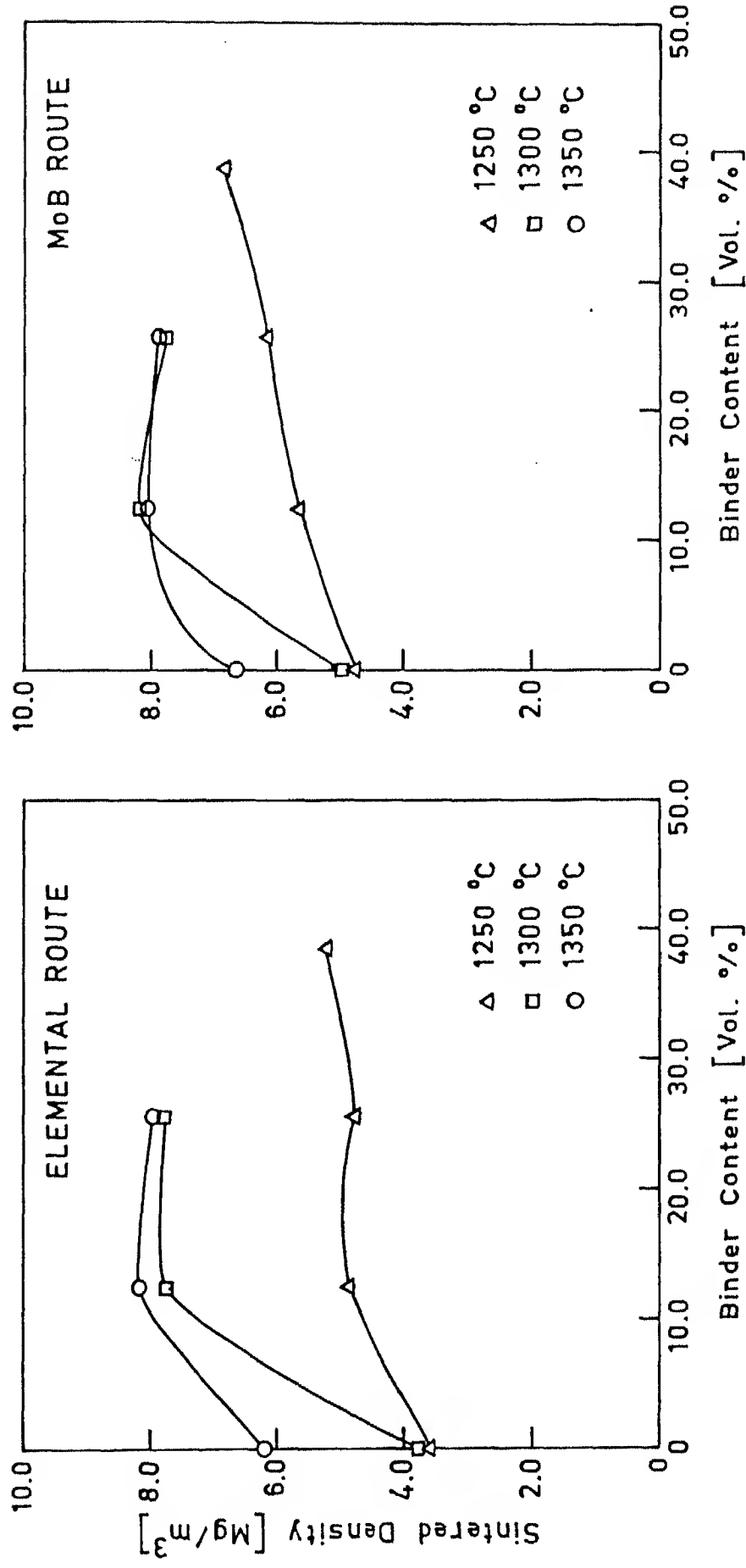


Fig. 3.6. Sintered density variation of Mo_2FeB_2 - αFe cermet prepared through elemental and MoB routes and sintered at different temperatures.

increasing the sintering temperature from 1250°C to 1300°C sintered density remains almost constant and then increases rapidly with the further increase in sintering temperature. But in case of cermets containing higher volume% binder the sintered density increases rapidly from 1250°C to 1300°C sintering. The value remains almost constant with the further increase in sintering temperature. The processing route adopted for cermets does not reflect much change on density in case of higher volume% binder.

3.2.3 % Total Sintered Porosity

Cermets prepared from both the routes follow an identical trend in the variation of % total sintered porosity with the binder content (Fig. 3.7). Cermets prepared from the MoB route possessed lower % total sintered porosity as compared to those from the elemental route. Initially for either route the property reduces rapidly for 12 vol.% binder cermets. However, the variation in the % total sintered porosity is not quite significant with the further increase in the binder content, particularly during sintering at 1300°C and 1350°C. The value reduces drastically with the increase in sintering temperature from 1250°C to 1300°C. In case of straight Mo_2FeB_2 , the % total sintered porosity remains almost constant upto 1300°C, but in case of 1350°C sintering it reduces rapidly.

3.2.4 Densification Parameter

Cermets prepared by either route exhibit a drastic increase in the densification parameter for ~ 12 vol.% binder (Fig. 3.8). In case of cermets prepared from the Elemental route with greater

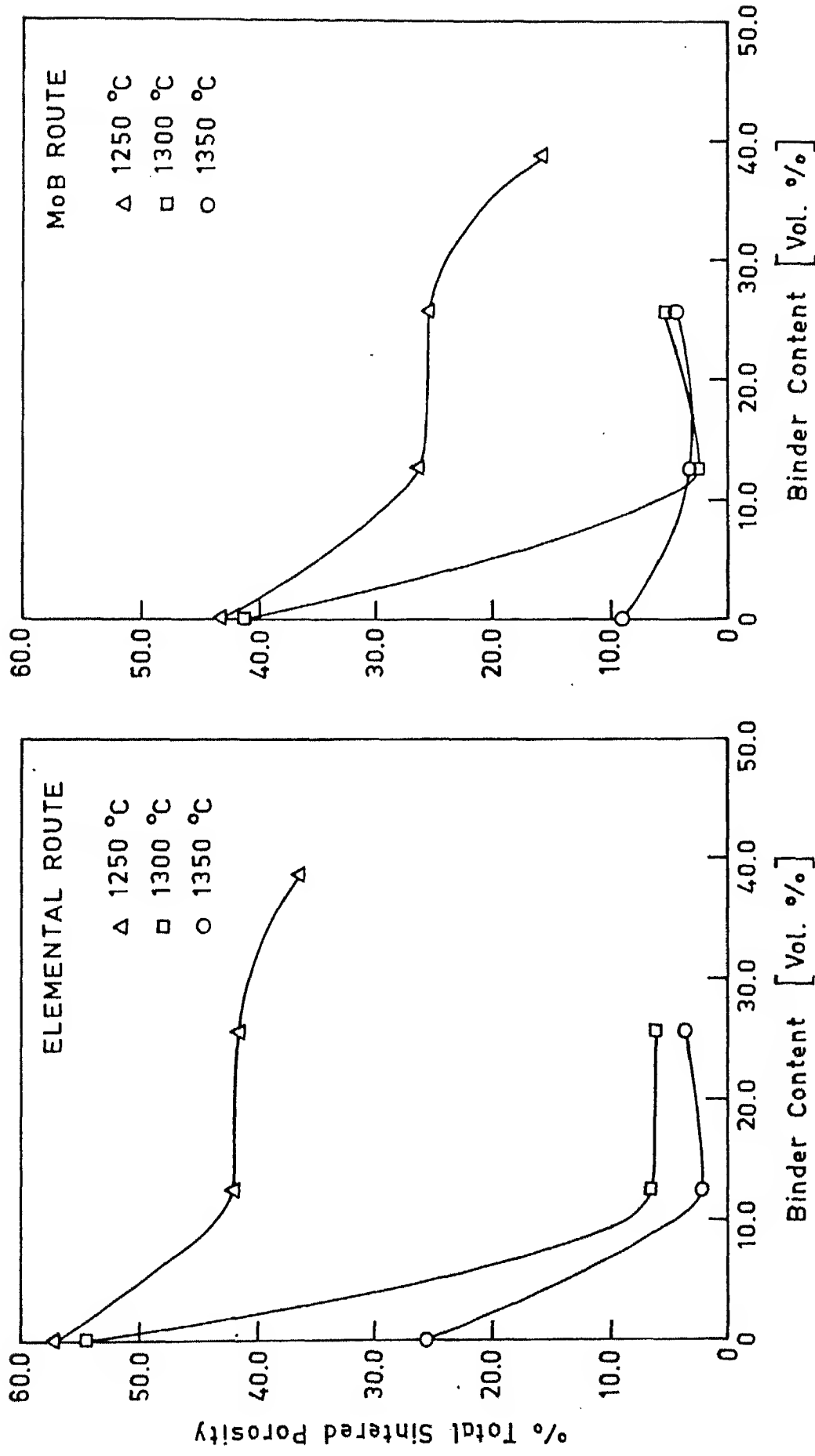


Fig. 3.7. % Total sintered porosity variation of Mo_2FeB_2 - αFe cermet prepared through elemental and MoB routes and sintered at different temperatures.

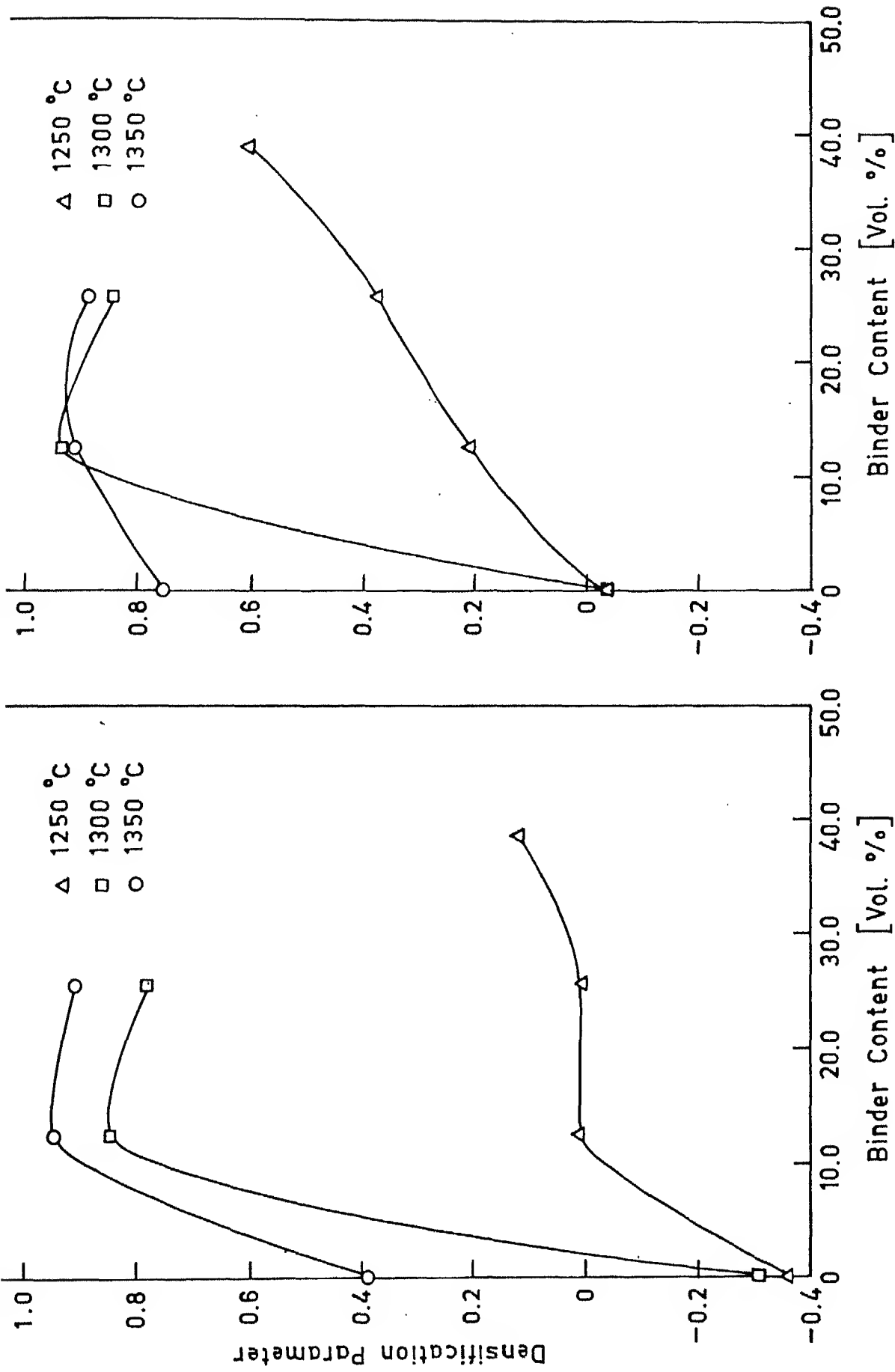


Fig. 3.8. Densification parameter variation of $\text{Mo}_2\text{FeB}_2\text{-}\alpha\text{Fe}$ cermet prepared through elemental and MoB routes and sintered at different temperatures.

than this binder addition, the variation in the densification parameter is not quite significant at 1300°C and 1350°C, but at 1250°C sintering with ~ 25 vol. % binder the densification parameter increases slowly. In case of 1250°C sintering, cermet prepared from the MoB route follow a rapid increase in the densification parameter with the increase in the binder content. However, in case of 1300°C and 1350°C sintering, it decreases for greater than 12.43 vol.% binder addition.

It is interesting to note that with the increase in temperature, its effect on densification behaviour is similar for cermets, but in case of straight boride Mo_2FeB_2 , the densification parameters in case of 1250°C and 1300°C sintering are in proximity.

3.3 MECHANICAL PROPERTIES

Various mechanical properties i.e. Vickers Hardness, Transverse Rupture Strength (TRS) and Indentation Fracture Toughness (Kc) are described in the following subsections.

3.3.1 Vickers Hardness

Cermets prepared from the elemental route exhibit an increase in Vickers hardness with the increase in binder content (Fig. 3.9). The variation is not much significant for 1250°C sintering but at higher temperatures Vickers hardness increases rapidly with the increase in binder content. In case of cermets prepared from the MoB route at 1250°C, the property does not vary uniformly with the increase in binder content. At higher sintering temperatures, there is a maximum in the plots at ~ 12 vol.% binder.

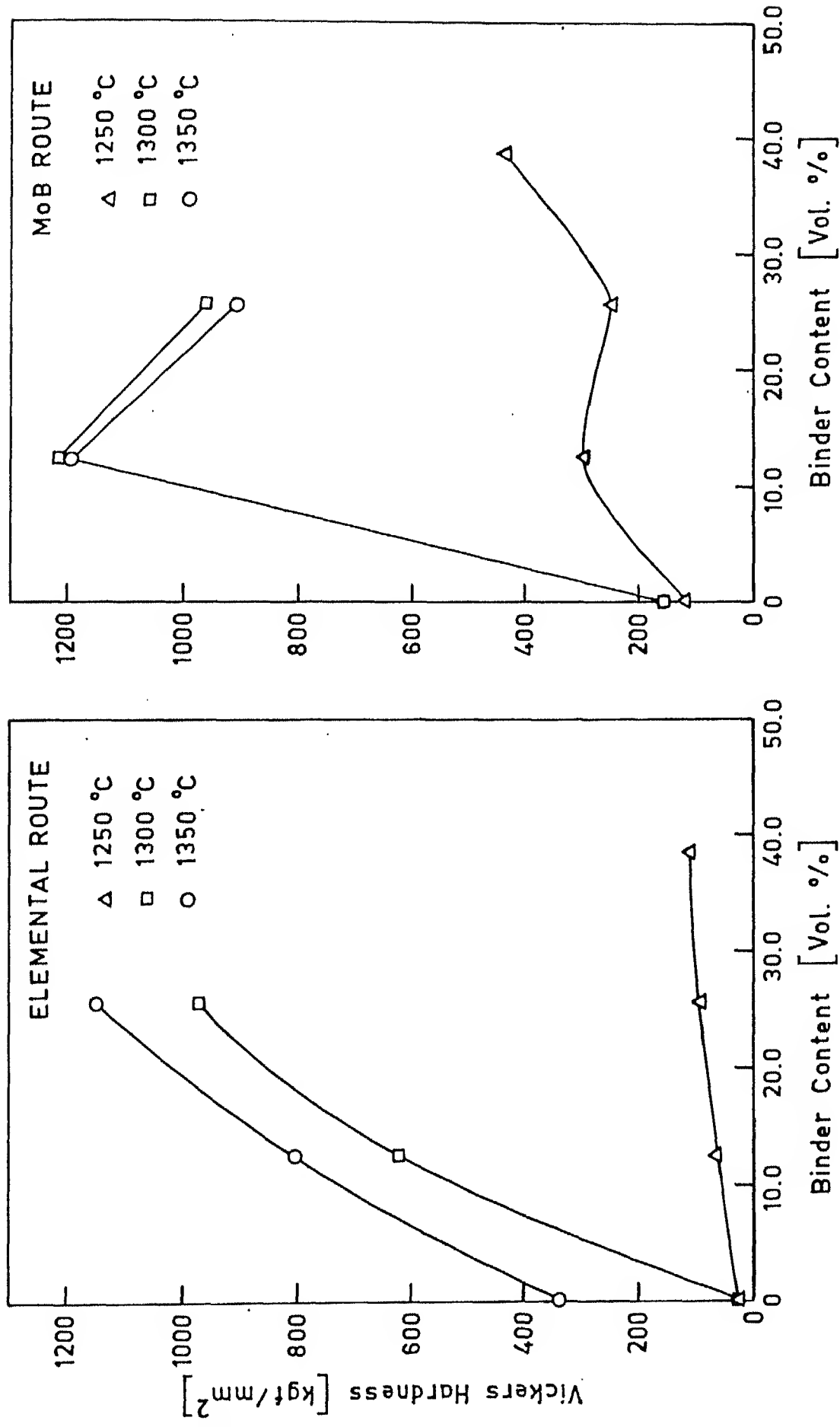


Fig. 3.9. Vickers hardness variation of $\text{Mo}_2\text{FeB}_2 - \alpha\text{Fe}$ cermets prepared through the elemental and MoB routes and sintered at different temperatures.

In case of Mo_2FeB_2 , the Elemental route exhibits higher hardness, particularly when it was sintered at 1350°C , but in case of MoB route, the effect of sintering temperature is absent.

3.3.2 Transverse Rupture Strength (TRS)

The transverse rupture strength increases with the increase in binder content with the exception in case of cermets prepared from the elemental route after sintering at 1350°C (Fig. 3.10), where there is a drop in TRS at ~12 vol.% binder. In case of straight Mo_2FeB_2 boride prepared from the elemental route, the change in TRS up to 1300°C sintering is insignificant, after which it increases rapidly.

A noteworthy feature is that the cermets containing 25.62 vol.% binder prepared from either route exhibit maximum transverse rupture strength.

3.3.3 Indentation Fracture Toughness (K_{IC})

Fig. 3.11 shows the variation in indentation fracture toughness of cermets prepared by the MoB route after sintering at 1350°C . It is evident that values increase with the increase in the binder content. The increase in toughness for 25.62 vol.% binder content is about 116% higher to that of straight Mo_2FeB_2 boride.

3.4 OPTICAL MICROSTRUCTURE AND SEM FRACTOGRAPHY

Fig. 3.12(a) and (b) show the optical microstructures of the straight Mo_2FeB_2 prepared through the elemental and MoB routes after 1350°C sintering. It is evident that the straight Mo_2FeB_2 boride prepared through the elemental route is highly porous, porosity is approximately 25.63%. The microstructures mainly

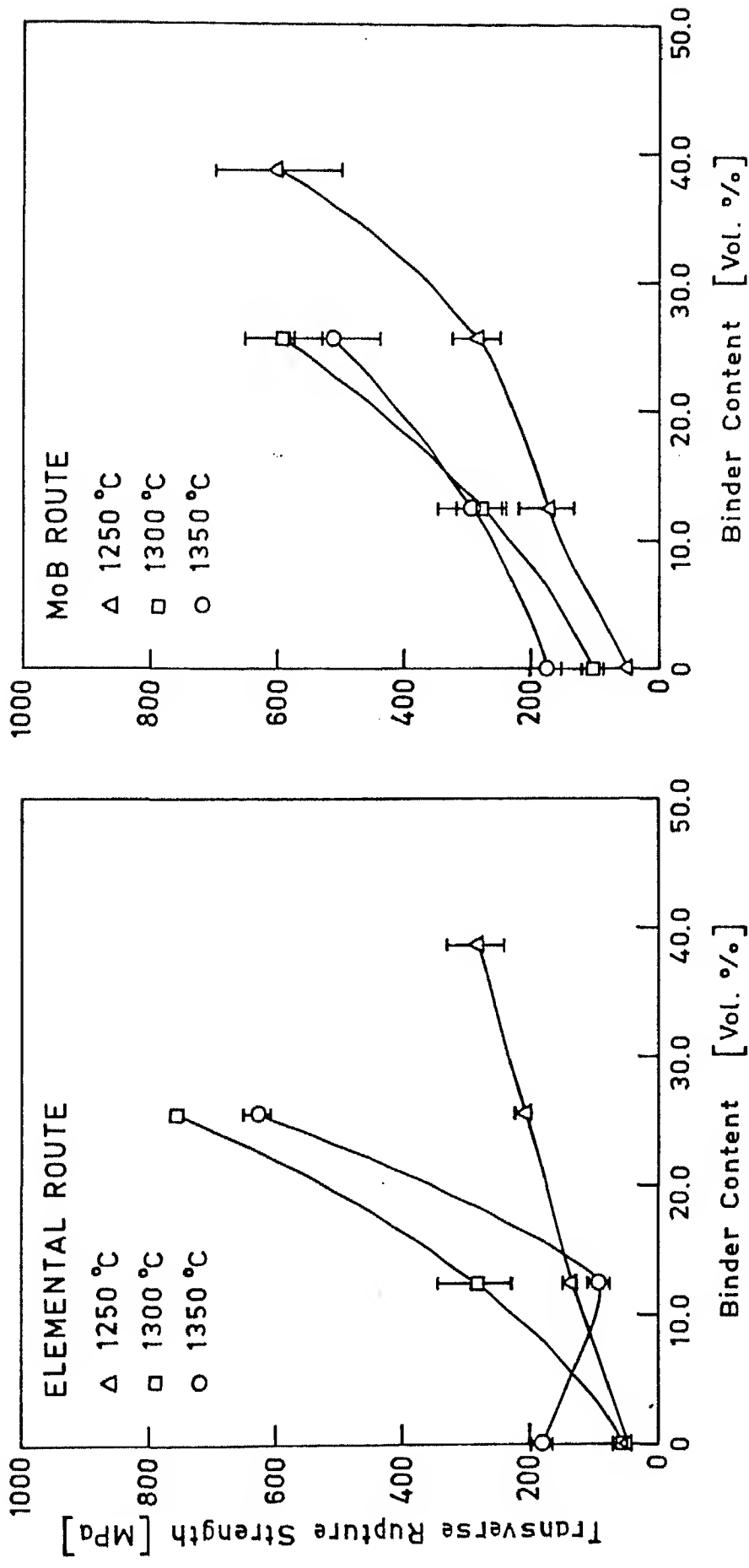


Fig. 3.10. Transverse rupture strength variation of $\text{Mo}_2\text{FeB}_2\text{-}\alpha\text{Fe}$ cermet prepared through elemental and MoB routes and sintered at different temperatures.

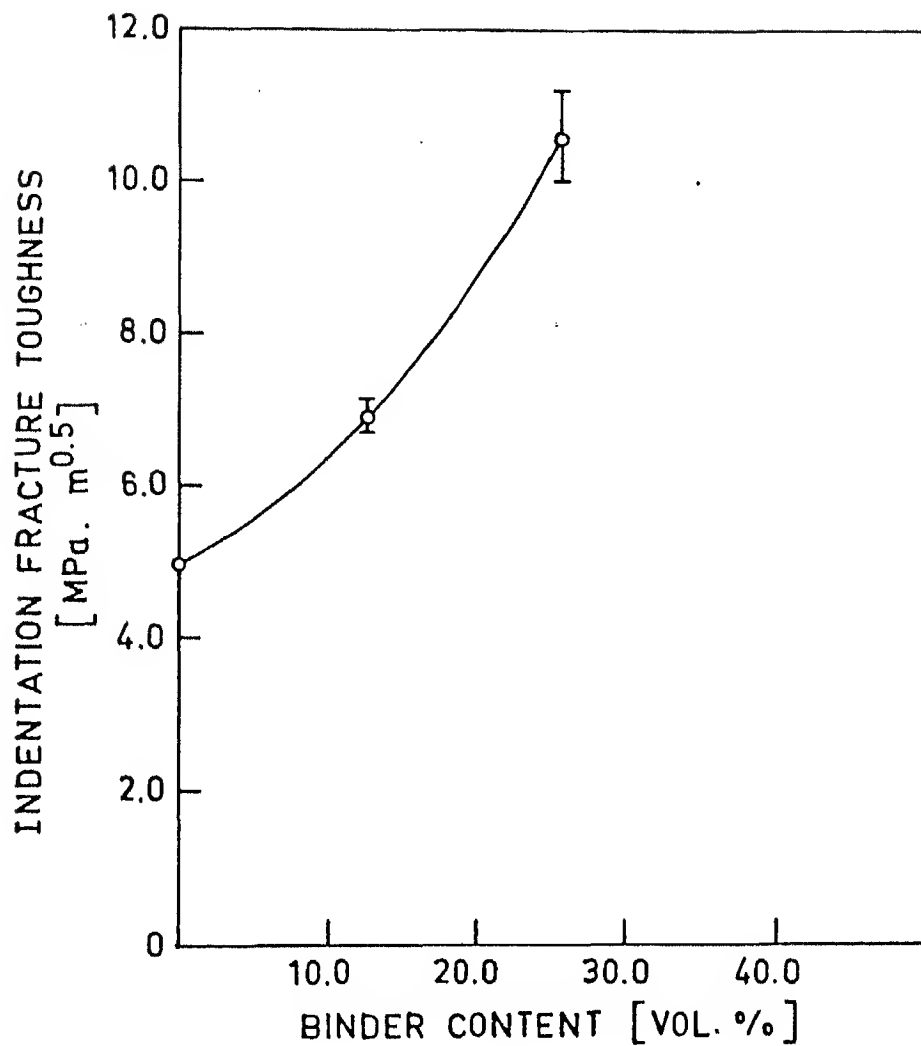
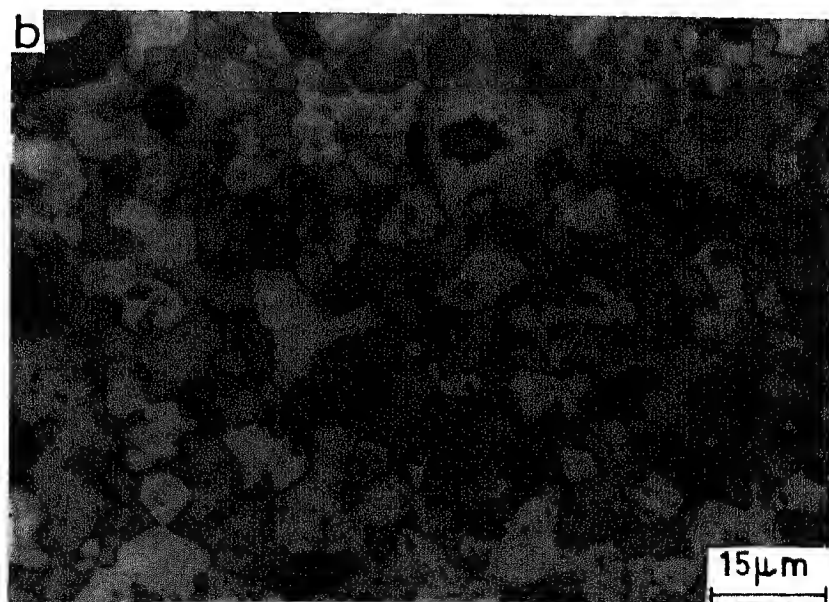
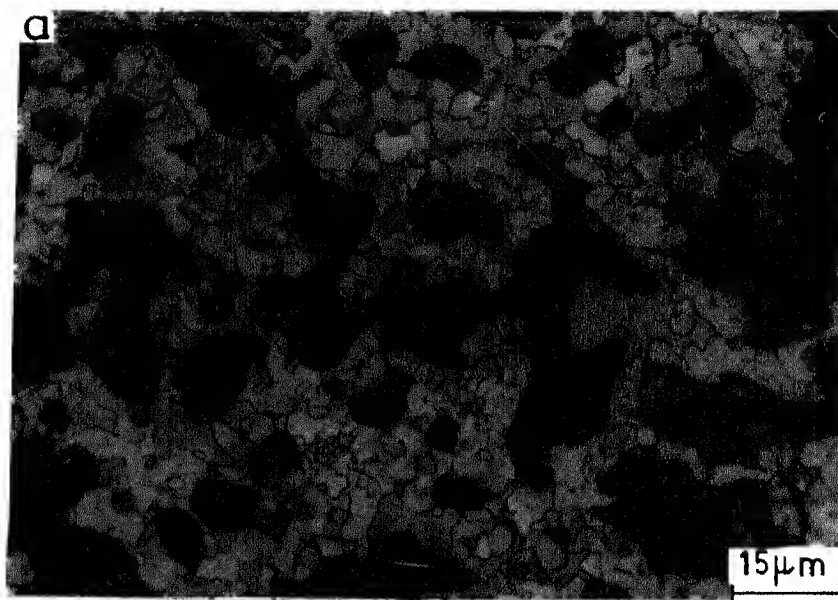
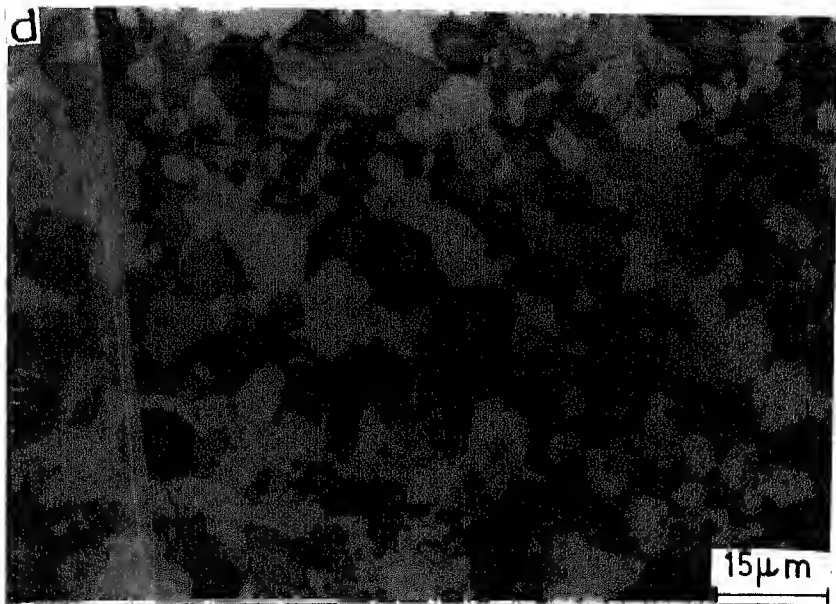
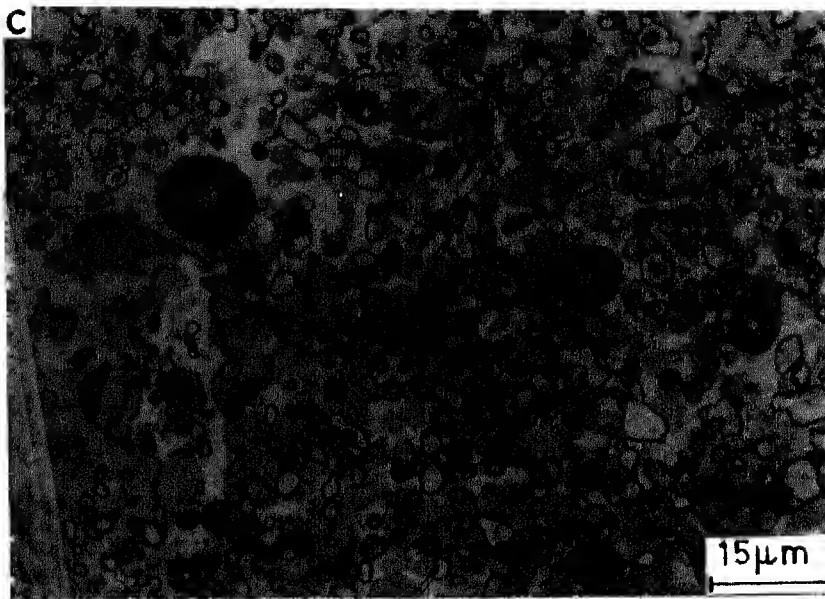


Fig. 3.11. Indentation Fracture Toughness Variation of Mo_2FeB_2 - αFe Cermets Prepared Through the MoB Route at 1350°C Sintering Temperature.





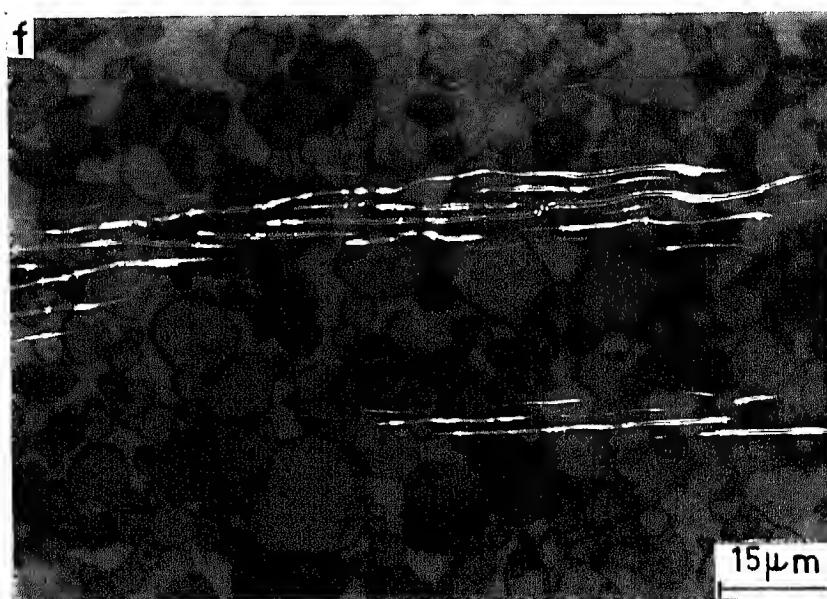
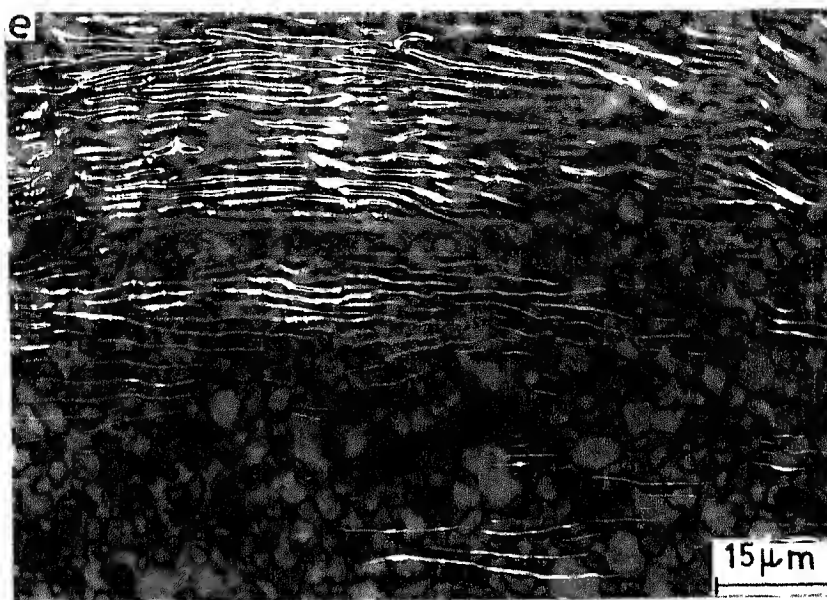


Fig. 3.12 Optical microstructures of Mo_2FeB_2 - αFe and its based cermetes prepared through elemental and MoB routes (sintering temperature 1350°C):

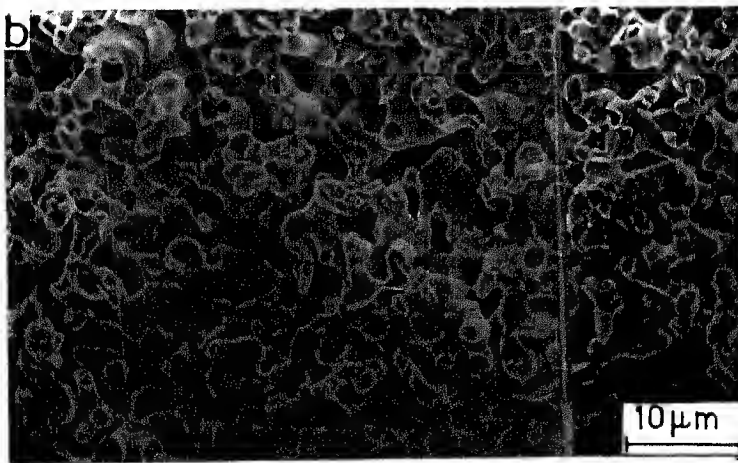
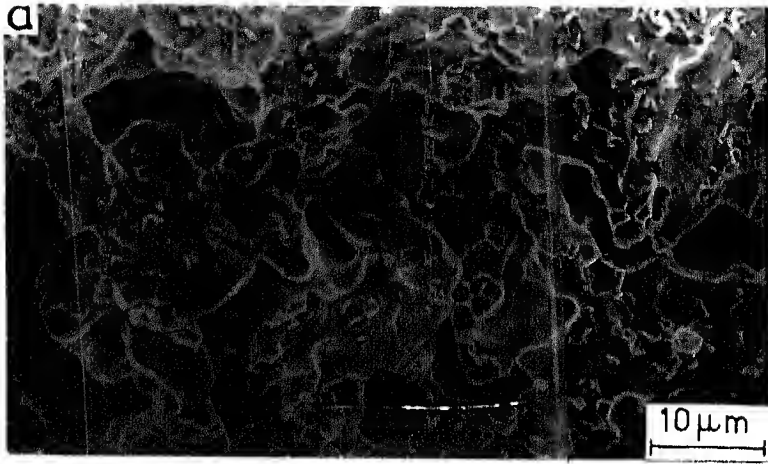
- (a) Mo_2FeB_2 (Elemental route)
- (b) Mo_2FeB_2 (MoB route)
- (c) Mo_2FeB_2 -12.43 vol.% αFe (Elemental route)
- (d) Mo_2FeB_2 -12.43 vol.% αFe (MoB route)
- (e) Mo_2FeB_2 -25.62 vol.% αFe (Elemental route)
- (f) Mo_2FeB_2 -25.62 vol.% αFe (MoB route)

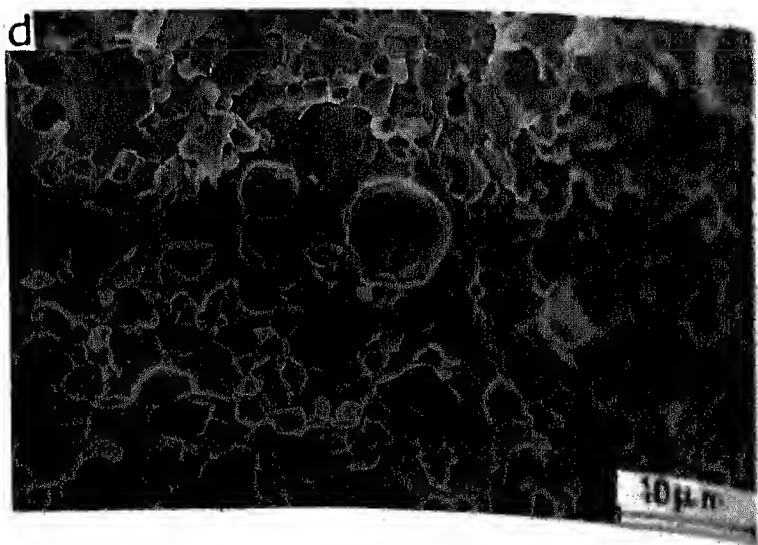
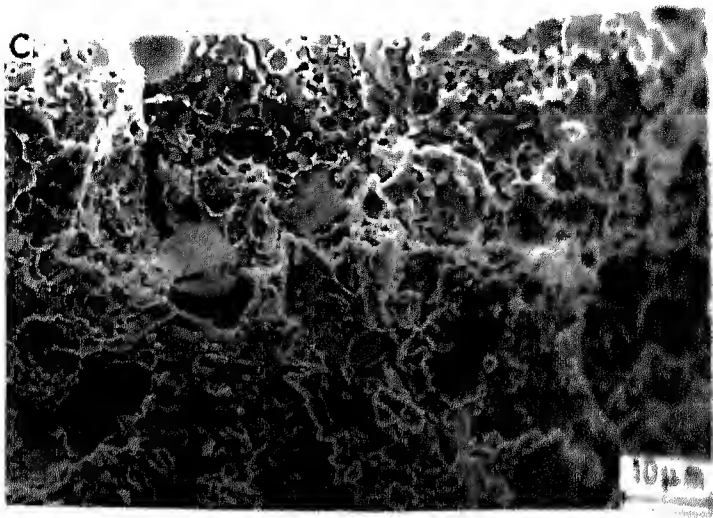
consist of fine irregular geometrical shaped boride grains with interconnected and almost spherical isolated pores. The MoB route, on the other hand, exhibits relatively less amount of porosity, the porosity is approximately 9.05 % and are isolated spherical in nature. The microstructures reflect boride grain coarsening with irregular geometrical shaped boride grains.

Mo_2FeB_2 - 12.43 vol. % α Fe cermet prepared through the elemental route after 1350°C sintering exhibits fine uniform irregular geometrical shaped boride grains with small spherical isolated pores (Fig. 12c). While boride grain coarsening is quite predominant in case of MoB route with relatively large amount of spherical isolated pores (Fig. 12d).

Cermet containing 25.62 vol.% α -iron binder prepared through the elemental route after 1350°C sintering shows fine uniform boride grains with almost zero porosity (Fig. 12e). The boride grains are surrounded by the α -iron binder. The MoB processing route is characterized by excessive boride grain coarsening with large spherical isolated pores. The large boride grains are also uniformly distributed in the α -iron binder (Fig. 12f).

Fig. 3.13 (a) and (b) show the secondary electron image of the TRS fractured straight Mo_2FeB_2 boride prepared through elemental and MoB routes after 1350°C. It is evident from the fractograph that elemental route exhibits highly interconnected pores with few isolated pores and the failure is characterized by the intergranular dimple brittle fracture mode with quasicleavage facets. The MoB route shows uniformly distributed isolated pores with few interconnected pores. The intergranular brittle





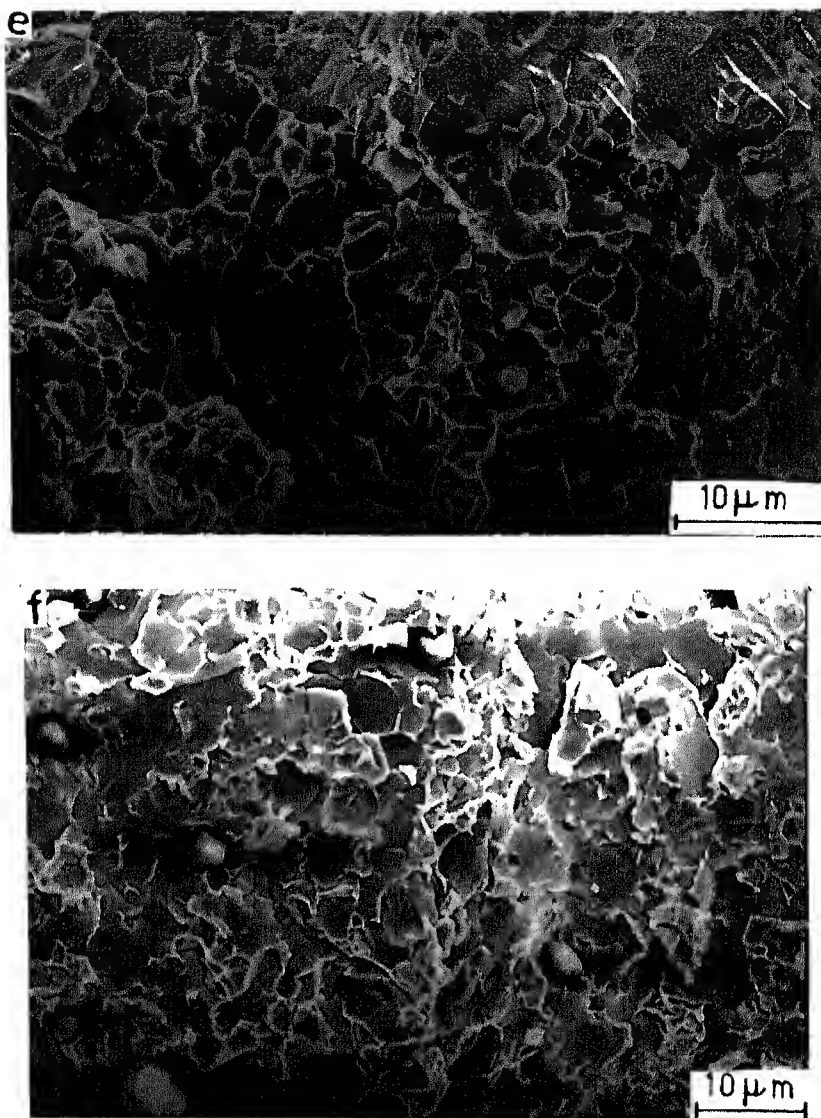


Fig. 3.13 SEM Fractographs of Mo_2FeB_2 and its based cermets sintered at 1350°C :

- (a) Mo_2FeB_2 (Elemental route)
- (b) Mo_2FeB_2 (MoB route)
- (c) Mo_2FeB_2 -12.43 vol.% αFe (Elemental route)
- (d) Mo_2FeB_2 -12.43 vol.% αFe (MoB route)
- (e) Mo_2FeB_2 - 25.62 vol.% αFe (Elemental route)
- (f) Mo_2FeB_2 - 25.62 vol.% αFe (MoB route)

fracture of boride grains reveals the dimple brittle fracture.

Fig. 3.13 (c) and (d) show the SEM fractographs of Mo_2FeB_2 - 12.43 vol.% α Fe cermets prepared through the elemental and MoB routes after 1350°C. The elemental route exhibits dimple fracture with large quasicleavage facets, cracks are also predominant at the fractured boride grain boundary regions. The fractured surface exhibits large amount of isolated pores. MoB route exhibits almost equiaxed nonuniform size dimple fracture with quasicleavage facets. Very little spherical isolated pores are present on the fractured surface.

Fig. 3.13 (e) and (f) show the SEM fractographs of Mo_2FeB_2 -25.62 vol.% α Fe cermets prepared through the elemental and MoB routes after 1350°C sintering. The elemental route is characterized by the equiaxed nonuniform size fine dimple inter granular brittle failure with quasicleavage facets. The fractured surface contains spherical isolated pores, whereas, the MoB route exhibits large quasicleavage facets.

3.5 X-RAY DIFFRACTION ANALYSIS

X-ray diffraction studies confirmed the presence of only two phases Mo_2FeB_2 and α Fe. Fig. 3.14 shows lattice parameter variation of both hard and binder phases. Mo_2FeB_2 exhibits tetragonal lattice configuration. It is evident that the variation in lattice parameters of the hard phase are insignificant in either processing route and are within the error limit. Lattice parameter of the binder phase i.e. α Fe also reflects identical pattern. Some of the x-ray results are given in Appendix.

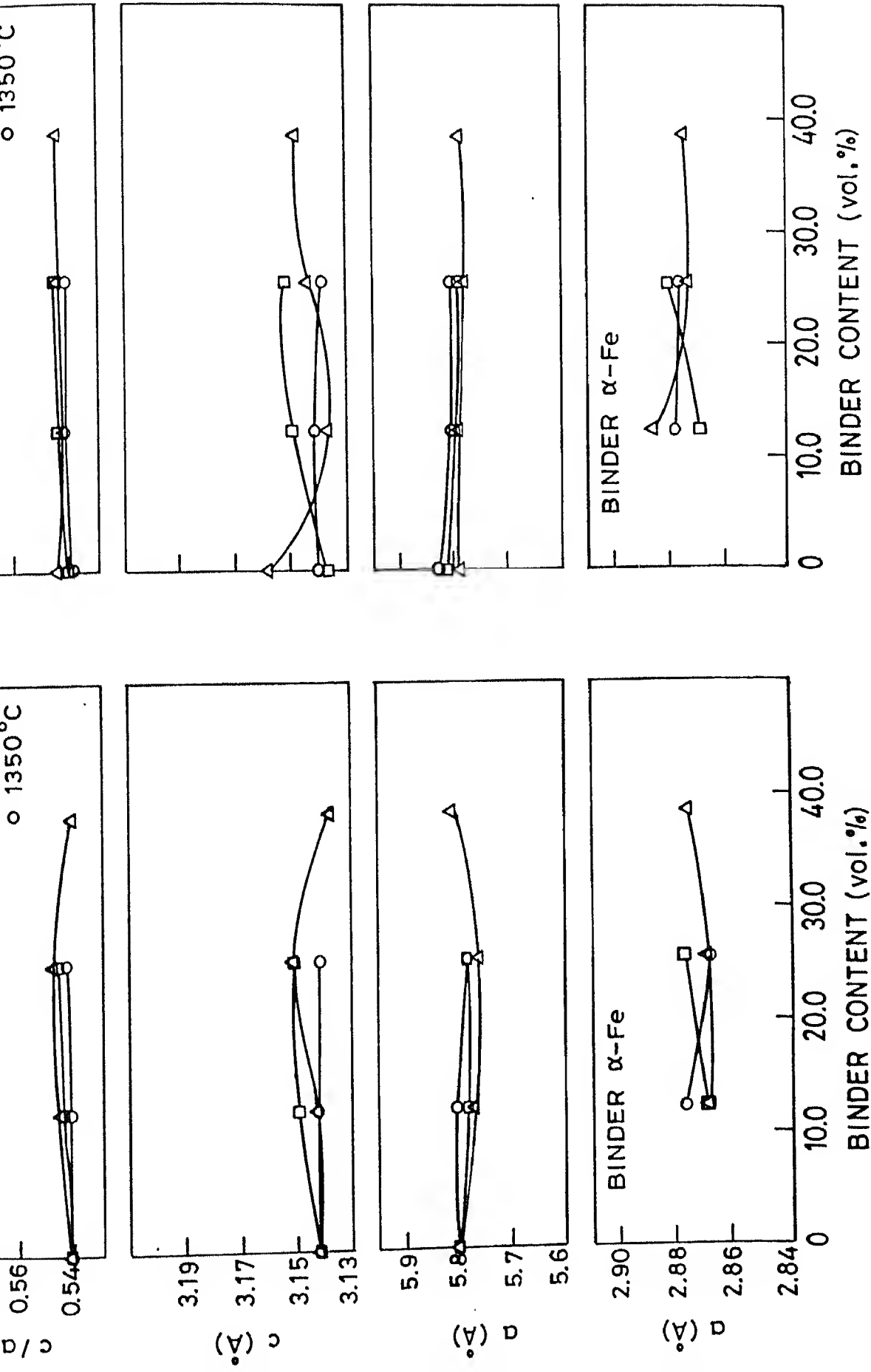


Fig. 3.14 Lattice parameter variation of hard and binder phases in Mo_2FeB_2 - αFe cermet prepared through elemental and MoB routes at different temperatures.

3.6 SATURATION MAGNETIC FLUX DENSITY

The variation in the saturation magnetic flux density with the binder content is shown in Fig. 3.15. The noteworthy feature is that saturation magnetic flux density increases almost linearly with the increase in binder content in case of cermets prepared from the elemental route. The MoB processing route exhibits almost an identical relation. The value for 12.43 vol.% binder cermet prepared through the elemental route is somewhat higher than that prepared through the MoB route.

3.7 THERMAL SHOCK RESISTANCE

Table 3.3 shows the thermal shock resistance variation of cermets, from which it is evident that there is no effect of binder content on this property.

Table 3.3 : Thermal shock resistance (ΔT) variation of Mo_2FeB_2 - α Fe cermets prepared through the MoB route

Binder Content (vol.% α Fe)	ΔT ($^{\circ}\text{C}$)
0	< 370
12.43	< 370
25.62	< 370

3.8 CORROSION WEIGHT LOSS STUDY

Corrosion weight loss study was carried out in case of Mo_2FeB_2 - α Fe sintered cermets prepared through the MoB route at 1350°C . Fig. 3.16 shows the corrosion rate of Mo_2FeB_2 and its based cermets in 10 wt.% HCl and 10 wt.% HF solutions for 10 hours respectively. It is evident from the figure that the straight Mo_2FeB_2 boride exhibits maximum corrosion rate in both corrosive media. Cermet containing 12.43 vol.% α Fe binder shows least corrosion rate among all the investigated cermets. The

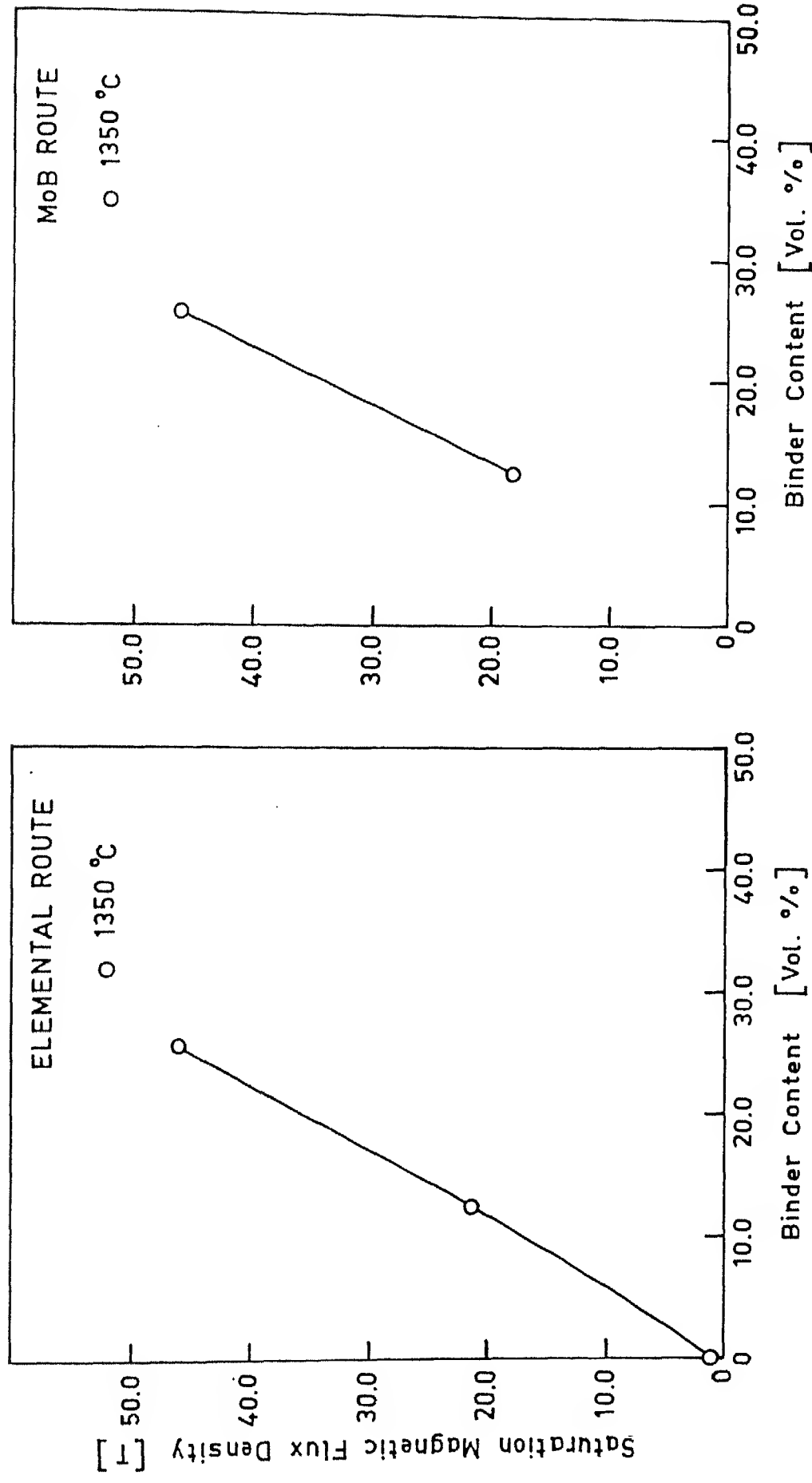


Fig. 3.15. Saturation magnetic flux density variation of Mo_2FeB_2 - αFe cermets prepared through elemental and MoB routes and sintered at 1350 °C.

Alloy 1 (0 vol.% Binder); Alloy 2 (12.43 vol.% Binder);

Alloy 3 (25.62 vol.% Binder)

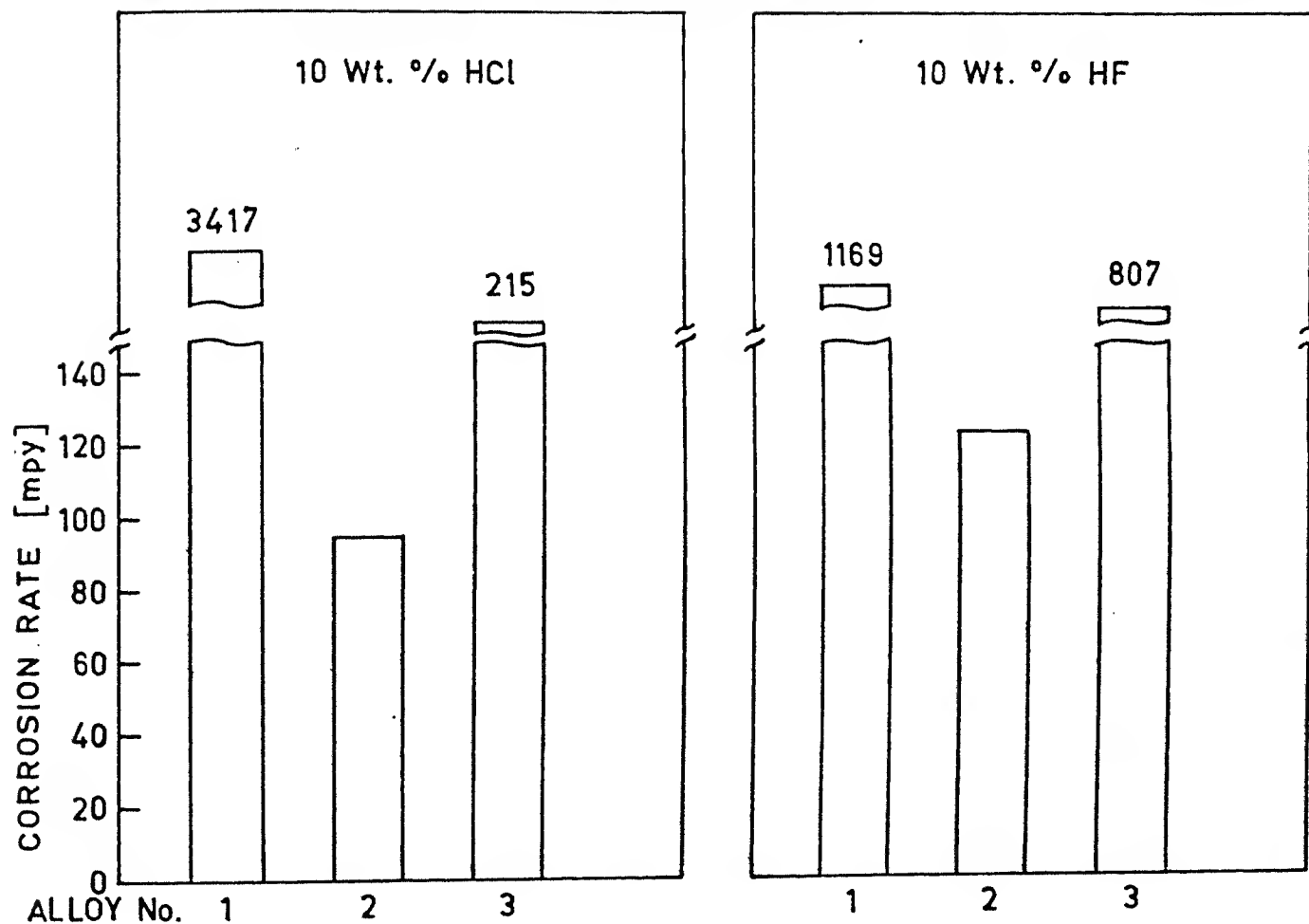


Fig. 3.16. Corrosion Rate of $\text{Mo}_2\text{FeB}_2 - \alpha\text{Fe}$ Cermets in 10 wt. % HCl and 10 wt. % HF Solutions for 10 Hours Respectively.

corrosion rate increases rapidly with the further increase in binder content to 25.62 vol.% α Fe.

PART II : SINTERING OF $\text{Mo}_2\text{Fe}(\text{Ni})\text{B}_2$ - $\text{Fe}(\text{Ni})$ CERMETS THROUGH THE MoB ROUTE

3.9 CHARACTERIZATION OF MILLED POWDER

Fig. 3.17 and 3.18 show the particle size distribution of various ball milled powder premixes prepared through the MoB route. Table 3.4 gives the data of the average particle size of milled powders corresponding to different $\text{Mo}_2\text{Fe}(\text{Ni})\text{B}_2$ - $\text{Fe}(\text{Ni})$ cermet compositions. It is evident that with the increase in iron and nickel binders the average particle size increases. Fe-Ni-MoB powder premixes do not follow a systematic average particle size variation with the increase in the binder content.

3.10 DENSIFICATION BEHAVIOUR

Various densification properties i.e. % volume shrinkage, sintered density, % total sintered porosity and densification parameter are described below.

Table 3.4 : Average particle size of the various powder premixes used for the P/M processing of the $\text{Mo}_2\text{Fe}(\text{Ni})\text{B}_2$ - $\text{Fe}(\text{Ni})$ cermets through the MoB route.

Mo_2FeB_2 - αFe Cermets		$\text{Mo}_2(\text{Fe}_{0.5}\text{Ni}_{0.5})\text{B}_2$ - $\gamma(\text{FeNi})$ Cermets		Mo_2NiB_2 -Ni Cermets	
Binder Content α Fe (vol.%)	Average Particle Size (μm)	Binder Content $\gamma(\text{FeNi})$ (vol.%)	Average Particle Size (μm)	Binder Content Ni (vol.%)	Average Particle Size (μm)
0	2.21	0	2.76	0	2.53
12.43	2.25	11.51	1.98	10.88	2.57
25.62	2.47	24.41	2.03	23.74	3.07
-	-	37.22	1.93	-	-

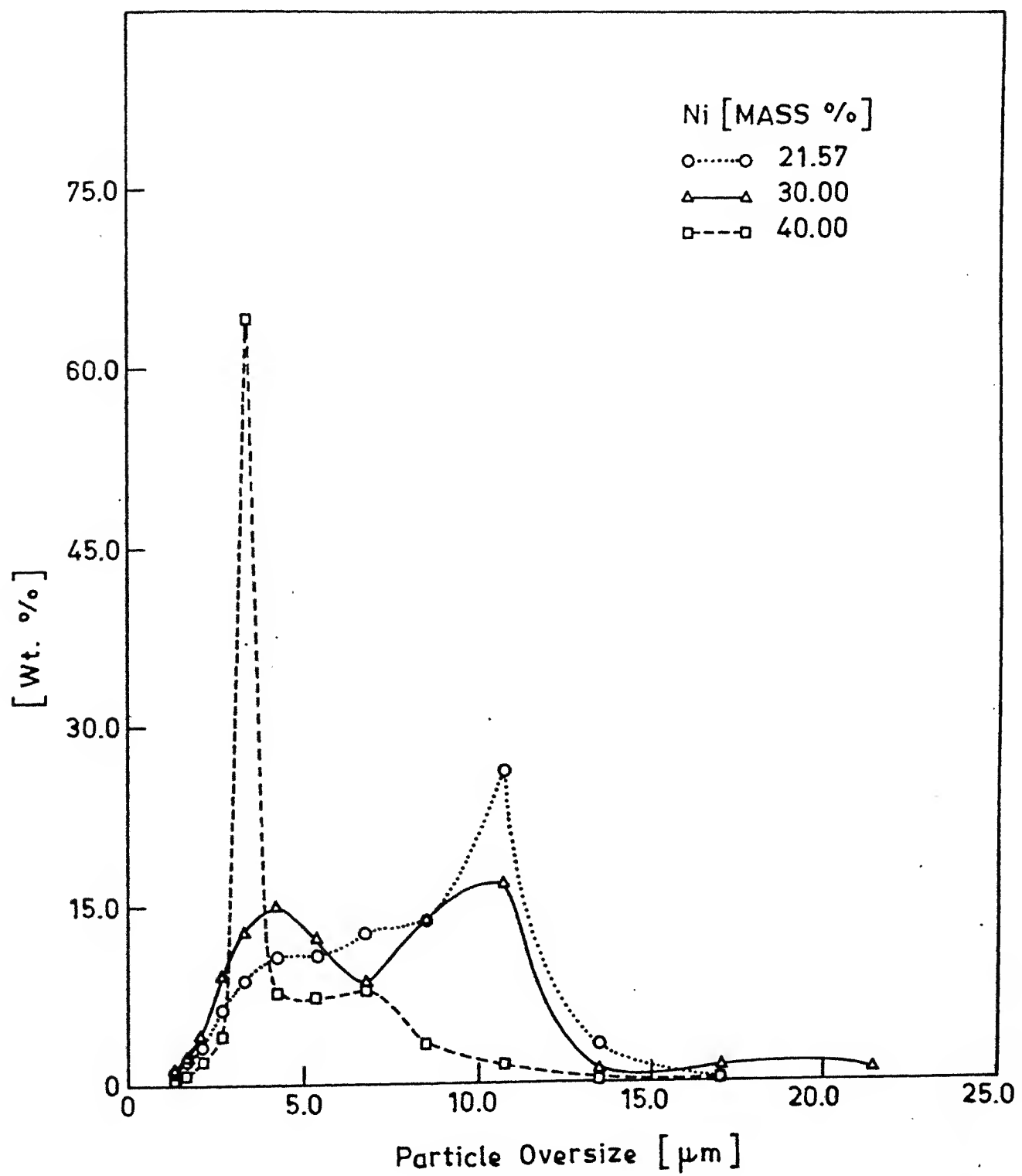


Fig. 3.18. Particle size distribution of the MoB-Ni powder premixes.

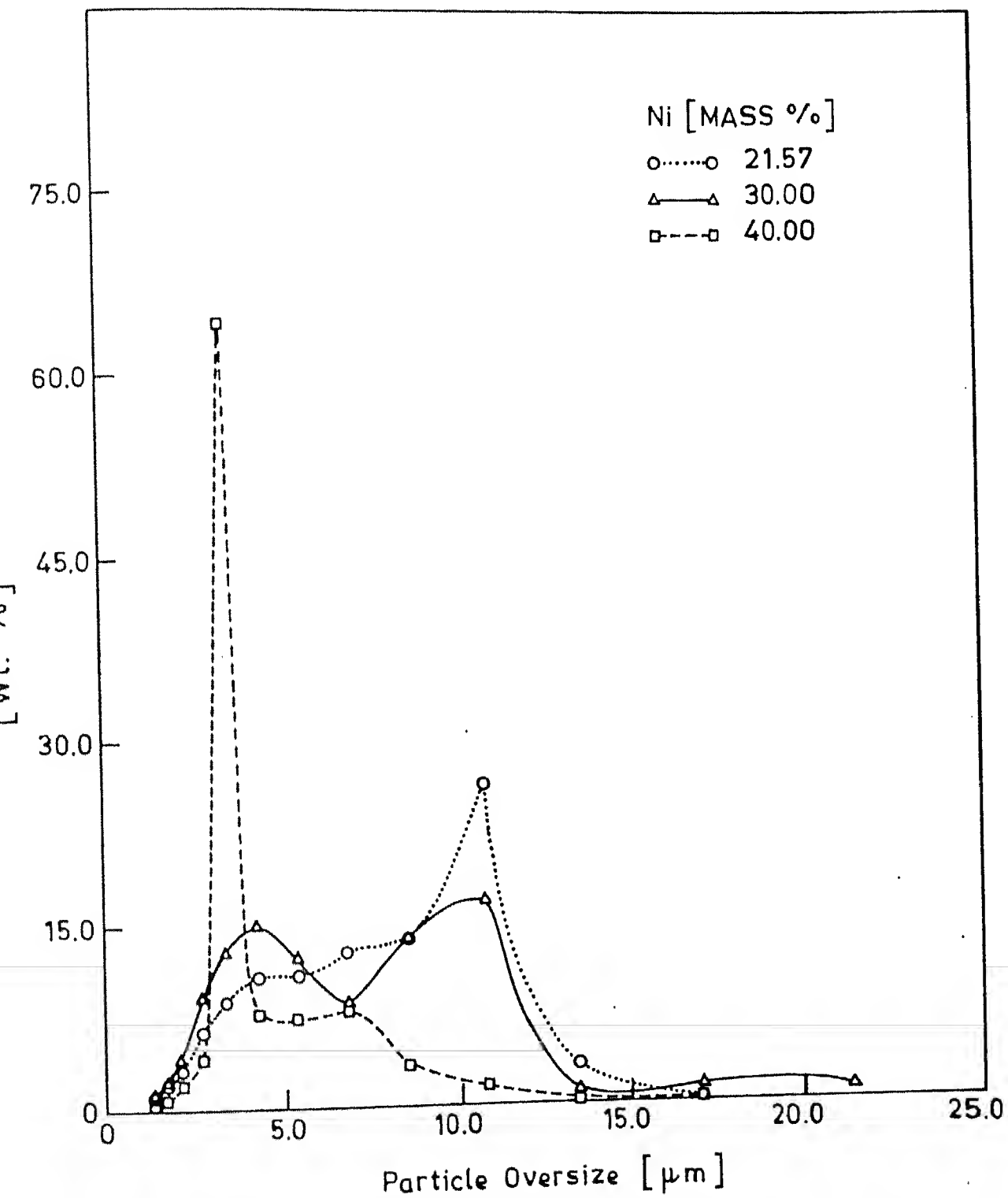


Fig. 3.18. Particle size distribution of the MoB-Ni powder premixes.

3.10.1 % Volume Shrinkage

The relationship between the % volume shrinkage and the binder content of $\text{Mo}_2\text{Fe}(\text{Ni})\text{B}_2\text{-Fe}(\text{Ni})$ cermets is shown in Fig 3.19.

% Volume shrinkage of $\text{Mo}_2\text{Fe}(\text{Ni})\text{B}_2\text{-Fe}(\text{Ni})$ cermets in general increases with the increase in $\text{Fe}(\text{Ni})$ binder content with the exception in $\text{Mo}_2(\text{Fe}_{0.5}\text{Ni}_{0.5})\text{B}_2 - 11.51\gamma(\text{FeNi})$ (vol%) cermet, where it exhibits slight decrease with respect to the straight $\text{Mo}_2(\text{Fe}_{0.5}\text{Ni}_{0.5})\text{B}_2$ boride. $\text{Mo}_2\text{Fe}(\text{Ni})\text{B}_2\text{-Fe}(\text{Ni})$ cermets do not show any swelling after sintering at 1350°C . Mo_2NiB_2 straight boride gives rise to a maximum % volume shrinkage and it is almost in proximity with the straight $\text{Mo}_2(\text{Fe}_{0.5}\text{Ni}_{0.5})\text{B}_2$ boride. $\text{Mo}_2\text{FeB}_2 - \alpha \text{Fe}$ cermets exhibit a rapid increase in % volume shrinkage in the initial stage. At higher than 12.43 vol% α -iron binder addition, it further increases slightly. The effect of binder in the remaining two groups of cermets do not reflect significant change in % volume shrinkage variation.

3.10.2 Sintered Density

Sintered density of $\text{Mo}_2\text{Fe}(\text{Ni})\text{B}_2\text{-Fe}(\text{Ni})$ cermets, in general, increases with the increase in $\text{Fe}(\text{Ni})$ binder content (Fig. 3.20).

In case of $\text{Mo}_2\text{FeB}_2 - \alpha \text{Fe}$ cermets, in the initial stage the sintered density increases quite significantly up to 12.43 vol% α -iron binder. Subsequently the value reduces slightly with further increase in the binder content.

$\text{Mo}_2\text{NiB}_2\text{-Ni}$ cermets exhibit a slight increase in sintered density in the initial stage. After 10.88 vol% nickel binder addition it does not vary quite significantly.

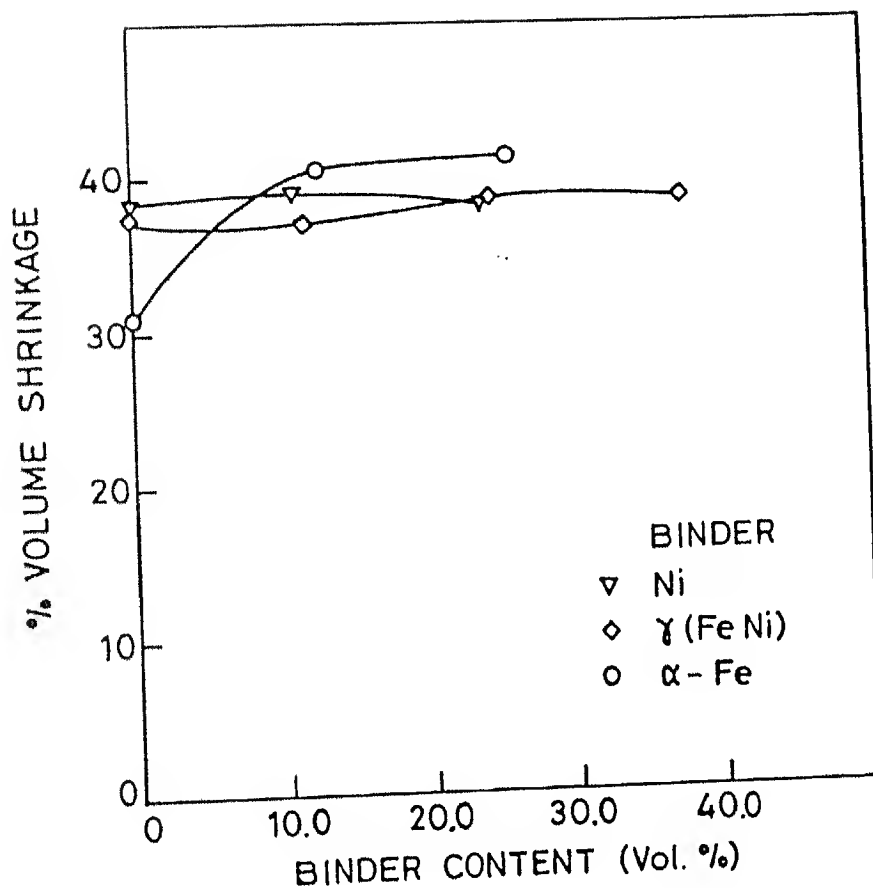


Fig. 3.19. % Volume shrinkage variation of $\text{Mo}_2\text{Fe}(\text{Ni})\text{B}_2\text{-Fe}(\text{Ni})$ cermets prepared through the MoB route and sintered at 1350°C .

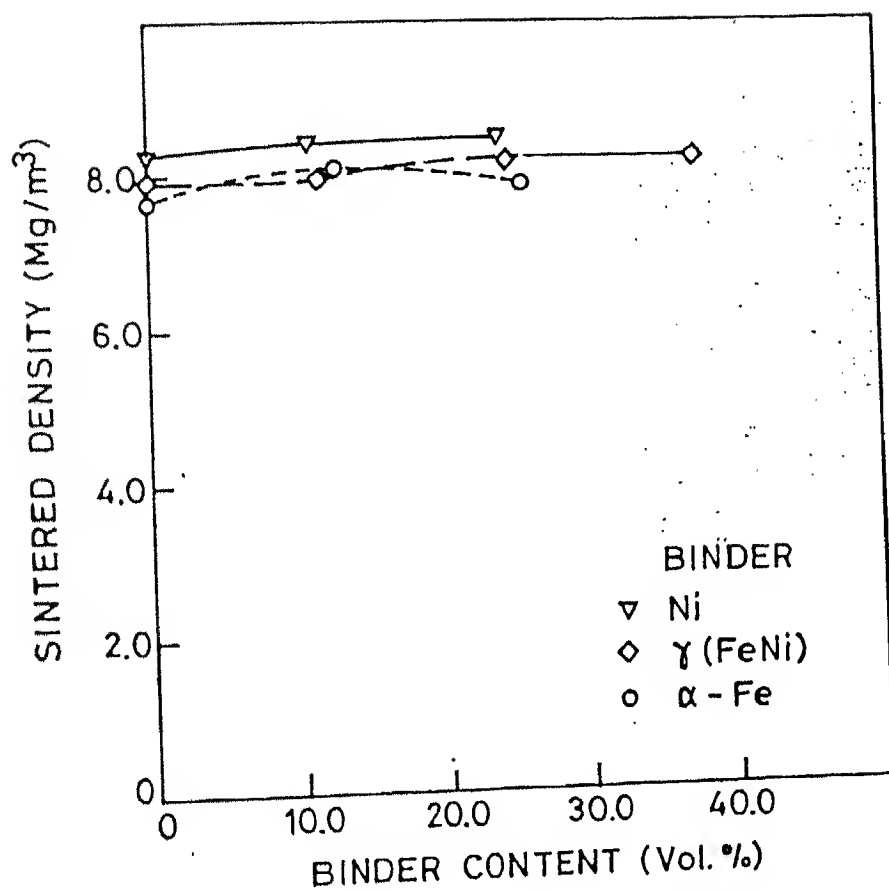


Fig. 3.20 Sintered density variation of $\text{Mo}_2\text{Fe}(\text{Ni})\text{B}_2\text{-Fe}(\text{Ni})$ cermet_s prepared through the MoB route and sintered at 1350°C .

$\text{Mo}_2(\text{Fe}_{0.5}\text{Ni}_{0.5})\text{B}_2 - \gamma(\text{FeNi})$ cermets follow almost an identical pattern in sintered density variation with the increase in $\gamma(\text{FeNi})$ binder content to that of $\text{Mo}_2\text{NiB}_2\text{-Ni}$ cermets. Initially the sintered density increases quite significantly. The variation in sintered density is insignificant after 24.40 vol% $\gamma(\text{FeNi})$ binder addition.

The noteworthy feature is that the straight $\text{Mo}_2(\text{Fe}_{0.5}\text{Ni}_{0.5})\text{B}_2$ boride exhibit higher sintered density as compared to the straight Mo_2FeB_2 boride, whereas $\text{Mo}_2\text{NiB}_2\text{-Ni}$ cermets give rise to maximum sintered density as compared to all other cermets.

3.10.3 % Total Sintered Porosity (% ϵ_{TS})

$\text{Mo}_2\text{Fe}(\text{Ni})\text{B}_2\text{-Fe}(\text{Ni})$ cermets exhibit a decrease in the % total sintered porosity with the increase in the $\text{Fe}(\text{Ni})$ binder content (Fig. 3.21).

In case of $\text{Mo}_2\text{FeB}_2\text{-}\alpha\text{Fe}$ cermets, in the initial stage % ϵ_{TS} decreases rapidly up to 12.43 vol.% α -iron binder addition. In the later stage % ϵ_{TS} increases with the increase in α -iron binder content.

$\text{Mo}_2\text{NiB}_2\text{-Ni}$ cermets show a rapid decrease in % ϵ_{TS} upto 10.88 vol.% nickel binder addition. Subsequently it decreases slightly with the increase in the binder content.

The variation in % ϵ_{TS} with the binder content in case of $\text{Mo}_2(\text{Fe}_{0.5}\text{Ni}_{0.5})\text{B}_2\text{-}\gamma(\text{FeNi})$ cermets follows almost an identical pattern to that of $\text{Mo}_2\text{NiB}_2\text{-Ni}$ cermets. Initially the decrease in % ϵ_{TS} is quite significant. After 24.41 vol.% $\gamma(\text{FeNi})$ binder addition the variation is not appreciable.

CENTRAL LIBRARY
I. I. T., KANPUR
121713
No. A.121713

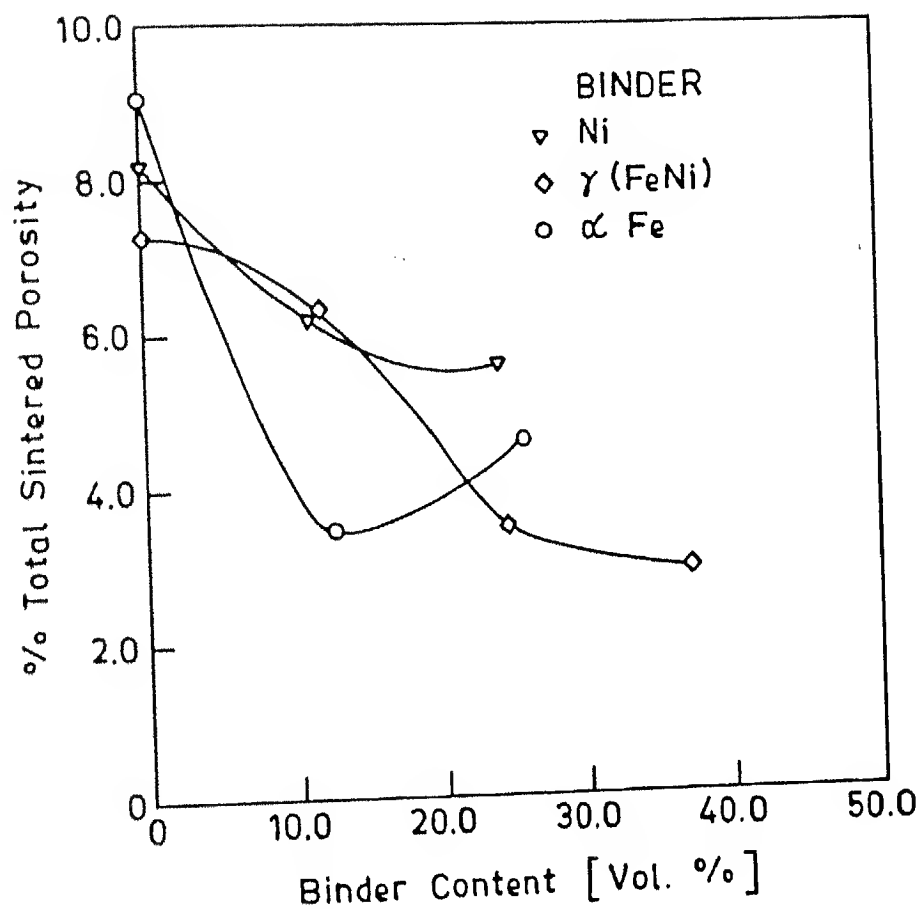


Fig. 3.21. % Total sintered porosity variation of $\text{Mo}_2\text{Fe}(\text{Ni})\text{B}_2\text{-Fe}(\text{Ni})$ cermets prepared through the MoB route and sintered at 1350°C .

The decrease in % ϵ_{TS} is noticed maximum in case of α -iron binder. The porosity variation of cermets containing γ (FeNi) binder is more or less similar to that of nickel bonded cermets, particularly in low volume fraction binder.

3.10.4 Densification Parameter

The effect of Fe(Ni) binder addition on the densification parameter of $\text{Mo}_2\text{Fe}(\text{Ni})\text{B}_2$ -Fe(Ni) cermets follows an increasing trend as shown in the Fig. 3.22.

Mo_2FeB_2 - α Fe Cermets exhibit a rapid increase in densification parameter in the initial stage. After 12.43 vol.% α -iron binder addition it reduces slightly with the further increase in binder content.

$\text{Mo}_2(\text{Fe}_{0.5}\text{Ni}_{0.5})\text{B}_2$ - γ (FeNi) cermets also exhibit a parallel relationship in densification behaviour as compared to the Mo_2NiB_2 -Ni cermets. Initially densification parameter increases quite significantly. After 24.41 vol.% γ (FeNi) binder addition, the variation in densification parameter is insignificant.

The straight $\text{Mo}_2(\text{Fe}_{0.5}\text{Ni}_{0.5})\text{B}_2$ and Mo_2NiB_2 ternary borides exhibit higher densification parameter as compared to the straight Mo_2FeB_2 boride, the former values are in proximity. $\text{Mo}_2(\text{Fe}_{0.5}\text{Ni}_{0.5})\text{B}_2$ - γ (FeNi) cermets containing 37.22 vol.% γ (FeNi) binder exhibit maximum densification parameter of 0.92.

3.11 MECHANICAL PROPERTIES

Various mechanical properties of $\text{Mo}_2\text{Fe}(\text{Ni})\text{B}_2$ -Fe(Ni) cermets i.e. Vickers hardness, transverse rupture strength and indentation fracture toughness are described below.

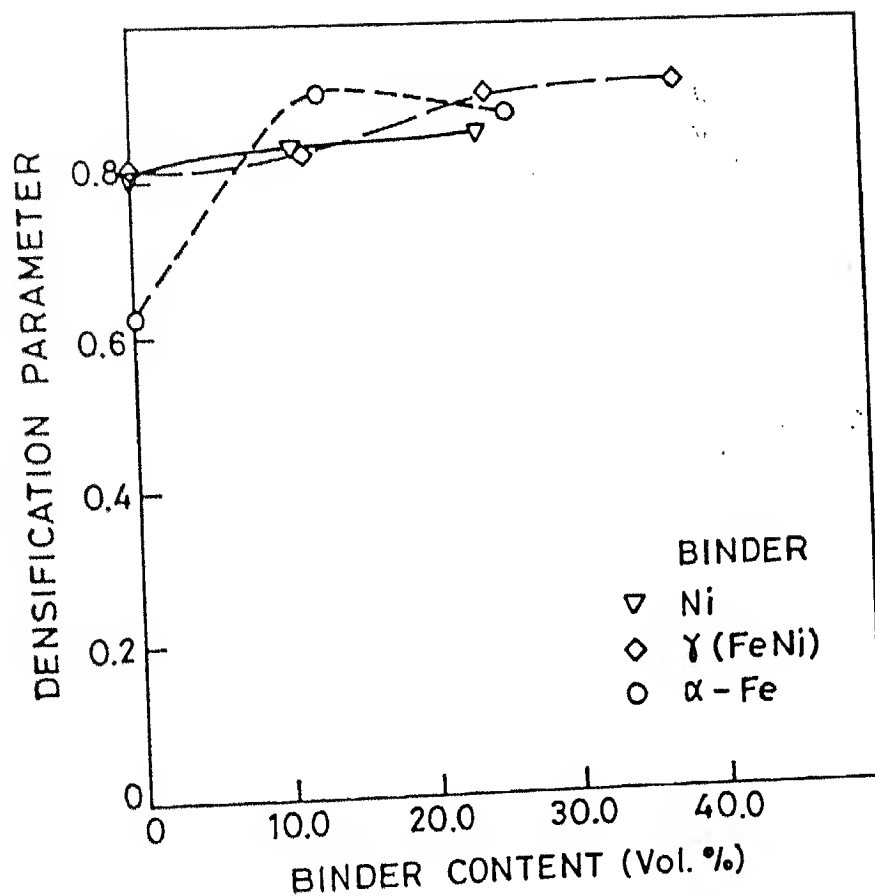


Fig. 3.22 Densification parameter variation of $\text{Mo}_2\text{Fe}(\text{Ni})\text{B}_2$ - $\text{Fe}(\text{Ni})$ cermet prepared through the MoB route and sintered at 1350°C .

3.11.1 Vickers Hardness

The relationship between Vickers hardness with the binder content in $\text{Mo}_2\text{Fe}(\text{Ni})\text{B}_2\text{-Fe}(\text{Ni})$ cermets is shown in the Fig. 3.23.

$\text{Mo}_2\text{FeB}_2\text{-}\alpha$ Fe cermets exhibit an increase in Vickers hardness with the increase in binder content. In the initial stage Vickers hardness increases drastically up to 12.43 vol.% binder and in the later stage the decrease is quite significant with the increase in binder content.

In case of $\text{Mo}_2\text{NiB}_2\text{-Ni}$ cermets Vickers hardness variation shows a reverse relationship. Vickers hardness decreases almost linearly with the increase in the binder content.

$\text{Mo}_2(\text{Fe}_{0.5}\text{Ni}_{0.5})\text{B}_2\text{-}\gamma(\text{FeNi})$ cermets like $\text{Mo}_2\text{FeB}_2\text{-}\alpha$ Fe cermets shows an increase in hardness upto 11.51 vol.% $\gamma(\text{FeNi})$ binder addition. Subsequently, Vickers hardness decreases quite significantly with the increase in the binder content.

The characteristic feature among the investigated cermets is that the $\text{Mo}_2\text{FeB}_2\text{-}\alpha$ Fe cermet containing 12.43 vol.% α -iron binder exhibits a maximum hardness as high as 1195 kgf/mm^2 .

3.11.2 Transverse Rupture Strength (TRS)

$\text{Mo}_2\text{Fe}(\text{Ni})\text{B}_2\text{-Fe}(\text{Ni})$ cermets exhibit a significant increase in TRS with the increase in Fe(Ni) binder content (Fig. 3.24).

In case of $\text{Mo}_2\text{FeB}_2\text{-}\alpha$ Fe cermets TRS increases up to 12.43 vol.% α -iron binder addition. Later on it increases still rapidly with the increase in α -iron binder content.

The noteworthy feature is that the $\text{Mo}_2\text{NiB}_2\text{-Ni}$ cermets exhibit maximum TRS as compared to other investigated cermets. The straight Mo_2NiB_2 boride gives rise to a maximum TRS as

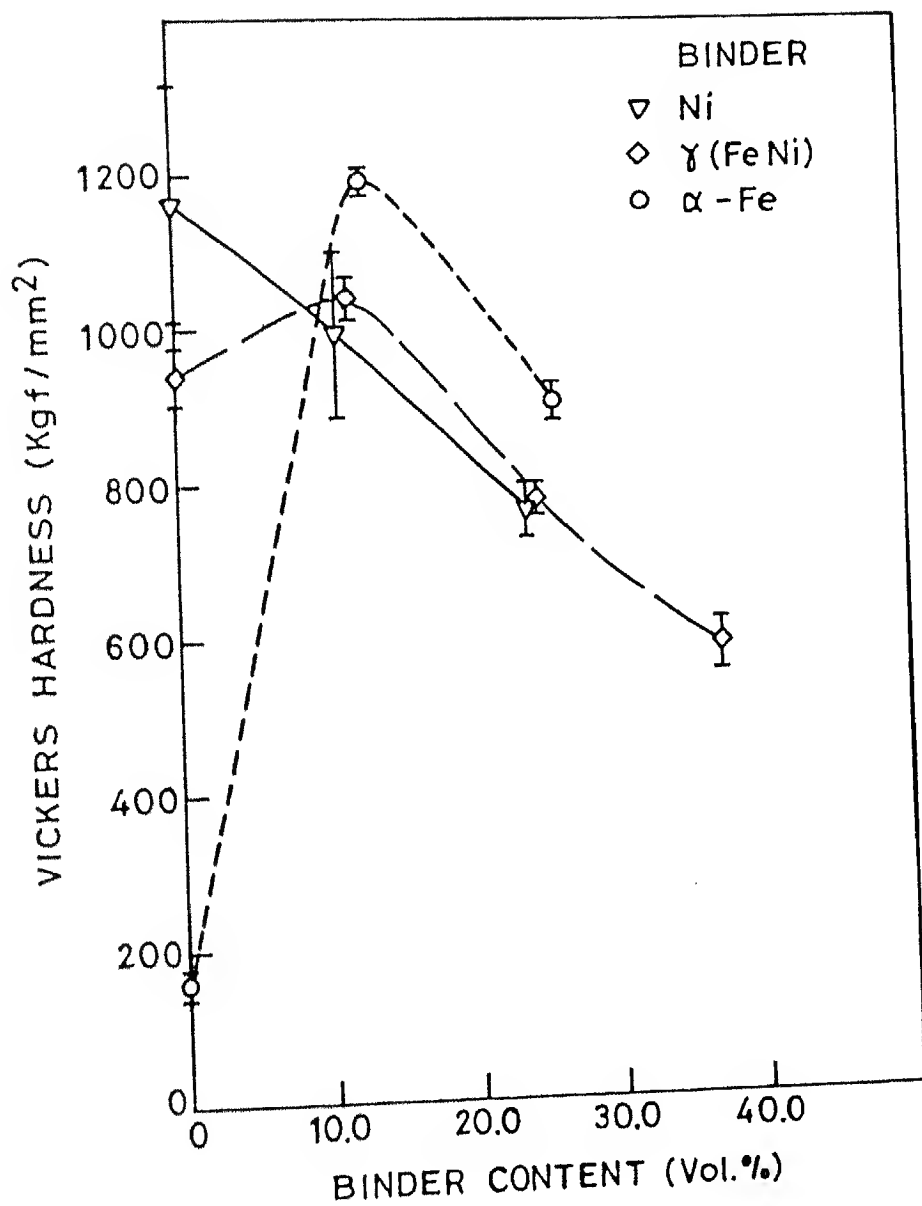


Fig. 3.23 Vickers hardness variation of $\text{Mo}_2\text{Fe}(\text{Ni})\text{B}_2 - \text{Fe}(\text{Ni})$ cermets prepared through the MoB route and sintered at 1350°C .

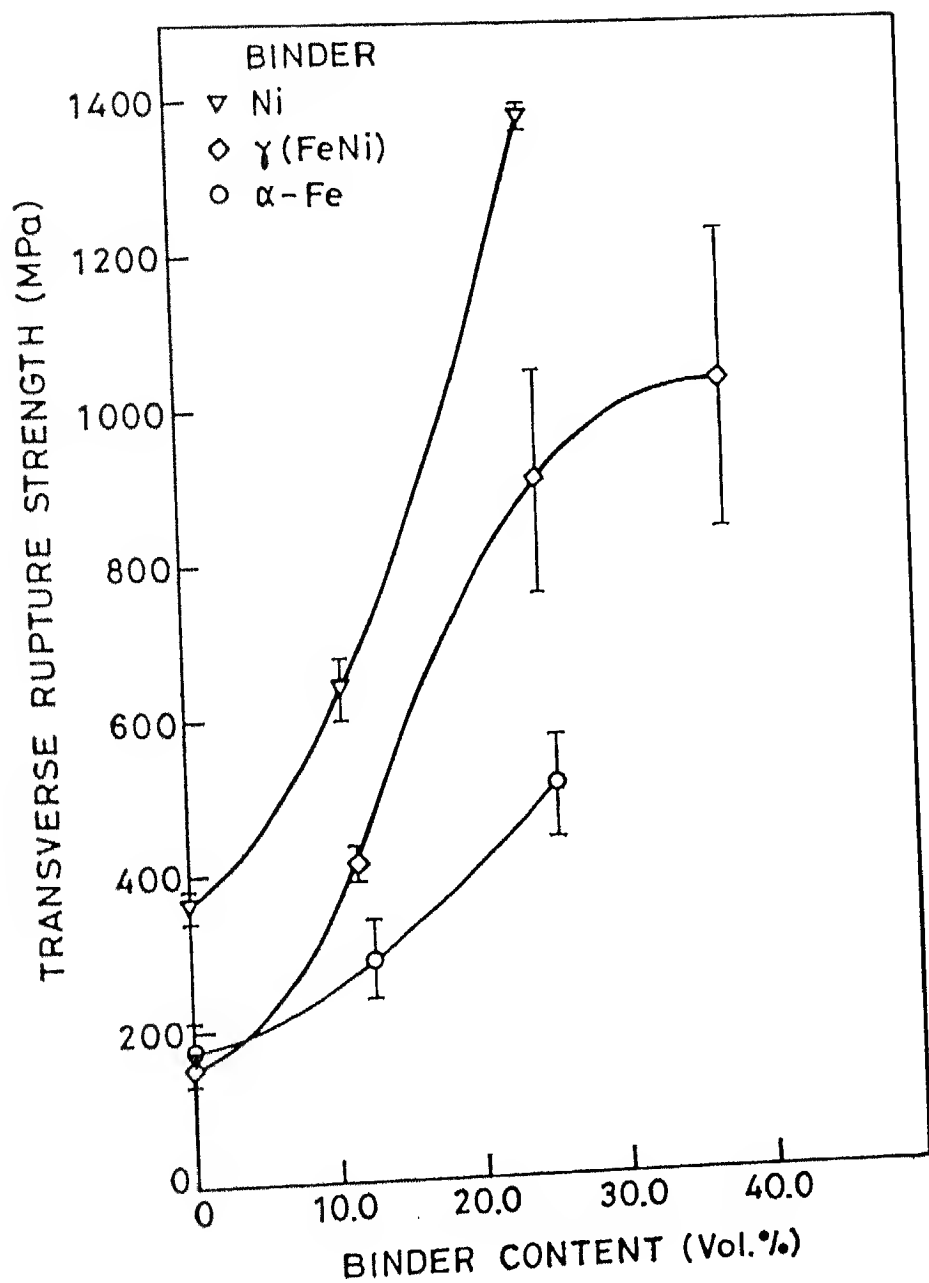


Fig. 3.24 Transverse rupture strength variation of $\text{Mo}_2\text{Fe}(\text{Ni})\text{B}_2$ -Fe(Ni) cermet prepared through the MoB route and sintered at 1350°C .

compared to the straight Mo_2FeB_2 and $\text{Mo}_2(\text{Fe}_{0.5}\text{Ni}_{0.5})\text{B}_2$ borides, where the values are almost in proximity. Mo_2NiB_2 -Ni cermet containing 23.74 vol% nickel binder exhibits a maximum TRS of 1380 MPa.

3.11.3 Indentation Fracture Toughness (Kc)

$\text{Mo}_2\text{Fe}(\text{Ni})\text{B}_2$ -Fe(Ni) cermets exhibit an increase in indentation fracture toughness with the increase in Fe(Ni) binder content (Fig 3.25).

In case of Mo_2FeB_2 - α Fe cermets indentation fracture toughness increases uniformly with the increase in binder content.

Mo_2NiB_2 -Ni cermets like Mo_2FeB_2 - α Fe cermets show an uniform increase in indentation fracture toughness with the increase in the binder content. The straight Mo_2NiB_2 boride phase exhibits 35% increase in indentation fracture toughness as compared to the straight Mo_2FeB_2 boride. The sequence of indentation fracture toughness variation also follows the pattern similar to TRS. However, for a binder content greater than 24.41 vol% in case of $\gamma(\text{FeNi})$ binder the toughness drops drastically.

3.12 OPTICAL MICROSTRUCTURES AND SEM FRACTOGRAPHY

Fig. 3.26 (a), (b) and (c) show the optical microstructures of $\text{Mo}_2(\text{Fe}_{0.5}\text{Ni}_{0.5})\text{B}_2$ - $\gamma(\text{FeNi})$ cermets containing 11.51, 24.41 and 37.22 vol.% $\gamma(\text{FeNi})$ binders respectively. The microstructures consist of a mixture of cubic, spherical, angular and complex geometrical shaped boride grains. The grey and white $\gamma(\text{FeNi})$ binders are homogeneously distributed between the boride grains. The microstructures also reveal spherical isolated pores. The

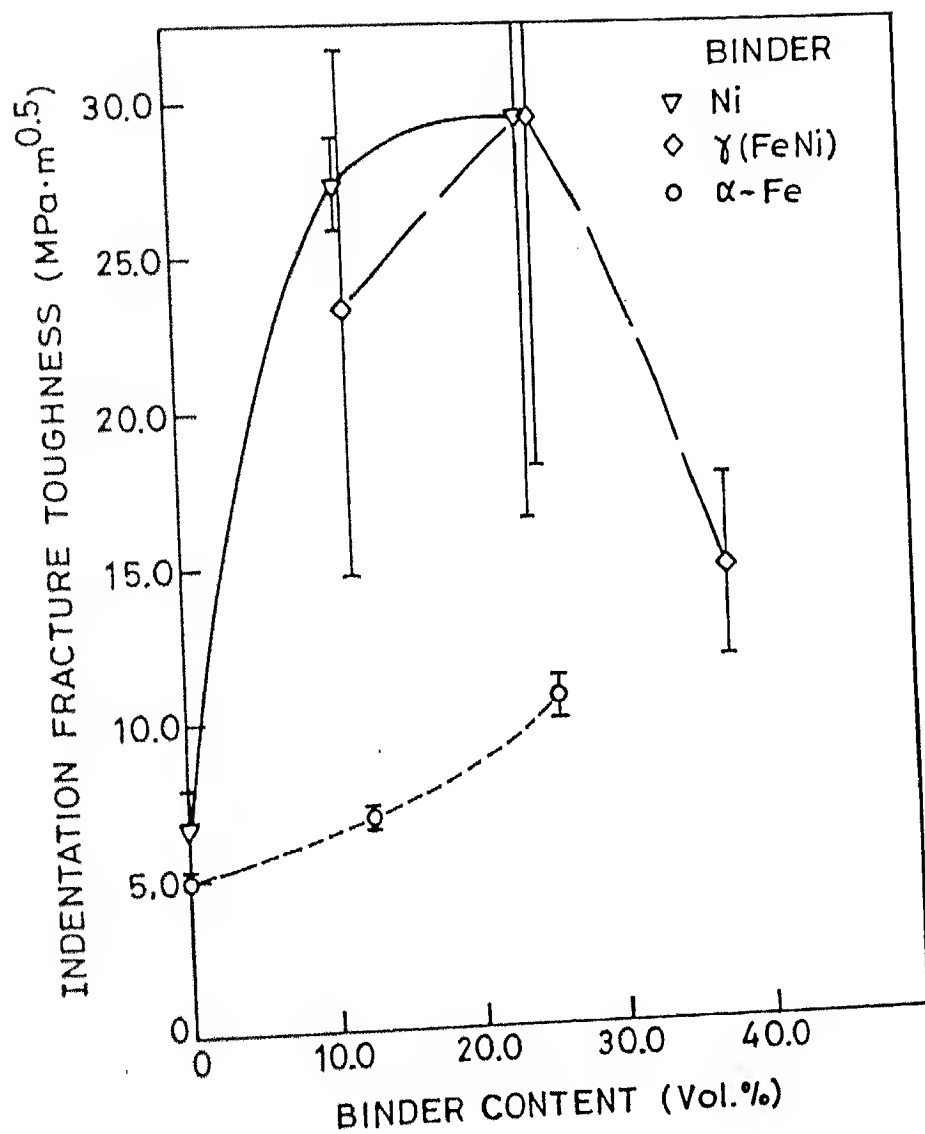
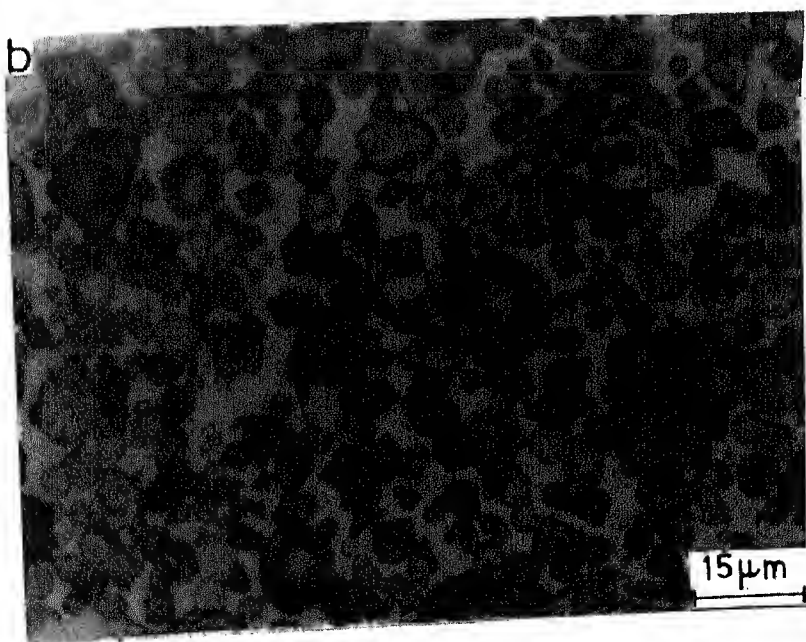
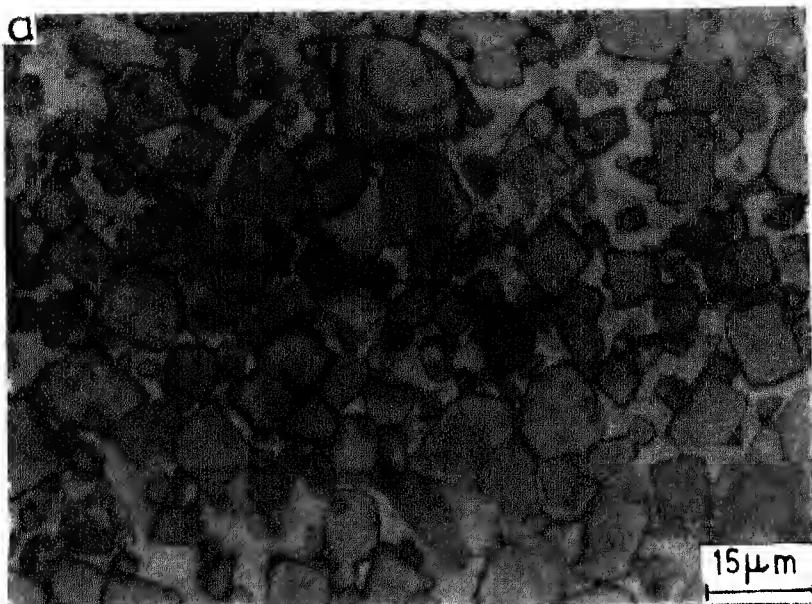


Fig. 3.25 Indentation Fracture toughness variation of $\text{Mo}_2\text{Fe}(\text{Ni})\text{B}_2\text{-Fe}(\text{Ni})$ cermet's prepared through the MoB route and sintered at 1350°C .



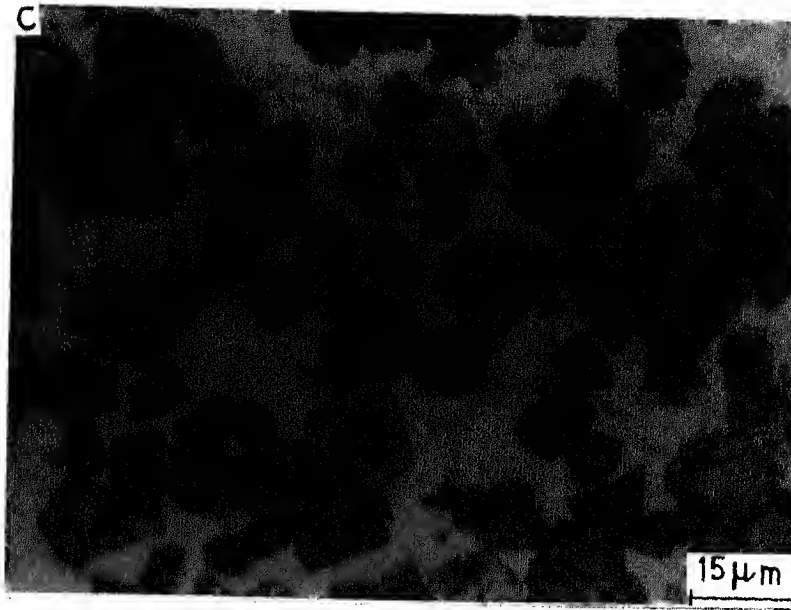


Fig. 3.26 Optical microstructures of $\text{Mo}_2(\text{Fe}_{0.5}\text{Ni}_{0.5})\text{B}_2$ based cermets prepared through the MoB route (Sintering temperature 1350°C) :

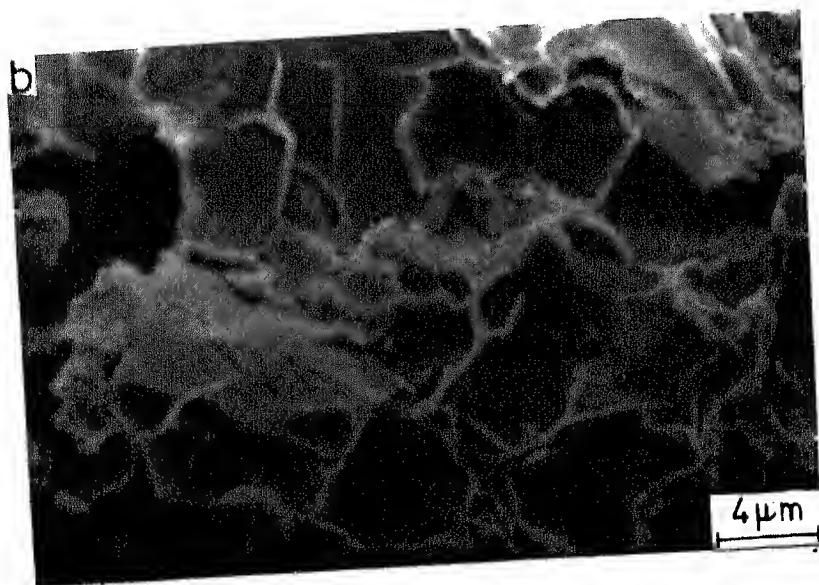
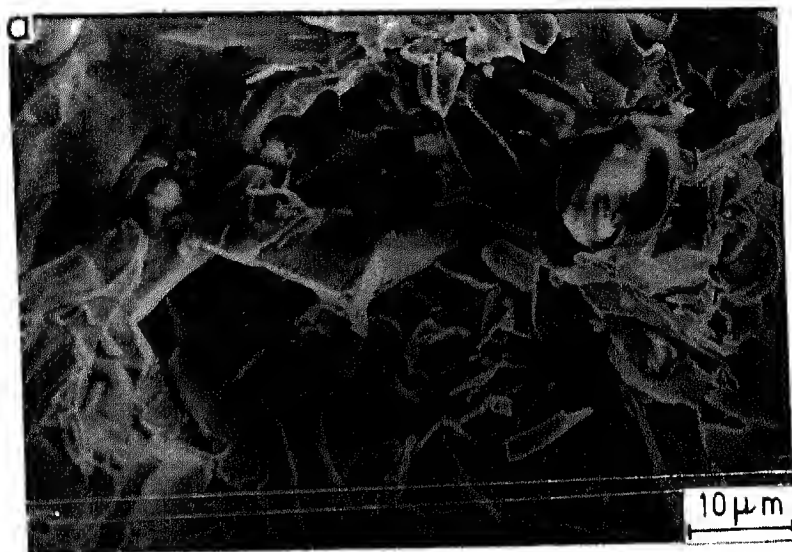
- (a) $\text{Mo}_2(\text{Fe}_{0.5}\text{Ni}_{0.5})\text{B}_2$ - 11.51 vol.% $\gamma(\text{FeNi})$
- (b) $\text{Mo}_2(\text{Fe}_{0.5}\text{Ni}_{0.5})\text{B}_2$ - 24.41 vol.% $\gamma(\text{FeNi})$
- (c) $\text{Mo}_2(\text{Fe}_{0.5}\text{Ni}_{0.5})\text{B}_2$ - 37.22 vol.% $\gamma(\text{FeNi})$

number and size of such pores decrease with the increase in $\gamma(\text{FeNi})$ binder content. Cermet containing 11.51 vol.% $\gamma(\text{FeNi})$ exhibits excessive boride grain coarsening Fig. 3.20(a), while 24.41 vol. % $\gamma(\text{FeNi})$ bonded cermet shows boride grain refinement (Fig. 3.26 b). With the increase in $\gamma(\text{Fe,Ni})$ binder to 37.22 vol.%, the microstructures also reveal boride grain coarsening.

Fig. 3.27 (a) shows the secondary electron image of the TRS fractured surface of the straight $\text{Mo}_2(\text{Fe}_{0.5}\text{Ni}_{0.5})\text{B}_2$ boride. The fractograph exhibits intergranular brittle fracture with quasicleavage elongated and plate type facets. Large cracks are quite predominant at the grain boundary regions. Large dimples and elongated facets are also predominant near the void region.

Cermet containing 11.51 vol.% $\gamma(\text{FeNi})$ binder exhibits unequiaxed dimple intergranular brittle fracture with quasicleavage facets. The fractograph contains large cracks along the grain boundary region Fig. 3.27 (b). With the increase in $\gamma(\text{FeNi})$ binder content to 24.41 and 37.22 vol.% the fractographs reveal intergranular equiaxed dimple brittle fracture. The presence of large cracks along the grain boundary region and quasicleavage facets reflect severity of brittle failure.

Fig. 3.28(a), (b) and (c) show the optical microstructures of the straight Mo_2NiB_2 boride and its nickel bonded cermets containing 10.88 and 23.74 vol. % nickel binders respectively. The microstructures consist of a mixture of cubic, rectangular parallelepiped and complex regular geometrical shaped boride grains. The grey and white nickel binder is uniformly distributed between the boride grains. The boride grain size increases uniformly



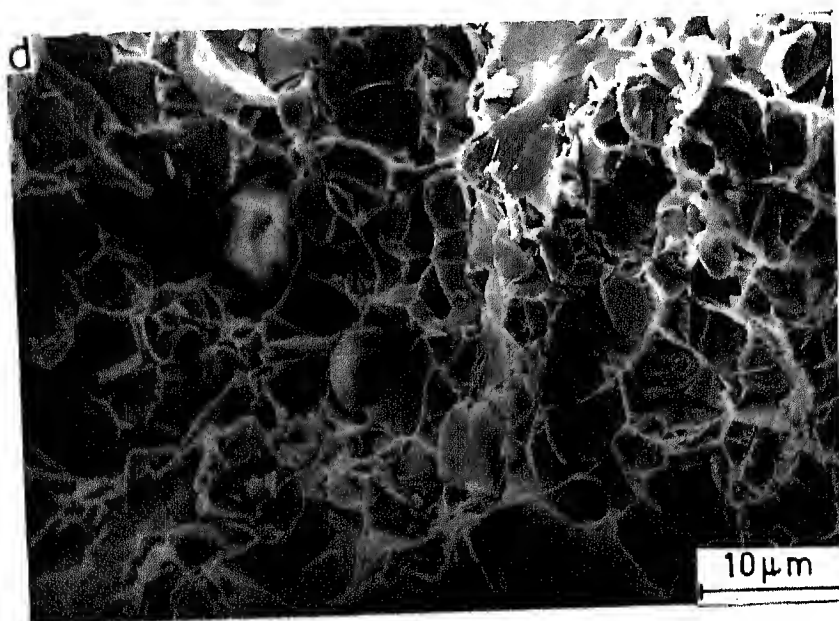
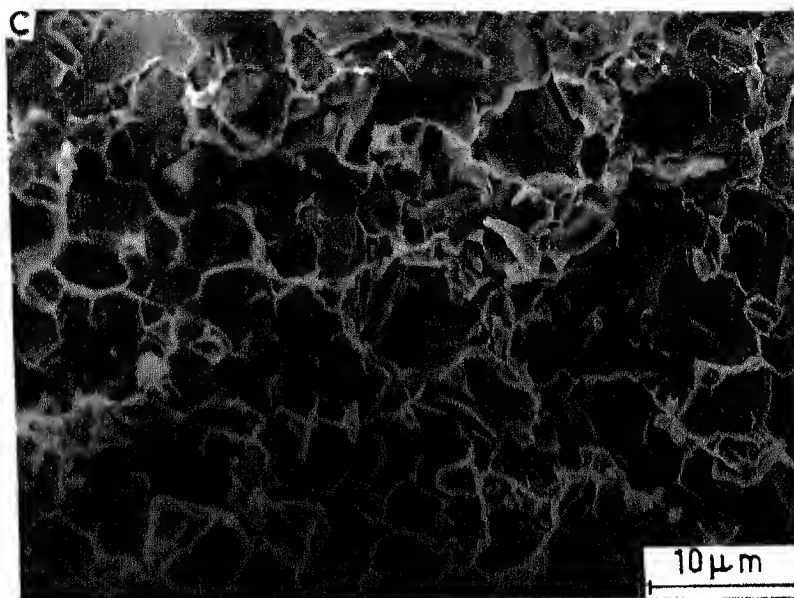
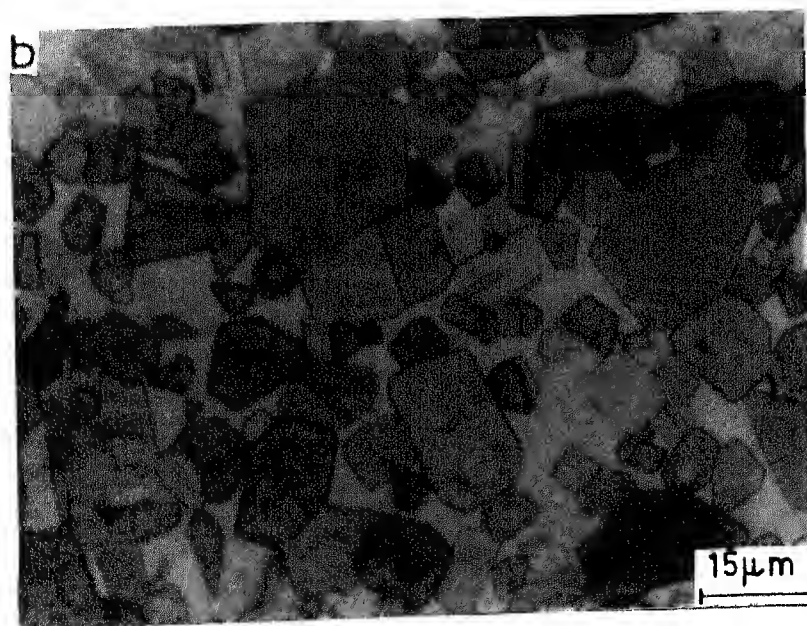
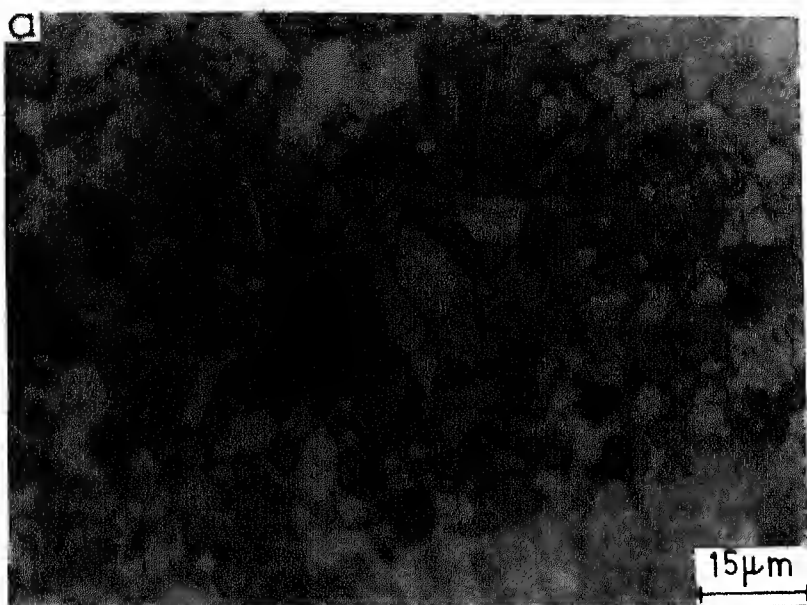


Fig. 3.27 SEM Fractographs of $\text{Mo}_2(\text{Fe}_{0.5}\text{Ni}_{0.5})\text{B}_2$ and its based cermets prepared through the MoB route (Sintering temperature 1350°C) :

- (a) $\text{Mo}_2(\text{Fe}_{0.5}\text{Ni}_{0.5})\text{B}_2$
- (b) $\text{Mo}_2(\text{Fe}_{0.5}\text{Ni}_{0.5})\text{B}_2$ - 11.51 vol.% $\gamma(\text{FeNi})$
- (c) $\text{Mo}_2(\text{Fe}_{0.5}\text{Ni}_{0.5})\text{B}_2$ - 24.41 vol.% $\gamma(\text{FeNi})$
- (d) $\text{Mo}_2(\text{Fe}_{0.5}\text{Ni}_{0.5})\text{B}_2$ - 37.22 vol.% $\gamma(\text{FeNi})$



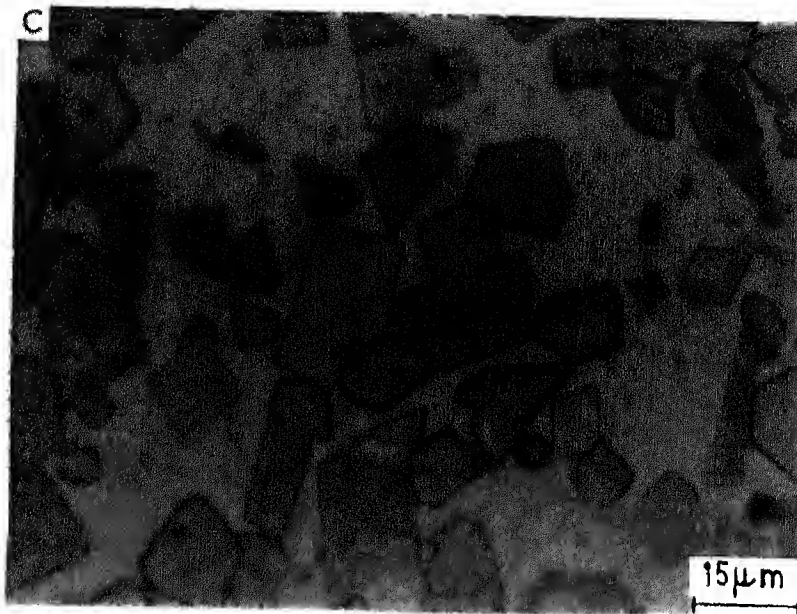


Fig. 3.28 Optical microstructures of Mo_2NiB_2 and its based cermets prepared through the MoB route (Sintering temperature 1350°C) :

- (a) Mo_2NiB_2
- (b) Mo_2NiB_2 - 10.88 vol.% Ni
- (c) Mo_2NiB_2 - 23.74 vol.% Ni

with the increase in nickel binder content. The microstructures also contain some spherical isolated pores.

Fig. 3.29 (a) shows the SEM fractograph of the straight Mo_2NiB_2 boride. The fractograph reveals dimple brittle failure with quasicleavage twinned plate and elongated facets. Large number of cracks are quite predominant near the grain boundary region. The fractographs also consist of river like facets near the void region.

Nickel bonded cermet containing 10.88 vol.% binder also shows brittle fracture. The fractured surface mainly consists of large number of quasicleavage plate and elongated facets with small number of dimples.

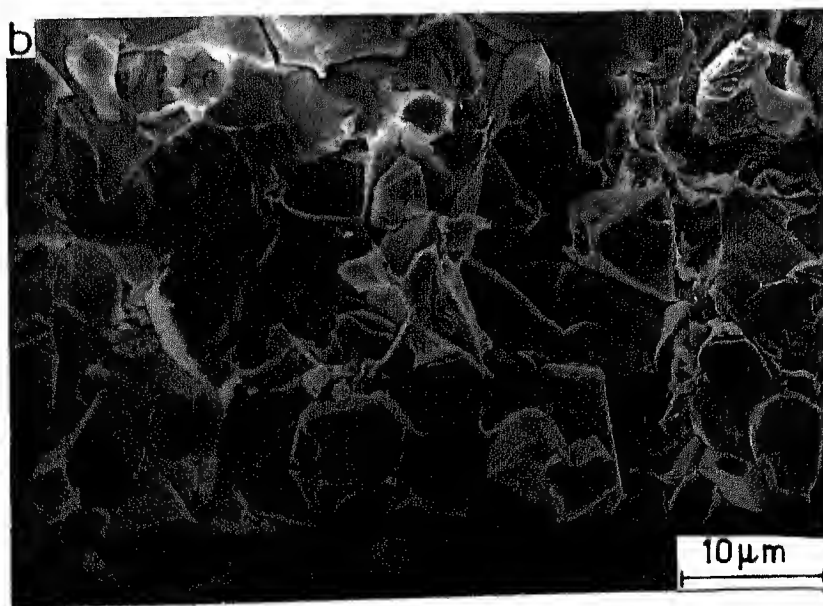
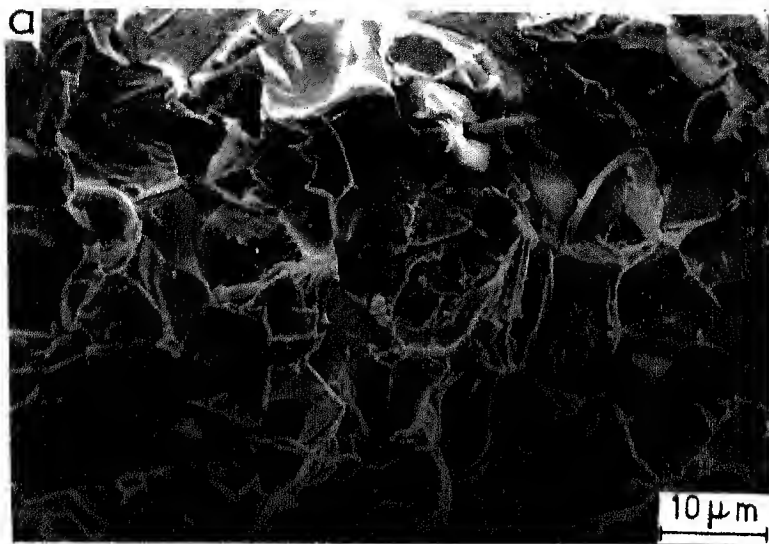
3.13 QUANTITATIVE METALLOGRAPHY

3.13.1 Boride Grain Mean Linear Intercept (\bar{l}_α)

The relationship between the boride grain mean linear intercept and binder content of $\text{Mo}_2\text{Fe}(\text{Ni})\text{B}_2$ -Fe(Ni) cermets is shown in the Fig 3.30.

It is evident from the above figure that the α Fe and $\gamma(\text{FeNi})$ bonded cermets do not follow a systematic variation in \bar{l}_α with the increase in binder content. Mo_2FeB_2 - α Fe cermets exhibit an increase in \bar{l}_α in the initial stage. For greater than 12.43 vol % α Fe binder addition it reduces. $\gamma(\text{FeNi})$ bonded cermets show a rapid decrease in \bar{l}_α initially, in the later stage it regains the earlier grain size. Mo_2NiB_2 -Ni cermets give rise to a rapid increase in \bar{l}_α with the increase in nickel binder content.

Cermets containing 12.43 vol.% α Fe, 11.51 vol % $\gamma(\text{FeNi})$,



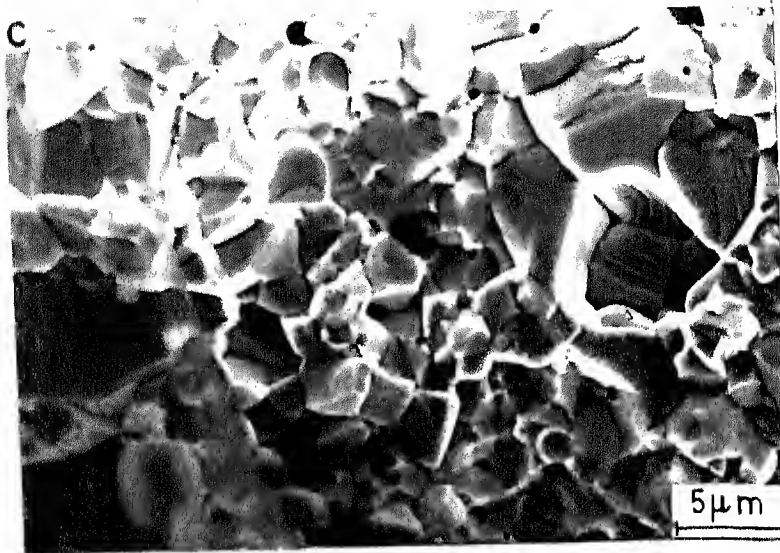


Fig. 3.29 SEM Fractographs of Mo_2NiB_2 and its based cermets prepared through the MoB route (Sintering temperature 350°C).

- (a) Mo_2NiB_2
- (b) Mo_2NiB_2 - 10.88 vol. %
- (c) Mo_2NiB_2 - 23.74 vol. %

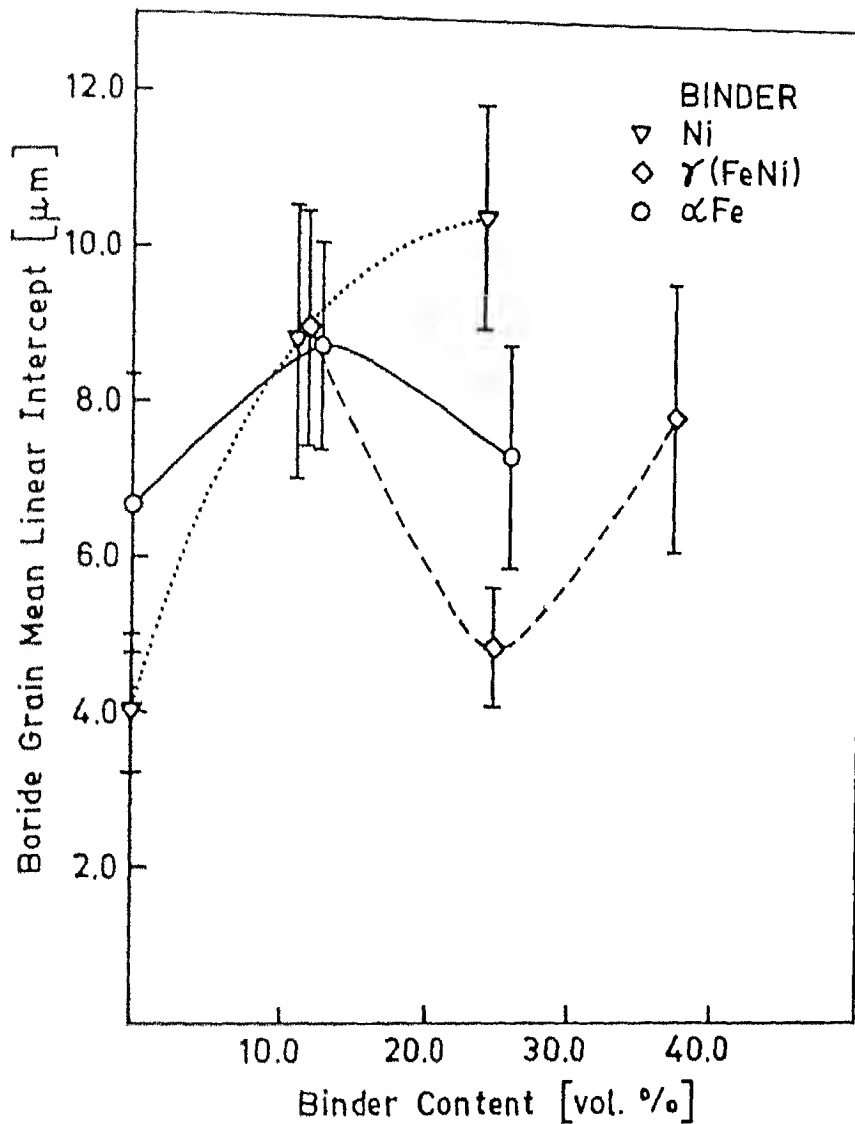


Fig. 3.30. Variation of boride grain mean intercept vs binder content of $\text{Mo}_2\text{Fe}(\text{Ni})\text{B}_2 - \text{Fe}(\text{Ni})$ cermets.

23.74 vol % Ni binders respectively reflect maximum boride grain size values such that the sequence is in the order $\text{Ni} > \gamma (\text{FeNi}) > \alpha \text{ Fe}$.

3.13.2 Binder Mean Free Path (\bar{l}_β)

Binder mean free path of $\text{Mo}_2\text{Fe}(\text{Ni})\text{B}_2$ -Fe(Ni) cermets in general increases with the increase in binder content [Fig. 3.31].

The variation of mean free path of binder phase for various cermets is such that it is similar in case of Ni and $\gamma(\text{FeNi})$ binders, while in case of $\alpha \text{ Fe}$ the change is rather slow in the initial increment in binder level from 12.43 vol.% to 25.62 vol.%.

3.13.3 Boride Phase Contiguity

Boride phase contiguity of $\text{Mo}_2\text{Fe}(\text{Ni})\text{B}_2$ -Fe(Ni) cermets in general decreases with the increase in binder content (Fig. 3.32).

Cermets containing 25.62 vol.% $\alpha \text{ Fe}$ and 23.74 vol.% Ni binders exhibit 40% and 56% decrease in boride phase contiguity. Where as, 37.22 vol.% $\gamma(\text{FeNi})$ bonded cermet shows a maximum decrease of 63% with respect to the straight boride.

The characteristic feature is that the decreasing trend in the boride phase contiguity follows the order of $\text{Ni} < \gamma(\text{FeNi}) < \alpha \text{ Fe}$.

3.14 X-RAY DIFFRACTION ANALYSIS

The presence of various hard and binder phases in $\text{Mo}_2\text{Fe}(\text{Ni})\text{B}_2$ -Fe(Ni) cermets have been confirmed from the X-ray diffraction studies.

Mo_2FeB_2 - $\alpha \text{ Fe}$ cermets have Mo_2FeB_2 hard ternary boride and

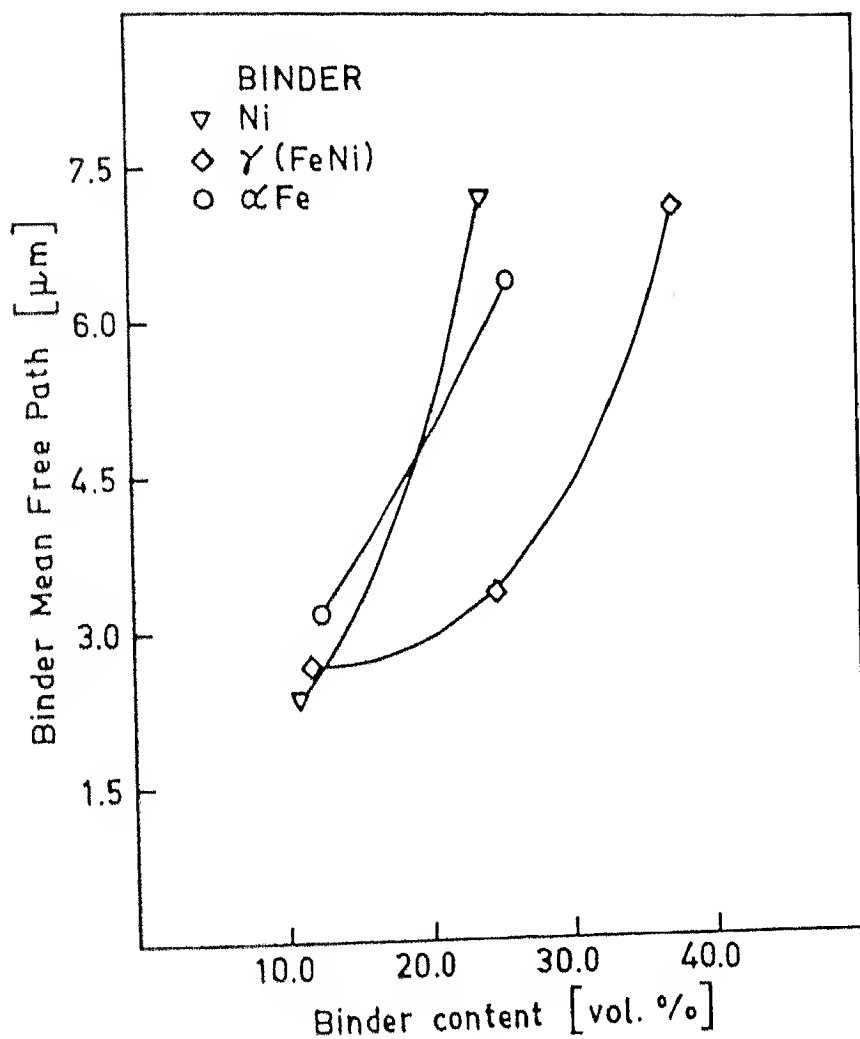


Fig. 3.31. Variation of binder mean free path vs binder content of $\text{Mo}_2\text{Fe}(\text{Ni})\text{B}_2 - \text{Fe}(\text{Ni})$ cermets.

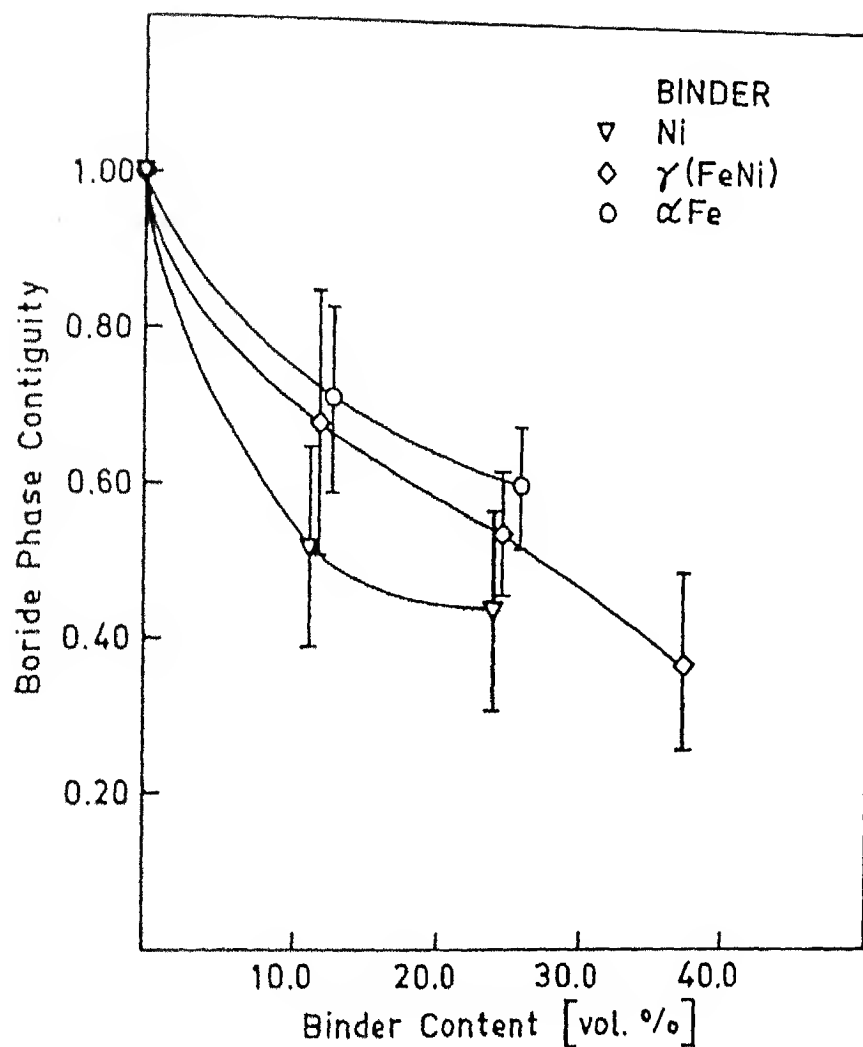


Fig. 3.32. Variation of boride phase contiguity vs binder content of $\text{Mo}_2\text{Fe}(\text{Ni})\text{B}_2\text{-Fe}(\text{Ni})$ cermets.

α -iron binder phases. Mo_2FeB_2 possesses tetragonal lattice configuration. The structure type is isotype with that of U_3Si_2 superstructure. α -iron binder has the BCC crystal structure. The structure type is isotype with that of W. The variation in lattice parameters of Mo_2FeB_2 and α Fe phases is shown in the Fig. 3.33. It is evident that lattice parameters of the Mo_2FeB_2 hard phase do not change significantly with the increase in α -iron binder content. The lattice parameter of the α -iron binder remains constant in all Mo_2FeB_2 - α Fe cermets.

$\text{Mo}_2(\text{Fe}_{0.5}\text{Ni}_{0.5})\text{B}_2$ has tetragonal crystal structure. The structure type is isotype with that of U_3Si_2 superstructure. $\gamma(\text{FeNi})$ binder exhibits FCC crystal structure. The structure type is isotype with that of AuCu. The variation in lattice parameters of $\text{Mo}_2(\text{Fe}_{0.5}\text{Ni}_{0.5})\text{B}_2$ and $\gamma(\text{FeNi})$ phases with the binder content is shown in the Fig. 3.34. It is interesting to note that the lattice parameters of these phases do not vary significantly with the increase in binder content.

Mo_2NiB_2 possesses an orthorhombic lattice configuration. The structure type is isotype with that of W_2CoB_2 superstructure. Nickel has fcc crystal structure. The structure type is isotype with that of copper. The variation in lattice parameters of Mo_2NiB_2 and nickel with the binder content is shown in the Fig. 3.35.

It is interesting to note that unlike other systems in this case, there is detectable increase in lattice parameter of both hard as well as binder phases with the increase in the binder content. This is evident, as the error in measurement for all

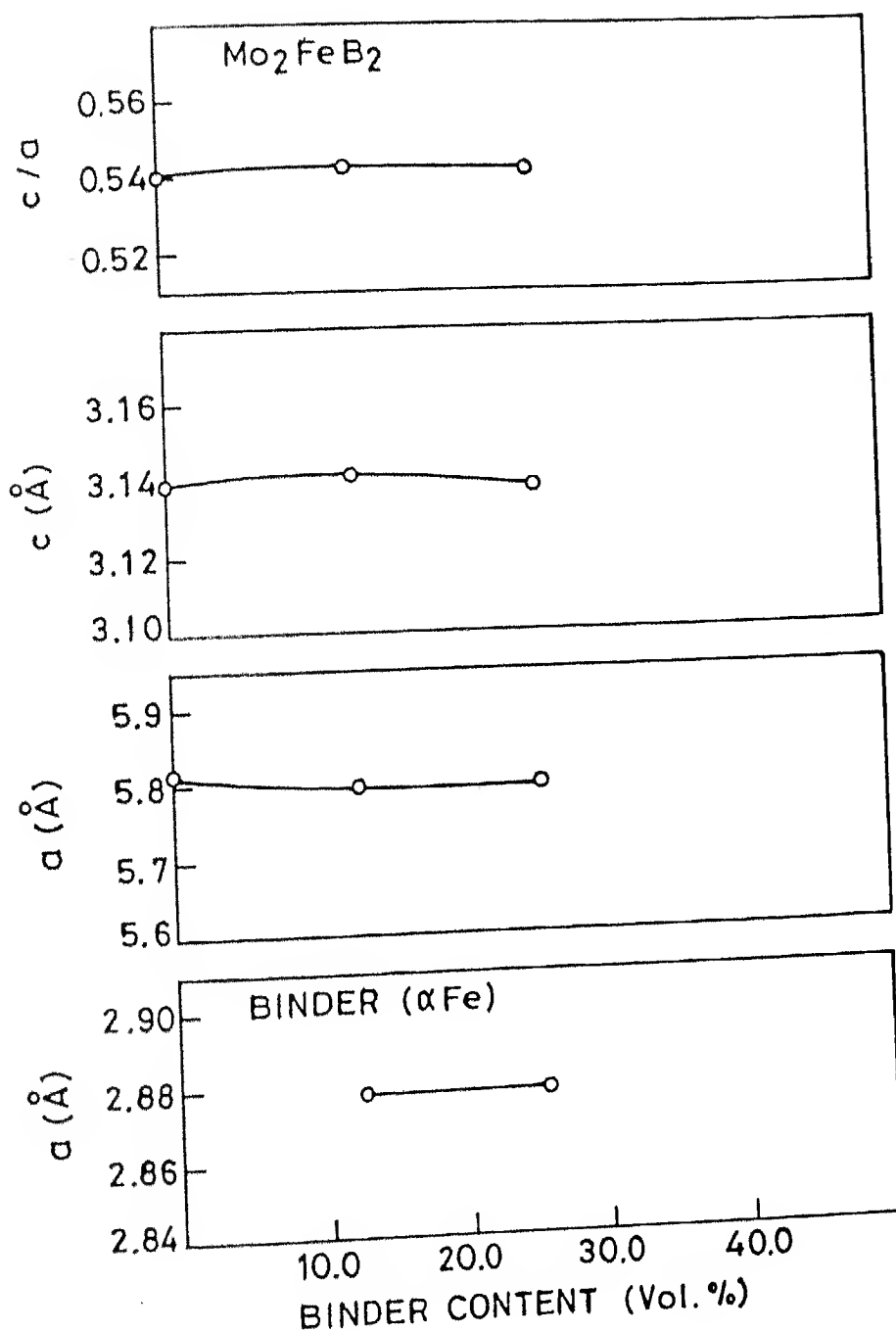


Fig. 3.33 Lattice parameter variation of hard and binder phases in Mo₂FeB₂-αFe cermets prepared through the MoB route and sintered at 1350°C.

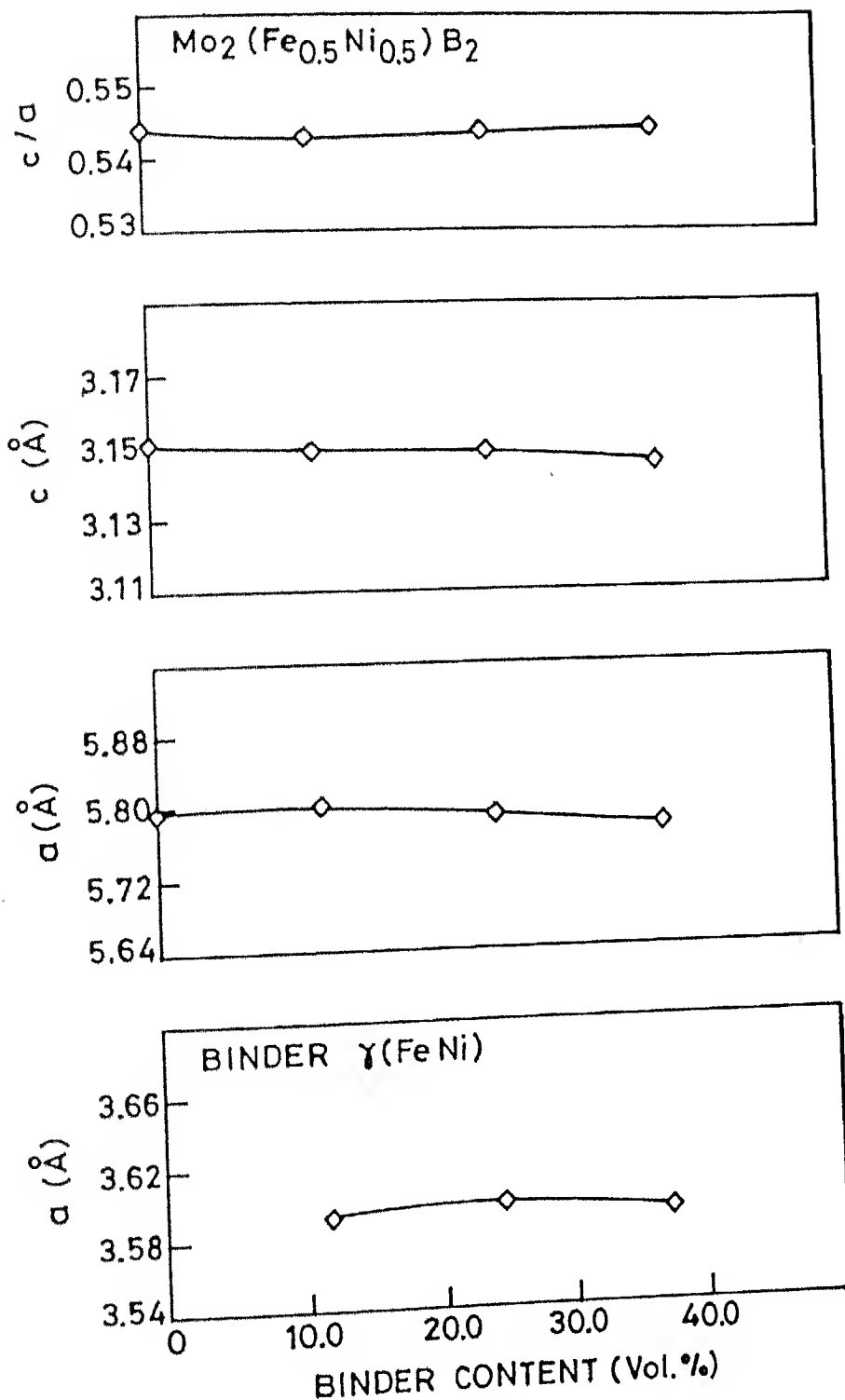


Fig. 3.34 Lattice parameter variation of hard and binder phases in Mo₂(Fe_{0.5}Ni_{0.5})B₂-γ(FeNi) cermet^s prepared through the MoB route and sintered at 1350°C.

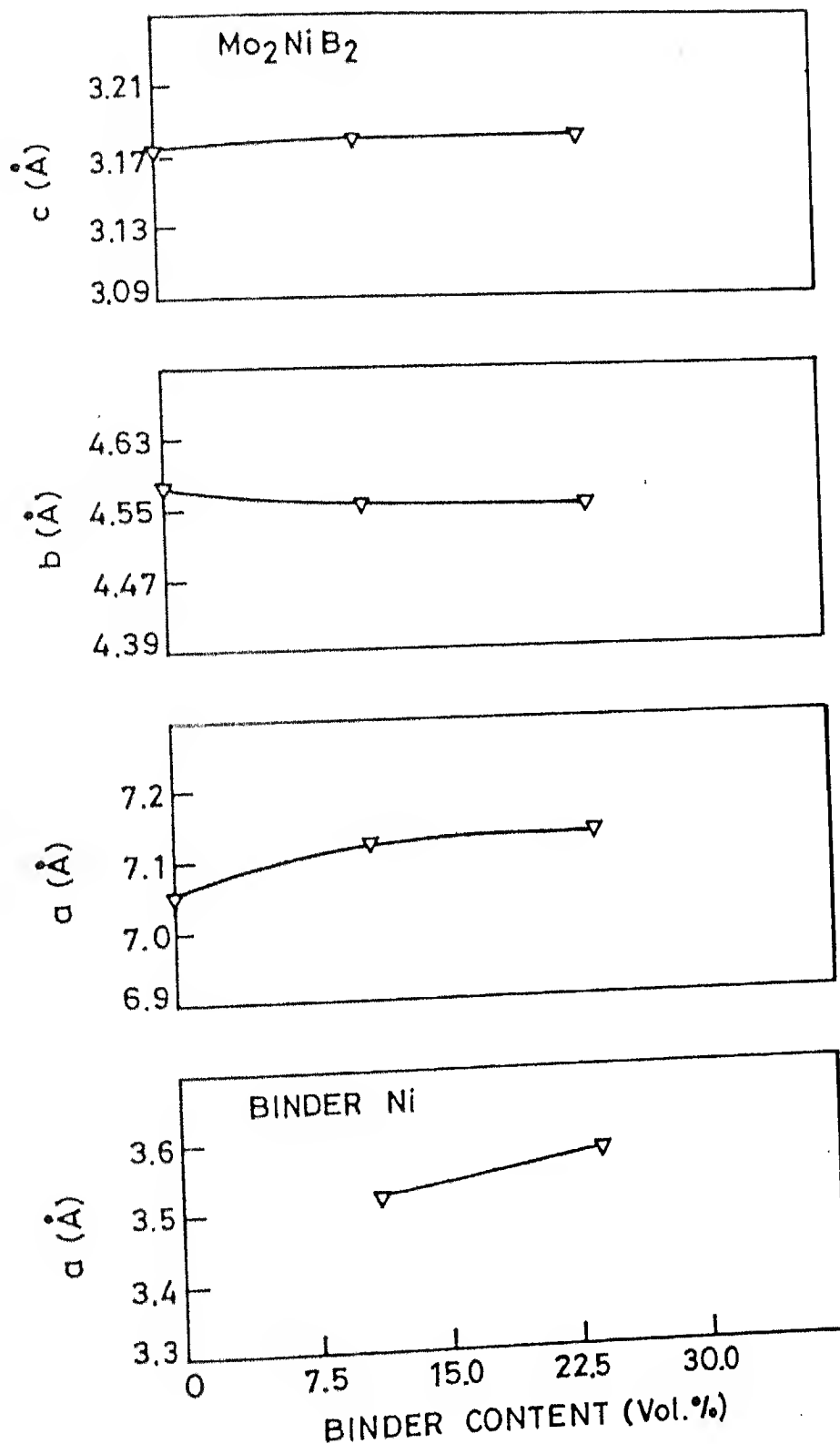


Fig. 3.35 Lattice parameter variation of hard and binder phases in Mo₂NiB₂-Ni cermets prepared through the MoB route and sintered at 1350°C .

these three systems are of the same order.

Some of the x-ray results are given in Appendix.

3.15 SATURATION MAGNETIC FLUX DENSITY

$\text{Mo}_2\text{Fe}(\text{Ni})\text{B}_2$ -Fe(Ni) cermets exhibit in general an increase in saturation magnetic flux density with the increase in the binder content (Fig. 3.36).

In case of Mo_2FeB_2 - α Fe cermets saturation magnetic flux density increases rapidly from 12.43 vol.% α -iron binder addition to 156% with the increase in binder content to 25.62 vol.% α -iron.

$\text{Mo}_2(\text{Fe}_{0.5}\text{Ni}_{0.5})\text{B}_2$ - $\gamma(\text{FeNi})$ cermets show almost a linear relationship between the saturation magnetic flux density and the binder content.

The noteworthy feature is that the variation in this property with respect to binder content is more in case of Mo_2FeB_2 - α Fe cermets as compared to cermets containing $\gamma(\text{FeNi})$ binder.

In case of cermets containing nickel as the binder, magnetic measurement could not be made.

3.16 THERMAL SHOCK RESISTANCE

Table 3.5 shows the thermal shock resistance variation of $\text{Mo}_2\text{Fe}(\text{Ni})\text{B}_2$ -Fe(Ni) cermets prepared through the MoB route.

It is evident that Mo_2FeB_2 - α Fe cermets reflect no significant effect of binder addition on thermal shock resistance.

$\text{Mo}_2(\text{Fe}_{0.5}\text{Ni}_{0.5})\text{B}_2$ - $\gamma(\text{FeNi})$ and Mo_2NiB_2 -Ni cermets give rise to quite significant improvement on thermal shock resistance with

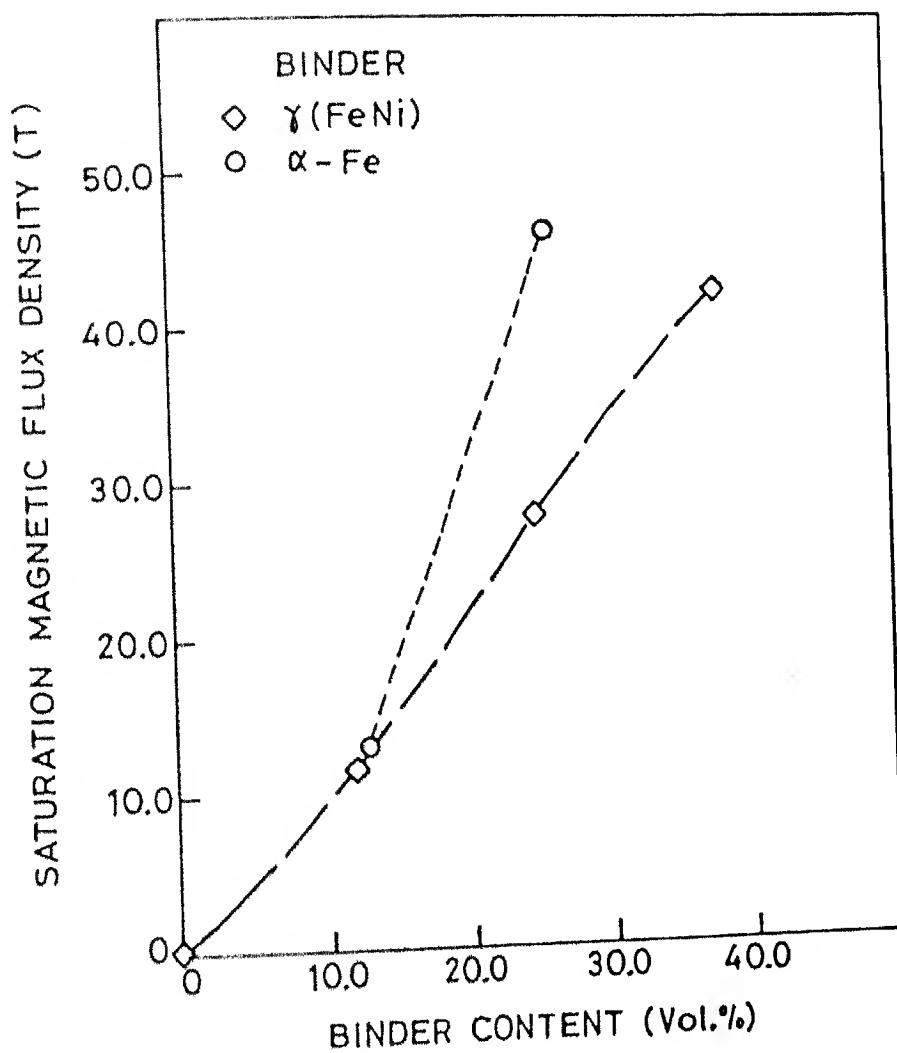


Fig. 336 Saturation magnetic flux density variation of $\text{Mo}_2\text{Fe}(\text{Ni})\text{B}_2\text{-Fe}(\text{Ni})$ cermets prepared through the MoB route and sintered at 1350°C .

the increase in $\gamma(\text{FeNi})$ and nickel binder content.

Table 3.5 : Thermal Shock Resistance (ΔT) of $\text{Mo}_2\text{Fe}(\text{Ni})\text{B}_2\text{-Fe}(\text{Ni})$ cermets prepared through the MoB route

Cermet	Binder Content (Vol.%)	ΔT ($^{\circ}\text{C}$)
$\text{Mo}_2\text{FeB}_2\text{-}\alpha\text{Fe}$	0	< 370
	12.43	< 370
	25.62	< 370
$\text{Mo}_2(\text{Fe}_{0.5}\text{Ni}_{0.5})\text{B}_2\text{-}\gamma(\text{FeNi})$	0	< 765
	11.51	770
	24.41	770
	37.22	770
$\text{Mo}_2\text{NiB}_2\text{-Ni}$	0	< 665
	10.88	770
	23.74	770

3.17 CORROSION WEIGHT LOSS STUDY

Fig. 3.37 shows the corrosion rate of $\text{Mo}_2\text{Fe}(\text{Ni})\text{B}_2\text{-Fe}(\text{Ni})$ cermets in 10 wt.% HCl and 10 wt.% HF solutions respectively.

$\text{Mo}_2\text{FeB}_2\text{-}\alpha\text{Fe}$ cermets, in general, show least corrosion resistance as compared to the other investigated cermets. It is interesting to note that the corrosion resistance follows a trend $\text{Ni} > \gamma(\text{FeNi}) \gg \alpha\text{Fe}$ in either corrosion media.

As regards the effect of binder content on corrosion rate is concerned, it is evident that the rate is minimum in case of 12.43 vol.% αFe and 11.51 vol.% $\gamma(\text{FeNi})$ containing cermets. However, in case of Ni- bonded cermets, the corrosion rate was approximately constant irrespective of the binder content.

Alloy 1,4,8 (~10 vol% Binder); Alloy 2,5,9 (~12 vol% Binder),
Alloy 3,6,10 (~24 vol% Binder); Alloy 7 (37 vol% Binder)

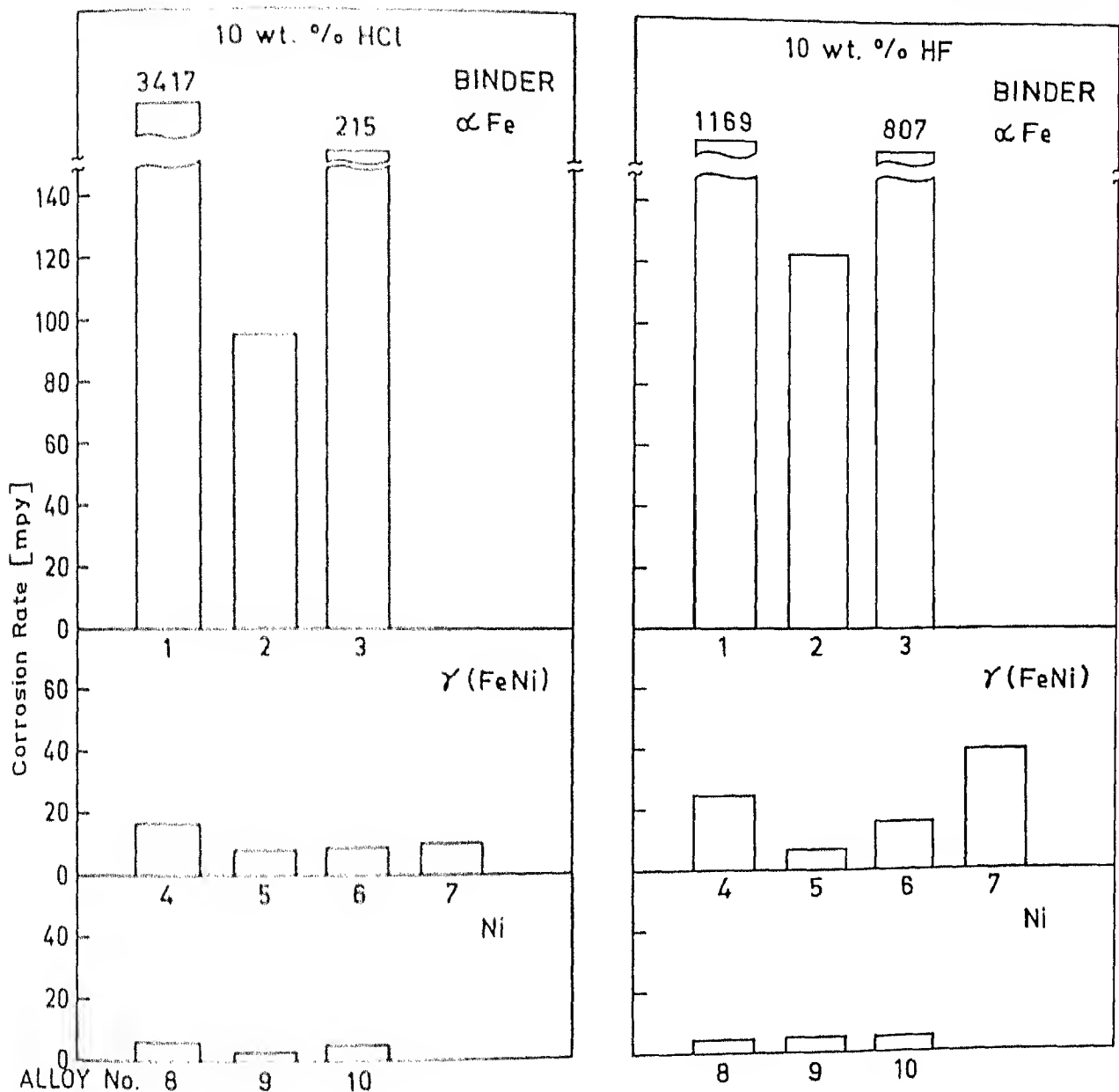


Fig. 3.37. Corrosion rate of $\text{Mo}_2\text{Fe}(\text{Ni})\text{B}_2\text{-Fe}(\text{Ni})$ cermets in 10 wt. % HCl and 10 wt. % HF solutions for 10 hrs respectively.

The noteworthy feature is that $\text{Mo}_2\text{Fe}(\text{Ni})\text{B}_2\text{-Fe}(\text{Ni})$ cermets, in general, exhibit poor corrosion resistance in 10 wt.% HF acid solution as compared to 10 wt.% HCl acid solution, with the exception of Ni-bonded cermets, where the values are in the same range. Another unique feature is that the straight Mo_2FeB_2 corrodes maximum in 10 wt% HCl medium.

CHAPTER IV

DISCUSSION

The results of the present investigations have been discussed in two parts. In the first part the results of sintered properties of Mo_2FeB_2 - αFe cermetes prepared through the elemental and MoB routes are discussed. The second part contains the discussion of the results of sintered properties of $\text{Mo}_2\text{Fe}(\text{Ni})\text{B}_2$ - $\text{Fe}(\text{Ni})$ cermetes prepared through the MoB route.

PART I : Mo_2FeB_2 - αFe CERMETS THROUGH THE ELEMENTAL AND MoB ROUTES

4.1 EFFECT OF BALL MILLING ON AVERAGE PARTICLE SIZE

As it is evident from Table 3.2, the average particle size of ball milled powder premixes, in general, increases with the increase in binder content. This is related to the fact that soft binder surrounding the hard phase impedes the milling efficiency. Literature [21,22] reveals that microhardness of molybdenum (2740 kgf/mm^2) is greater than that of MoB (2350 kgf/mm^2). This appears to be the reason why a more brittle phase i.e. Mo gets milled to a relatively greater extent as compared to the cermetes prepared through the MoB route.

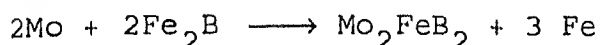
4.2 Densification Behaviour

During reaction sintering starting with powder mixture of binary boride and metal, a ternary boride is formed at the contacting points by solid state diffusion. A quasi-binary liquid phase is formed between the ternary boride particles and the metal phase. This liquid phase promotes densification by liquid phase sintering mechanism.

In case of elemental premix route the steps involved consist of:

- Formation of Fe_2B from elemental Fe and B powders. Fe_2B has 8.82 wt.% boron and a tetragonal lattice. The solubility of boron in iron is negligible (0.02 wt.%), thus promoting the formation of binary boride.

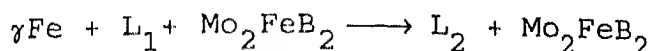
- Formation of Mo_2FeB_2 from Fe_2B and Mo by the solid state reaction:



- Formation of an eutectic liquid L_1 by the reaction between Fe_2B and γFe at 1149°C and 3.8 wt.% B.

Significant differences exist among data reported in the literature. In a review on boriding and diffusion metallizing Chatterjee-Fischer [23] cites the values of 1174°C reported by Massalski [24]. Nowacki and Klimeck [25] quote the reference [26] but report a phase diagram from which one can deduce eutectic temperature as 1157°C . In a critical assessment of previously reported Fe-B phase diagrams [27-29], Chart [30] calculated a temperature 1177°C . A value slightly lower than 1177°C is suggested by Yukinobu et al. [31], who revised the liquidus curve of the Fe-B system on the basis of resistivity measurements in conjugation with X-rays and thermal dilatometric studies. Kneller and Khan [32] in turn reported Fe-B phase diagram with the eutectic temperature 1160°C , determined on the basis of DTA and X-ray diffraction measurements.

■ Formation of another liquid L_2 via the following reaction at 1202°C



It is reported by German et al. [2] that the formation of Mo_2FeB_2 during sintering elemental Fe-B-Mo causes swelling, which occurs above 752°C [11]. The eutectic liquid L_1 exerts a capillary force, due to this capillary action interconnected pores are filled up by this liquid. It helps in particle rearrangement by primary densification between 1092°C - 1142°C [11]. With the rise in temperature $> 1200^\circ\text{C}$ secondary densification of the cermets is effective by dissolution of Mo_2FeB_2 in L_2 resulting in the solution and reprecipitation of Mo_2FeB_2 , a process characterizing the second stage of liquid phase sintering.

It is interesting to note that in case of ternary boride Mo_2FeB_2 there is not much change in sintered porosity after 1250°C and 1300°C sintering, but the porosity level drops significantly at a still higher temperature i.e. 1350°C . This confirms that stable sp^3 configuration of boron atoms in boride is responsible for the presence of covalent bonding and hence poor sinterability at relatively lower temperatures. It is known that elemental boron has $2s^2 2p^1$ configuration of valence electrons, which during formation of crystal attains sp^3 configuration because of $s \rightarrow p$ transition. In case of cermets, however, the situation is at a variance. Here the porosity levels after 1300°C and 1350°C sintering are much in proximity as compared to 1250°C sintering. This is in consonance with the

fact that diffusivity in the melt is high apart from the increased volume fraction of the liquid phase.

In case of MoB route, it is obvious that the porosities of straight Mo_2FeB_2 after any sintering is lower as compared to the elemental route [Fig 3.7], which is associated with faster solid state reaction in the former. However in case of Mo_2FeB_2 - αFe cermets, such enhanced densification is felt more after 1250°C sintering. For other two sintering temperatures viz. 1300°C and 1350°C, the densification was almost independent of the preparation route. This confirms that at elevated temperatures, the attainment of equilibrium was similar in either processing route.

4.3 Mechanical Properties

The results of Vickers hardness, transverse rupture strength and indentation fracture toughness are discussed below.

4.3.1 Vickers Hardness

The attainment of better hardness of sintered Mo_2FeB_2 prepared through the elemental route after 1350°C sintering as compared to that prepared by MoB route (Fig. 3.9) is not correlable with mere densification results (Fig. 3.8). It is possible that various synthesis stages as enumerated earlier are responsible for a better homogeneous ternary phase formation in case of elemental route. Enhanced porosity in this case as compared to MoB route is attributed to swelling as suggested by German et al. [10].

In case of cermets it is evident that MoB route gives rise to higher hardness values as compared to those obtained through

elemental route, particularly for 1250°C sintering. This is correlable with the sintered porosity which is lower in the former preparation route. However after a still elevated temperature sintering i.e. 1300°C and 1350°C, the drop in hardness in high volume fraction binder (25.62 vol.%) cermets (MoB route) could be attributed to the ease of coalescence among boride grains by the Ostwald ripening process, thus promoting boride grain coarsening.

4.3.2 Transverse Rupture Strength (TRS)

TRS variation with respect to binder content (Fig. 3.10) can be directly correlated with the total sintered porosity variation, such that an increase in porosity decreases the rupture strength. However, with respect to sintering temperature, the cermets unlike ternary Mo_2FeB_2 boride show greater TRS values after 1300°C sintering than after 1350°C. Since TRS values have large scatter for brittle solids, the above conclusions can not be confirmatory. However, one thing emerges clearly that for better transverse rupture strength, the sintering temperature must be greater than 1250°C.

SEM fractography results (Fig. 3.13 a & b) showing similar fracture mode in straight Mo_2FeB_2 and cermets (Mo_2FeB_2 -12.43 vol.%Fe) is attributed to the fact that a relatively high porosity after 1250°C sintering in the cermet is sufficient to mask the ductilising role of the metal binder.

4.3.3 Indentation Fracture Toughness (Kc)

Indentation fracture toughness variation of 1350°C sintered cermets demonstrates the toughening effect of metal binder, such

that there is a 100% increase in the value for 25.62 vol.% α Fe binder cermet as compared to the straight Mo_2FeB_2 boride. Such a quantitative change is also seen in case of TRS variation.

4.4 SATURATION MAGNETIC FLUX DENSITY

As apparent from the results (Fig. 3.15), the saturation magnetic flux density in case of Mo_2FeB_2 - α Fe cermets prepared through the elemental and MoB route follows an increasing linear trend with the increase in binder content. The results are in consonance with the fact that a greater volume fraction of ferromagnetic component i.e. α -Fe increases the saturation magnetic flux density values. Apart from this the porosity also plays its role as it increases the resistivity and also decreases the eddy current loss. This is the reason why lower volume fraction binder containing cermets exhibit rather low magnetic flux densities.

Mo_2FeB_2 - α Fe cermets prepared through the MoB route exhibit slight increase in the saturation magnetic flux density as compared to the elemental route. This appears due to an increase in grain size. In this case magnetic domains are less hindered by grain boundary walls as compared to the cermets prepared through the elemental route.

4.5 CORROSION WEIGHT LOSS STUDY

From the results it is evident that the straight Mo_2FeB_2 boride exhibits least corrosion resistance in 10 wt.% HCl solution. The maximum porosity level in straight Mo_2FeB_2 boride is attributed to maximum exposed effective surface area to the corrosive medium, and hence more corrosion.

minimum porosity level, thus exposing minimum effective surface area. This makes it least corrosion resistant. Literature [18] reports that the corrosion potential of Mo_2FeB_2 is approximately 0 mV to 50 mV and with that of α -iron binder is -450 mV to - 280 mV with respect to the Ag/AgCl electrode in 10 wt.% HCl. Although the α -iron binder corrodes faster as compared to Mo_2FeB_2 phase the better corrosion resistance in case of cermets may be correlated with better densification.

Cermet containing 25.62 vol.% α -iron binder exhibits less corrosion resistance to that of 12.43 vol.% α -iron bonded cermet. This is due to the higher proportion of iron which is more anodic in nature.

Corrosion resistance of the straight Mo_2FeB_2 in 10 wt.% HF is superior as compared to in 10 wt.% HCl solution, which may be attributed to the increase in corrosion potential of Mo_2FeB_2 phase. The poor corrosion resistance of Mo_2FeB_2 - αFe cermets in 10 wt.% HF solution may be attributed to the decrease in corrosion potential of α -iron binder.

PART II : $\text{Mo}_2\text{Fe}(\text{Ni})\text{B}_2$ -Fe(Ni) CERMETS THROUGH THE MoB ROUTE

4.6 EFFECT OF BALL MILLING ON AVERAGE PARTICLE SIZE

The average particle size of ball milled powder premixes of $\text{Mo}_2\text{Fe}(\text{Ni})\text{B}_2$ -Fe(Ni) cermets, in general, increases with the increase in Fe(Ni) binder content (Table 3.4). The α -iron and nickel binder phases possess 30-40% and 40% ductility with hardness of 82 and 85 BHN respectively [33], whereas, the hard and brittle MoB phase possesses 2350 kgf/mm² microhardness [34].

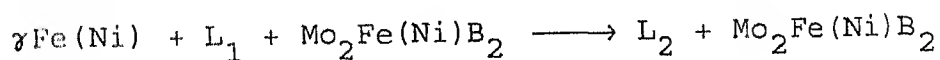
During ball milling due to cascading action between WC balls, bowl wall and among powder particles multigravity forces arises. Due to such action, the hard and brittle MoB powder particles are fractured to a relatively greater extent as compared to the ductile binder powder particles. Subsequently these fractured hard powder particles impinge over the softer Fe(Ni) binder powder particles which surround the hard phase. This infers that the ductilising effect of the soft Fe(Ni) binder phase decelerates the milling efficiency. On the other hand with the increase in vol.% of hard and brittle MoB phase the fineness of ball milled powder premixes increases.

4.7 DENSIFICATION BEHAVIOUR AND MICROSTRUCTURE

During reaction sintering starting with powder mixture of MoB binary boride and metal binder (Fe/Ni), a ternary boride is formed at the contacting points. A quasi-binary liquid phase is formed between the ternary boride ($\text{Mo}_2\text{Fe}(\text{Ni})\text{B}_2$) particles and the metal binder phase. This liquid phase so formed promotes densification through the liquid phase sintering mechanism.

During synthesis of boride based cermets following steps can be considered:

- Formation of $\text{Mo}_2\text{Fe}(\text{Ni})\text{B}_2$ from MoB and Fe(Ni) by solid state reaction.
- Formation of liquid phase, which helps in particle rearrangement during densification by the reaction.



The temperature at which this reaction takes place is dependent on the type of binder. In case of iron binder the

temperature is 1202°C [11], while in case of nickel it is above 955°C [13]. This indicates that after sintering at 1350°C , densification in nickel bonded cermets should be better than that in iron bonded ones. As a matter of fact this is evidenced by better Ostwald ripening in case of nickel bonded cermets. However, this is not reflected by the sintered porosity variation (Fig. 3.21). One of the probable reasons appears the fact that the calculation of theoretical densities assuming the rule of mixture in such reactive systems is on erroneous assumption. Another supporting feature for the better sinterability in case of nickel bonded cermets can be guessed from the fact that the contact melting temperature of $\text{MoB}_2\text{-Ni}$ (1000°C) is lower than in case of $\text{MoB}_2\text{-Fe}$ (1100°C) [35].

Our observation that for any fixed binder level, Ni-bonded cermets show maximum grain coarsening (Fig. 3.30), suggests that the dissolution kinetics in such binder is fast. This appears to be reasonable from the fact that the maximum solubility of refractory metal molybdenum in nickel (40%) is more than in α -iron (30%) [36]. An increase in the hard phase boride grain coarsening with increase in the binder volume fraction in any cermet confirms better homogeneous milling in such cases, which causes the contiguity of hard ceramic phase to get lowered. Such an event will further accentuate dissolution and reprecipitation stage of liquid phase sintering. The presence of some debonded rounded particles in the SEM fractographs (Fig. 3.29) independent of the type of binder and its content, is not very clear. However, it may be attributed to some of the original MoB

particles, which could not perhaps get fully reacted. Such possibility exists, as the transition metal binder melt does not fully wet MoB [37], with the natural consequence of the formation of void envelope.

The variation in sintered porosity in case of straight ternary boride is opposite to that for its based cermet. The porosity in the former decreases in the sequence $\text{Mo}_2\text{FeB}_2 \rightarrow \text{Mo}_2\text{NiB}_2 \rightarrow \text{Mo}_2(\text{Fe}_{0.5}\text{Ni}_{0.5})\text{B}_2$. The maximum sintered porosity in case of Mo_2FeB_2 appear to be related to the possibility of oxygen impurity in iron powder, whose oxide (FeO) is much stabler than NiO [35]. However, the oxide level was not that appreciable to get detected by the present X-ray studies. In case of cermets, unlike transient eutectic liquid phase ($\text{M}_2\text{B-M}$) formation during synthesis of ternary borides, the binder melt is persistent one, which assists in densification throughout the sintering cycle.

From the wettability point of view there is not much difference in the contact angles of VI-th group metal borides with either iron or nickel melt [37]. However, it is also reported that the intensity of wetting of a refractory boride increases in the order $\text{Fe} \rightarrow \text{Co} \rightarrow \text{Ni}$ [39]. The lowest values of sintered porosity in case of Mo_2FeB_2 - α Fe as compared to Mo_2NiB_2 -Ni cermets may be attributed to the above fact and also to a sudden drop in surface tension of ferrous melt containing oxygen impurity, if any, as compared to the similar nickel melt [40].

4.8 MECHANICAL PROPERTIES

The results of various investigated mechanical properties such as Vickers hardness, transverse rupture strength and indentation fracture toughness are discussed below:

4.8.1 Vickers Hardness

As evident from Fig. 3.23, the cermets with iron and γ (FeNi) binders show a presence of hardness peak. On the other hand in cermets containing nickel, a uniform fall in hardness with increase in binder volume fraction is noticed. As mentioned previously, nickel containing cermets show maximum sintered density, and any hardness fall is therefore attributed to the presence of the relatively soft binder. However in other two types of binders, the porosity level in boride, particularly in Mo_2FeB_2 , is pretty high and any increase in hardness with the initial increase in binder content can be attributed to densification. The fall in hardness after 12 vol.% binder in such cases is due to the softening effect similar in case of nickel. As the hardness difference in iron (82 BHN) and nickel (85 BHN) is not much, it can be concluded that only parameter which contributes in the sintered hardness is the sintered porosity.

4.8.2 Transverse Rupture Strength (TRS) and Indentation Fracture Toughness (Kc)

The improvement in the TRS and fracture toughness of cermets with increase in binder content irrespective of the type of binder can be justified by two reasons. A better densification with increase in the binder volume fraction and the relatively larger proportion of soft binder contribute in enhancing the

strength of the cermets. It is interesting that TRS of the cermets decreases in the sequence $\text{Ni} \rightarrow \gamma(\text{FeNi}) \rightarrow \alpha \text{ Fe binder}$, which is also generally similar in case of fracture toughness. It is worth noting that the transverse rupture strength of a Mo_2B_5 based cermet bonded with 20 vol.% permalloy (600 MPa), as reported by Alfintseva et al. [41], is in proximity of our data for cermet bonded with $\gamma(\text{FeNi})$ (750MPa).

It is worth noting that the ultimate tensile strength of nickel (310 MPa) is greater to that of iron (193-276 MPa) [42]. In addition, the % elongation of the former is somewhat higher than the latter. This suffices to conclude that the transverse rupture strength and fracture toughness of the $\text{Mo}_2\text{NiB}_2\text{-Ni}$ cermets in principle, should be greater than the $\text{Mo}_2\text{FeB}_2\text{-}\alpha\text{Fe}$ cermets. As a matter of fact, this has been experimentally confirmed presently. FCC nickel is known to be responsive to a large number of slip systems during plastic deformation as compared to solid solution strengthened Fe-Ni binary alloy.

Literature [43] confirms better strength of Fe-Ni alloy as compared to straight nickel. However, such a feature is not suggested from the present TRS variation (Fig. 3.24), where the fall in TRS is in the sequence $\text{Ni} \rightarrow \gamma(\text{FeNi}) \rightarrow \alpha\text{Fe}$. This can be related with the probable segregation of intermetallics around the stacking faults in Fe-Ni alloy, thus lowering the energy. Such a feature of solute segregation was noticed by Howie and Swann [44].

With the difficulty in obtaining equilibrium conditions below about 400°C for Fe-Ni alloys containing more than 30%

nickel, it is safely assumed that at room temperature the iron-nickel is in austenitic (FCC) phase. This has been confirmed by present X-ray studies (Fig. 3.34).

4.9 SATURATION MAGNETIC FLUX DENSITY

It is evident that all the binders used presently in the cermets are ferromagnetic which have positive exchange energy. It is known that in condensed state the spin dipole magnetic moment for iron and nickel are 2.2 and 0.6 Bohr magnetons respectively [45], i.e. former about four times greater than the latter. This appears to control the end magnetic property of the investigated cermets, such that iron bonded ones exhibit higher saturation magnetic flux density values than the γ (FeNi) bonded ones. In the weakly ferromagnetic nickel bonded cermets no such measurements could be made. Another interesting feature is that the gap in the flux density becomes wider with increase in the binder content after 12 vol%. The picture in cermet is, however, much more complex, where in ternary borides transition metal atoms (Mo, Fe, Ni) are associated with nontransition metal atom (B). The latter group atoms are characterized by a potential which is deeper than that of a transition element atom for s and p states, the potential is practically equivalent so that of a vacancy for d-states [46].

4.10 THERMAL SHOCK RESISTANCE

Thermal shock in cermets is of very wide significance in most applications involving high temperatures. The thermal shock results in differential temperature throughout the body, leading to the generation of strains and stresses which may cause

cracking and failures. In general, cracking will be initiated when the maximum tensile thermal stress in the material reaches the fracture stress as measured under conditions appropriate to the thermal shock in terms of temperature, environment, state of stress and direction of stress. The critical parameters are, therefore, the heat transfer coefficient between the material and surrounding environment and the thermal conductivity of the material. The different level of porosity in the sintered cermets would also have an effect on the thermal conductivity. Our results, however, indicate that the thermal shock resistance of the cermets is independent of the binder content. This anomaly appears due to the lack in sensitivity in the measurements more than anything else.

4.11 CORROSION WEIGHT LOSS STUDY

The results of corrosion weight loss study of Mo_2FeB_2 - αFe cermets in 10 wt% HCl and 10 wt % HF solutions have been discussed in section 3.17.

The straight $\text{Mo}_2(\text{Fe}_{0.5}\text{Ni}_{0.5})\text{B}_2$ boride exhibits higher corrosion potential in 10 wt% HCl as compared to in 10 wt % HF solution. The difference in corrosion potential between $\text{Mo}_2(\text{Fe}_{0.5}\text{Ni}_{0.5})\text{B}_2$ and $\gamma(\text{FeNi})$ phases is not much in 10 wt% HCl solution, whereas in 10 wt% HF the difference in corrosion potential is quite significant. This gives rise to poor corrosion resistance in higher $\gamma(\text{FeNi})$ bonded cermets.

Mo_2NiB_2 -Ni cermets exhibit maximum corrosion resistance in 10 wt% HF. This may be attributed to the fact that the difference in corrosion potential between Ni and Mo_2NiB_2 phase is

almost negligible. Whereas in 10 wt% HCl solution the change in corrosion potential appears to be appreciable. The corrosion potential of the straight borides increases in the order $\text{Mo}_2\text{FeB}_2 \longrightarrow \text{Mo}_2(\text{Fe}_{0.5}\text{Ni}_{0.5})\text{B}_2 \longrightarrow \text{Mo}_2\text{NiB}_2$. Cermets binder corrosion potential also increases in the order $\alpha\text{Fe} \longrightarrow \gamma(\text{FeNi}) \longrightarrow \text{Ni}$ which is attributed to superior corrosion resistance of Mo_2NiB_2 -Ni cermets in either corrosive medium.

4.12 ELECTRONIC APPROACH TO BORIDE BASED CERMETS

In such type of inorganic cermets the constituents pertain to transition metals (Mo, Fe, Ni) and a nonmetal (B). These elements are characterized as d and sp type elements according to their valence electron configuration.

Samsonov and Upadhyaya [47] have elaborately discussed the role of configuration model in obtaining various high temperature materials. The essence of this model is that the valency of the individual atoms while being grouped in the condensed state, are divided into localized and nonlocalized parts. The localized part of valence electrons forms a configuration of spectrum in which maximum statistical weights are possessed by most stable configuration. These are responsible for a minimum store of free energy. Such configurations are d^5 , d^{10} and d^0 for the transition metals and s^2p^6 and quasistable sp^3 configuration for the sp elements. The maximum localization results in the highest strength of the crystal lattice and also the maximum sharing of the directional covalent bonds in compounds like borides. The localization must therefore be reviewed in relation to M-M and M-B bonds, the ratio of which governs the properties of th

material.

One of the most important tendencies in the electronic structure of boron is the formation of sp^3 configuration according to the scheme [48]



In metallic borides the transformation of sp^2 configuration can happen also in sp^3 configuration with the release of two electrons which are not bound in sp configuration.

Wettability is an important aspect for the development of cermets, which has been discussed by Upadhyaya [49] in details. According to him following conclusions can be drawn.

- 1 For the same transition metal borides wetting angle, in general, increases with increase in the period number of the molten metal.
2. For IVth group transition metal borides in case of iron group melts, the wettability increases in the order $Fe \rightarrow Co \rightarrow Ni$, while for Vth and VIth group borides the reverse is true. This infers that for higher statistical weight of sp^3 configuration, the energetic stability of transition metals must also be high for better wettability.

In the present investigation it has been observed that mechanical properties for example transverse rupture strength and indentation fracture toughness of $Mo_2Fe(Ni)B_2-Fe(Ni)$ cermets decrease in the sequence $Ni \rightarrow \gamma(FeNi) \rightarrow \alpha Fe$. This shows that the total bond strength in nickel containing cermets is highest.

Since the statistical weight of d^{10} configuration fo

Ni(88%) is higher than that of Fe(46%) [50], it is obvious that the bonds in the cermets are more localized in case of former than the later. Such a treatment although qualitative in nature is helpful in developing novel boride based cermets.

The interfacial bonds strength, which is the net result of wettability of the binder to the hard boride phase, is of importance. For example in developing steel matrix composites containing various volume fraction of TiB_2 [51], it was reported that with the increase in volume fraction of TiB_2 the total sintered porosity increases, thus making the composites less dense. This correlates that Fe with rather low statistical weight of d^{10} configuration is not an ideal candidate for such composites. However, from the cost point of view the preference naturally goes to iron. Under these circumstances the alloying of iron with nickel appears to be the legitimate answer.

CHAPTER V

CONCLUSIONS

1. The straight Mo_2FeB_2 boride prepared through the elemental route after 1250°C and 1300°C sintering exhibits swelling. % Volume shrinkage increases with the increase in binder content and sintering temperature (1250°C - 1350°C). Mo_2FeB_2 - 12.43 vol.% αFe cermet prepared through the MoB route at 1300°C shows a maximum % volume shrinkage.
2. Densification parameter in case of straight Mo_2FeB_2 and its α -iron bonded cermets prepared through either elemental or MoB route at 1250°C increases with the increase in binder content. The straight Mo_2FeB_2 boride prepared through the MoB route exhibits higher densification parameter as compared to the elemental route.
3. Mo_2FeB_2 - αFe cermets prepared through the elemental route possess fine grain structure as compared to those after MoB route. The boride grain size increases with the increase in binder content and sintering temperature.
4. Mo_2FeB_2 ternary boride phase has a tetragonal lattice structure, which is independent of the processing route. The structure type is isotype with that of U_3Si superstructure.
5. Mechanical properties e.g. Vickers hardness of Mo_2FeB_2 - αFe cermets prepared through the elemental route increase with the increase in α -iron binder content and sintering

temperature. Transverse rupture strength of such cermets prepared either through elemental or MoB route increases with the increase in binder content.

6. Thermal shock resistance of Mo_2FeB_2 - αFe cermets is independent of the binder content.
7. The corrosion resistance of the straight Mo_2FeB_2 boride prepared through the MoB route at 1350°C in 10 wt.% HF solution is superior to that corresponding to 10 wt.% HCl solution. In case of α -iron bonded cermets corrosion resistance is superior in 10 wt.% HCl solution.
8. Sintered porosity of ternary borides decreases in the order $\text{Mo}_2\text{FeB}_2 \rightarrow \text{Mo}_2\text{NiB}_2 \rightarrow \text{Mo}_2(\text{Fe}_{0.5}\text{Ni}_{0.5})\text{B}_2$, while in their based cermets the order is reverse. With the increase in the binder content in the range 0-24 vol.%, sintered porosity falls.
9. Sintered hardness of ternary borides decreases in the order $\text{Mo}_2\text{NiB}_2 \rightarrow \text{Mo}_2(\text{Fe}_{0.5}\text{Ni}_{0.5})\text{B}_2 \rightarrow \text{Mo}_2\text{FeB}_2$ while in case of their based cermets the order is reverse. α -iron and $\gamma(\text{FeNi})$ binder containing cermets exhibit a hardness maximum at 12 vol% binder, while nickel bonded cermets show uniform hardness fall with increase in the binder content.
10. Transverse rupture strength of all cermets irrespective of the binder increases with the increase in the binder content. In magnitude the value for any binder composition decreases in the sequence $\text{Ni} \rightarrow \gamma(\text{FeNi}) \rightarrow \alpha\text{Fe}$ bonded cermets.

11. The sequence in indentation fracture toughness variation also follows the pattern similar to transverse rupture strength. However for a binder content greater than 24 vol.% $\gamma(\text{FeNi})$ the toughness drops drastically.
12. Nickel bonded cermets exhibit maximum grain coarsening by Ostwald ripening during liquid phase sintering, followed by the $\gamma(\text{FeNi})$ and α -iron bonded cermets.
13. Boride-binder phase contiguity of $\text{Mo}_2\text{Fe}(\text{Ni})\text{B}_2$ - $\text{Fe}(\text{Ni})$ cermets increases with the increase in $\text{Fe}(\text{Ni})$ binder content. The increase in boride - binder phase contiguity in these cermets exhibits the order in binder as $\alpha\text{Fe} \rightarrow \gamma(\text{FeNi}) \rightarrow \text{Ni}$.
14. Binder mean free path of $\text{Mo}_2\text{Fe}(\text{Ni})\text{B}_2$ - $\text{Fe}(\text{Ni})$ cermets increases with the increase in $\text{Fe}(\text{Ni})$ binder content.
15. Mo_2NiB_2 ternary boride phase possesses an orthorhombic lattice structure. The structure type is isotype with that of W_2CoB_2 superstructure. In case of $\text{Mo}_2(\text{Fe}_{0.5}\text{Ni}_{0.5})\text{B}_2$ mixed double ternary boride the structure is tetragonal and is isotype with that of U_3Si_2 superstructure.
16. Saturation magnetic flux density of cermets increases uniformly with the increase in binder content, the value is greater for α -iron bonded cermets than the $\gamma(\text{FeNi})$ bonded ones.
17. The thermal shock resistance of any investigated cermet system is independent of the binder content. The values for nickel and $\gamma(\text{FeNi})$ bonded cermets are twice than those for α -iron bonded cermets.

18. The corrosion resistance of $\text{Mo}_2\text{Fe}(\text{Ni})\text{B}_2\text{-Fe}(\text{Ni})$ cermets increases in the order of binder as $\alpha \text{ Fe} \rightarrow \gamma (\text{FeNi}) \rightarrow \text{Ni}$ in either corrosive medium i.e., 10 wt.% HCl or 10 wt.% HF.
19. The properties of the cermets can be correlated with the bonding between the hard phase and binder, which in its own turn depends on the electronic structure of the individual components.
20. $\text{Mo}_2\text{Fe}(\text{Ni})\text{B}_2\text{-Fe}(\text{Ni})$ cermets exhibit intergranular brittle fracture mode.

REFERENCES

1. K. Takagi, T. Watanabe, T. Ando and Y. Kondo; Int. J. Powder Metall.; Vol. 22; No. 2, 1986, p. 91-96.
2. K. Takagi, M. Komai, T. Ide, T. Watanabe and Y. Kondo, Powder Metall. Int.; Vol. 19, No. 5, 1987, p. 30-33.
3. K. Takagi, M. Komai, T. Ide, T. Watanabe and Y. Kondo; Int. J. Powder Metall.; Vol. 23; No. 3, 1987, p. 157-161.
4. T. Ide, K. Nakano, T. Ando; Powder Metall. Int.; Vol. 20, No. 3; 1988, p. 21-24.
5. M. Komai, K. Takagi, T. Watanabe and Y. Kondo; API Confernece Proceeding 231, "Boron-Rich Solids (1991)", Edited by D. Emin, T. L. Aselaye, A. C. Switendick, B. Morrosin and C. L. Beckel, American Institute of Physics, New York; 1991, p. 578-581.
6. K. Takagi, S. Ohira, T. Ide, T. Watanabe and Y. Kondo; Reprint from Metal Powder Report; Vol. 42, No. 718, July/Aug. 1987.
7. W. Rieger, H. Nowotny and F. Benesovsky; Monatsh. Chem.; Vol. 95, 1964, p. 1502-1503.
8. E.I. Gradyshvsky, T. F. Fedorov, Yu, B. Kuzuma and R. V. Skolozdra; Poroshkovaya Metallurgia; No. 4, 1966, p. 55-60.
9. H. Haschke, H. Nowotny and F. Benesovsky; Monatsh. Chem.; Vol. 97, 1966, p. 1459-1468.
10. R.M. German, K.S. Hwang and D.S. Mandan; Powder Metall. Int.; Vol. 19; No. 2, 1987; p. 15-18.
11. T. Ide and T. Ando; Metall. Trans. A; Vol. 20A; Jan. 1989, p. 17-24.
12. P. T. Kolomytsev and N. V. Moskaleva; Sov. Powder Metall. and Metal Ceramics; 44, No. 8, Aug. 1966, p. 86-92.
13. M. Komai, Y. Yamosaki, K. Takagi and T. Watanabe; Properties of Emerging PM Mateials Advances in Powder Metallurgy and Particulate Materials - 1992; Vol. 8, Compiled by J. M. Capus and R. M. German., p. 81 - 88.
14. W. Rieger, H. Nowotny and F. Benesovsky; Mh. Chem.; 97, 1966, p. 378-382.
15. M. Komai, Y. Yamasaki and K. Takagi; Solid State Phenomena; Vol. 25 and 26; 1992; p. 531-538.

16. K. Takagi, S. Ohira, T. Ide, T. Watanabe and Y. Kondo; Modern Development in Powder Metallurgy; Vol. 16, 1984, p. 153-166.
17. K. Takagi, M. Komai, T. Watanabe and Y. Kondo; Proceeding 'P/M '90 World Conference on Powder Metallurgy', Vol. 1; The Institute of Metals, London; 1990, p. 374-384.
18. M. Komai, K. Takagi, T. watanabe and Y. Kondo; MRS Int'l Mfg. on Adv. Mats.; Vol. 4, 1989, p. 475-480.
19. C. B. Ponton and R. D. Rawlings; Mat. Sci. Tech.; V. 5, 1989, p. 961-976.
20. J. Gurland; Trans. Met. Soc. AIME; Aug. 1958, p. 452-455.
21. Properties of Elements: Handbook (Ed. G. V. Gamsonov), Vol. I (Physical Properties), Metallurgia, Moscow, 1976 (in Russian).
22. ASM Reference Book, 2nd Edition, ASM, Materials Park, Ohio, 1983, p. 426.
23. R. Chatterjee - Fischer, In 'Surface Modification Technologies', Ed. T. S. Sudershan, Marcel Dekker, New York; 1985, p. 567.
24. T. B. Massalski, Binary Phase Diagrams, ASM, Materials Park, Ohio, 1986, vol 1, P. 366.
25. J. Nowacki and L. Klimek; J. Mat. Sci.; vol. 27, 1992, 3651.
26. M. Hansen, Constitution of Binary Alloys, McGraw Hill, New York, 1958, p. 250.
27. K. I. Portnoi, M. Kh. Levinskaya and V. M. Romastov; Sov. Powder Metallurgy & Metal Ceramic; No. 8, 1969, 657.
28. K. I. Portnoi, V. M. Romashov; Sov. Powder Metall. Met. Ceram; No. 11, 1972, 378.
29. L. G. Voroshnin, L. S. Lofakhovich, G. G. Panich and G. F. Protasevich; Met. Sc. Heat Treatment; vol. 12, 1970, 732.
30. T. G. Chart, Critical Assessment of Thermodynamic Data for the Iron Boron System, National physical Laboratory, Teddington, U. K. 1982.
31. M. Yukinobu, O. Ogawa and S. Goto; Metall. Trans. 20B; 1989, 705.
32. E. Kneller and Y. Khan; Z. Metallk; vol. 78, 1987, 825.
33. Metals Handbook, 8-th Ed., vol. 1., ASM International, Materials Park, 1961.

34. A.E. Vol, Handbook of Binary Metallic Systems Structure and Properties, edited by N. V. Ageev, Israel program for Scientific Translations, Jerusalem, vol. 1, 1966.
35. O. C. Yurchenko; Poroshkovaya Metallurgia; No. 1, 1971, 45.
36. M. Hansen, Constitution of Binary Alloys, 2nd Ed., McGraw Hill, New York, 1958.
37. G. S. Upadhyaya, In Sintered Metal-Ceramic Composites, Ed. G. S. Upadhyaya, Elsevier, Amsterdam, 1984, p.41.
38. H. A. Fine and G. H Geiger, Handbook on Material and Energy Balance Calculations in Metallurgical Processes, TMS, Warrendale, 1979.
39. P. S. Kisly (Ed.), Kermeti, Naukova Dumka, Kiev, 1985, p. 192 (In Russian).
40. P. C. Mukherjee, Fundamentals of Metal Casting Technology, Oxford & IBH Pub. Co. New Delhi, 1979, p. 55.
41. R. A. Alfintseva, L. G. Bodrova and A.D. Verkhoturov, in 'High Temperature Borides and Silicides', Naukova Dumka, Kiev, 1978, p. 95.
42. J. L. Everhart, Engineering Properties of Ni and Ni-alloys, Plenum Press, New York, 1971, p. 196.
43. W. Betteridge, Nickel and its Alloys, Macdonald and Evan, Plymouth, 1977, p. 65.
44. A. Howie and P. R. Swann; Phil. Mag. Series 8; vol. 6, 1961, 1215.
45. A. R. Von Hippel, Dielectrics and Waves, Wiley, New York, 1954, p. 220.
46. J. Kanamori and H. Akai, In 'Transition Metals 1977', Ed. M. J. G. Lee, J. M. Perz and E. Fowcett, The Inst. of Phy., Bristol, 1978, p. 384.
47. G. V. Samsonov and G. S. Upadhyaya; High Temperatures High Pressures; vol. 3, 1971, 635-647.
48. G. V. Samsonov; Electron Technology; vol. 3, No. 1/2, 9-13.
49. G. S. Upadhyaya, In, 'Sintered Metal Ceramic Composites, Ed. G. S. Upadhyaya, Elsevier Science Publishers B. V., Amsterdam, p. 41.
50. G. S. Upadhyaya; Bull. Mat. Sc.; vol. 17, No. 6, 1994, 921-934.

51. B. P. Saha and G. S. Upadhyaya; Journal of Materials Processing Technology; vol. 3, 1993, 363-382.
52. Powder Data File No. 6-0696.
53. Ibid. 4-0809.
54. Ibid. 31-206.
55. C. G. Wilson and F. J. Spooner; Acta. Cryst.; 16, 1963, p. 230-231.
56. Pearson's Handbook of Crystallographic Data for Intermetallic Phases - P. Villars and L.D. Calvert, American Society for Metals, Materials Park, V.3, 1985, p. 2194.
57. Powder Data File No. 25-561.
58. Pearson's Handbook of Crystallographic Data for Intermetallic Phases - P Villars and L. D. Calvert, American Society for Metals, Materials Park, V. 2, 1985, p. 1332.
59. Powder Data File No. 6 - 0636.
60. Ibid. 6-0682.
61. Ibid. 6 - 0644.
62. Ibid. 6 - 0228.
63. Ibid. 32-463.
64. Ibid. 3-1053.
65. Ibid. 20-524.
66. Ibid. 19-609.
67. Ibid. 18-839.
68. Ibid. 4-0850.
69. Pearson's Handbook of Crystallographic Data for Intermetallic Phases - P. Villars and L. D. Calvert, American Society for Metals, Materials Park, V. 3, 1985, p. 2753.
70. Powder Data File No. 3-1036.
71. Ibid. 17-572.
72. Ibid. 6-0567.
73. Ibid. 25-576.

- 74. Ibid. 17-335.
- 75. Ibid. 12-417.
- 76. Ibid. 12-416.
- 77. Pearson's Handbook of Crystallographic Data for Intermetallic Phases - P. Villars and L. D. Calvert, American Society for Metals, Materials Park, V. 3, 1985, p. 1333.

APPENDIX

X-RAY DIFFRACTION RESULTS OF $\text{Mo}_2\text{Fe}(\text{Ni})\text{B}_2\text{-Fe}(\text{Ni})$ CERMETS

Table : A1

Cermet Composition : 100% Mo_2FeB_2
0% binder

Radiation : CuK_α

Diffraction Angle $\theta_{h_i k_i l_i}$ (°)	Interplanar Spacings $d_{h_i k_i l_i}$ (Å)	% Relative Intensity $\frac{I}{I_{\max}} \times 100\%$	Diffraction planes $\{h_i k_i l_i\}$	Identified Phases
14.23	3.1373	15.66	{001}	Mo_2FeB_2
17.20	2.607	70.48	{210}	Mo_2FeB_2
18.00	2.4947	24.10	{111}	Mo_2FeB_2
21.20	2.1318	88.55	{201}	Mo_2FeB_2
22.03	2.0557	37.35	{220}	Mo_2FeB_2
22.65	2.0019	100.00	{211}	Mo_2FeB_2
24.80	1.8379	40.96	{310}	Mo_2FeB_2
29.40	1.5704	21.69	{002}	Mo_2FeB_2
33.18	1.4088	25.90	{410}	Mo_2FeB_2
35.00	1.3441	28.92	{212}	Mo_2FeB_2
36.85	1.2855	39.76	{420}	Mo_2FeB_2
37.85	1.2564	40.96	{331}	Mo_2FeB_2
40.25	1.1931	26.51	{312}	Mo_2FeB_2

Table : A2

Cermet Composition : Mo_2FeB_2 - 12.43 vol.% αFe Radiation : CrK_α

Diffraction Angle $\theta_{h_i k_i l_i}$ ($^\circ$)	Interplanar Spacings $d_{h_i k_i l_i}$ (\AA)	% Relative Intensity $\frac{I}{I_{\text{max}}} \times 100\%$	Diffraction planes $\{h_i k_i l_i\}$	Identified Phases
21.40	3.1393	31.75	{001}	Mo_2FeB_2
26.22	2.5926	79.37	{210}	Mo_2FeB_2
27.34	2.4941	28.57	{111}	Mo_2FeB_2
28.88	2.3720	30.16	-	?
32.60	2.1260	84.13	{201}	Mo_2FeB_2
33.98	2.0497	30.16	{220}	Mo_2FeB_2
34.25	2.0353	28.57	{110}	αFe
34.93	2.0008	100.00	{211}	Mo_2FeB_2
38.73	1.8310	41.27	{310}	Mo_2FeB_2
46.73	1.5731	20.63	{002}	Mo_2FeB_2
47.90	1.5438	19.05	-	?
54.55	1.4061	22.22	{410}	Mo_2FeB_2
58.53	1.3431	36.51	{212}	Mo_2FeB_2
63.15	1.2839	47.62	{411}	Mo_2FeB_2
66.03	1.2536	47.62	{331}	Mo_2FeB_2

Table : A3

Cermet Composition : 100% $\text{Mo}_2(\text{Fe}_{0.5}\text{Ni}_{0.5})\text{B}_2$
0% binder

Radiation : CrK_α

Diffraction Angle $\theta_{h_i k_i l_i}$ (°)	Interplanar Spacings $d_{h_i k_i l_i}$ (Å)	% Relative Intensity $\frac{I}{I_{\max}} \times 100\%$	Diffraction planes $\{h_i k_i l_i\}$	Identified Phases
21.33	3.1498	8.98	{001}	$\text{Mo}_2(\text{Fe}_{0.5}\text{Ni}_{0.5})\text{B}_2$
23.23	2.9047	12.11	{200}	$\text{Mo}_2(\text{Fe}_{0.5}\text{Ni}_{0.5})\text{B}_2$
26.13	2.6013	46.09	{210}	$\text{Mo}_2(\text{Fe}_{0.5}\text{Ni}_{0.5})\text{B}_2$
27.28	2.4996	16.41	{111}	$\text{Mo}_2(\text{Fe}_{0.5}\text{Ni}_{0.5})\text{B}_2$
28.95	2.3664	13.67	-	?
32.48	2.1333	100.00	{201}	$\text{Mo}_2(\text{Fe}_{0.5}\text{Ni}_{0.5})\text{B}_2$
33.75	2.0618	31.25	{220}	$\text{Mo}_2(\text{Fe}_{0.5}\text{Ni}_{0.5})\text{B}_2$
34.80	2.0070	59.38	{211}	$\text{Mo}_2(\text{Fe}_{0.5}\text{Ni}_{0.5})\text{B}_2$
38.50	1.8400	17.58	{310}	$\text{Mo}_2(\text{Fe}_{0.5}\text{Ni}_{0.5})\text{B}_2$
53.93	1.4172	12.11	{410}	$\text{Mo}_2(\text{Fe}_{0.5}\text{Ni}_{0.5})\text{B}_2$
58.30	1.3463	44.53	{212}	$\text{Mo}_2(\text{Fe}_{0.5}\text{Ni}_{0.5})\text{B}_2$
62.60	1.2902	19.53	{420}	$\text{Mo}_2(\text{Fe}_{0.5}\text{Ni}_{0.5})\text{B}_2$
65.40	1.2598	75.78	{410}	$\text{Mo}_2(\text{Fe}_{0.5}\text{Ni}_{0.5})\text{B}_2$

Table : A4

Cermets Composition : $\text{Mo}_2(\text{Fe}_{0.5}\text{Ni}_{0.5})\text{B}_2$ - 11.51 vol.% γ (FeNi)Radiation : CrK_α

Diffraction Angle $\theta_{h_i k_i l_i}$ (°)	Interplanar Spacings $d_{h_i k_i l_i}$ (Å)	% Relative Intensity $\frac{I}{I_{\max}} \times 100\%$	Diffraction planes $\{h_i k_i l_i\}$	Identified Phases
21.35	3.1463	33.00	{001}	$\text{Mo}_2(\text{Fe}_{0.5}\text{Ni}_{0.5})\text{B}_2$
26.18	2.5967	90.00	{210}	$\text{Mo}_2(\text{Fe}_{0.5}\text{Ni}_{0.5})\text{B}_2$
27.33	2.4953	43.00	{111}	$\text{Mo}_2(\text{Fe}_{0.5}\text{Ni}_{0.5})\text{B}_2$
32.48	2.1333	98.00	{201}	$\text{Mo}_2(\text{Fe}_{0.5}\text{Ni}_{0.5})\text{B}_2$
33.45	2.0781	84.00	{111}	γ (FeNi)
33.88	2.0551	66.00	{220}	$\text{Mo}_2(\text{Fe}_{0.5}\text{Ni}_{0.5})\text{B}_2$
34.90	2.0020	100.00	{211}	$\text{Mo}_2(\text{Fe}_{0.5}\text{Ni}_{0.5})\text{B}_2$
38.58	1.8370	50.00	{310}	$\text{Mo}_2(\text{Fe}_{0.5}\text{Ni}_{0.5})\text{B}_2$
39.50	1.8008	28.00	{200}	γ (FeNi)
46.63	1.5759	16.00	{002}	$\text{Mo}_2(\text{Fe}_{0.5}\text{Ni}_{0.5})\text{B}_2$
54.35	1.4096	26.00	{410}	$\text{Mo}_2(\text{Fe}_{0.5}\text{Ni}_{0.5})\text{B}_2$
58.25	1.3470	24.00	{212}	$\text{Mo}_2(\text{Fe}_{0.5}\text{Ni}_{0.5})\text{B}_2$
62.85	1.2873	38.00	{411}	$\text{Mo}_2(\text{Fe}_{0.5}\text{Ni}_{0.5})\text{B}_2$
65.70	1.2568	29.00	{220}	γ (FeNi)
66.38	1.2502	22.00	{331}	$\text{Mo}_2(\text{Fe}_{0.5}\text{Ni}_{0.5})\text{B}_2$

Table : A5

Cermet Composition : 100% Mo_2NiB_2

0% binder

Radiation : CrK_α

Diffraction Angle $\theta_{h_i k_i l_i}$ ($^\circ$)	Interplanar Spacings $d_{h_i k_i l_i}$ (\AA)	% Relative Intensity $\frac{I}{I_{\text{max}}} \times 100\%$	Diffraction planes $\{h_i k_i l_i\}$	Identified Phases
18.93	3.5317	8.36	{200}	Mo_2NiB_2
23.28	2.8988	18.58	{101}	Mo_2NiB_2
26.10	2.6037	22.29	{011}	Mo_2NiB_2
30.23	2.2754	35.91	{020}	Mo_2NiB_2
31.50	2.1923	6.81	-	?
33.18	2.0933	100.00	{310}	Mo_2NiB_2
36.78	1.9133	12.07	{220}	Mo_2NiB_2
37.23	1.8935	8.67	{301}	Mo_2NiB_2
39.75	1.7913	20.43	{121}	Mo_2NiB_2
46.08	1.5904	14.24	{002}	Mo_2NiB_2
56.58	1.3724	6.81	{031}	Mo_2NiB_2
57.88	1.3525	5.57	{510}	Mo_2NiB_2
59.28	1.3325	6.19	-	?
61.45	1.3040	10.53	{022}	Mo_2NiB_2
62.20	1.2949	14.86	{501}	Mo_2NiB_2
63.65	1.2783	22.91	{231}	Mo_2NiB_2
64.63	1.2678	29.1	{312}	Mo_2NiB_2
69.33	1.2243	7.12	{222}	Mo_2NiB_2

Table : A6

Cermec Composition : 100% Mo_2NiB_2 -10.88 vol.%NiRadiation : CrK_α

Diffraction Angle $\theta_{h_i k_i l_i}$ ($^\circ$)	Interplanar Spacings $d_{h_i k_i l_i}$ (\AA)	% Relative Intensity $\frac{I}{I_{\text{max}}} \times 100\%$	Diffraction planes $\{h_i k_i l_i\}$	Identified Phases
23.28	2.8988	19.05	{101}	Mo_2NiB_2
26.00	2.6130	16.99	{011}	Mo_2NiB_2
28.93	2.3683	10.41	-	?
30.18	2.2789	20.97	{020}	Mo_2NiB_2
31.73	2.1783	5.78	-	?
33.05	2.1003	100.00	{211}	Mo_2NiB_2
34.38	2.0288	3.54	{111}	Ni
36.68	1.9178	4.84	{220}	Mo_2NiB_2
37.10	1.8989	8.10	{301}	Mo_2NiB_2
39.78	1.7904	15.98	{121}	Mo_2NiB_2
61.30	1.3059	4.704	{022}	Mo_2NiB_2
62.00	1.2973	8.10	{501}	Mo_2NiB_2
63.58	1.2791	29.65	{231}	Mo_2NiB_2
64.50	1.2691	18.73	{312}	Mo_2NiB_2
69.23	1.2251	17.79	{222}	Mo_2NiB_2

4 1713

421713
Date Slip

Date Slip

This book is to be returned on the date last stamped.

[illegible]

MS P- 1995-D-BAG-PRO



A121713